Synthesis and Characterization of TiO_2 Nanowire and Nanotube Arrays for Increased Optoelectronic Functionality

by

Arash Mohammadpour

A thesis submitted in partial fulfillment of the requirements for the degree of

Doctor of Philosophy

in

Microsystems and Nanodevices

Department of Electrical and Computer Engineering
University of Alberta

Abstract

The n-type semiconducting, vertically oriented TiO_2 nanotube and nanowire arrays constitute a mechanically robust, high surface area, easily functionalized architecture with vectorial electron percolation pathways and have been the focus of interest for variety of applications including but not limited to solar cells, water photoelectrolysis and photocatalysis, hydrogen sensors, drug delivery, stem cell differentiation and glucose sensors. Novel applications and better performance in present applications require innovative and more complex TiO_2 nanostructures.

We reported on fabrication of multipodal TiO_2 nanotubes. Multipodal refers to the nanotubes with more than one leg and are desirable for applications relying on differential surface functionalization and volume filling of individual legs. Capillary and hydrogen bonding forces dominant on the micro- and nanoscale strong enough to bend the TiO_2 nanotubes by tens of degrees are generated during the imbibition of electrolyte into and out of the intertubular spaces between adjacent tapered nanotubes. These forces were exploited to develop a mechanism we call “nanotube combination” to produce multipodal nanotubes.

Very large diameter TiO_2 nanotubes with inner diameters as large as 900 nm, were also generated which surpass the largest inner diameter reported thus far for anodically formed self-organized TiO_2 nanotubes by a factor of 2.5. Such nanotubes with pore diameters comparable with the optical wavelength make it possible to perform unprecedented resonance scattering and effective medium regime studies. Large diameter nanotube arrays were simulated using the finite difference time domain (FDTD) method, and the simulated optical properties were compared to those measured experimentally.

Inefficient absorption of red/near-IR light by sensitized TiO_2 nanostructures limits the efficiency of light harvesting involved applications they are employed in, and utilizing Förster resonance energy transfer (FRET) is promising for resolving the problem. However, FRET efficiencies benefit strongly from the deterministic placement of chromophores. We tested the possibility of FRET phenomenon in nanoporous anodic aluminum oxide (AAO) by encapsulating Alq_3 molecules into the nanvoids in the pore wall fissures and coating carboxyfluorescein onto the surface of the walls. Due to the efficient FRET for such a chromophore placement in AAO, such deterministic positioning might also be advantageous to apply to TiO_2 nanotubes.

We performed the first direct measurement of charge carrier mobility in TiO_2 nanowire arrays. We reported an effective electron drift mobility of 1.9×10^{-5} $cm^2V^{-1}s^{-1}$ in rutile nanowire arrays directly measured using the time of flight and space charge limited current techniques. In addition, we measured an equilibrium free electron concentration of $\sim 10^{14}$ cm^{-3} and a trap density of 3.5×10^{16} cm^{-3} in rutile nanowires. These results point to the importance of reducing traps to improve charge transport in rutile nanowires.

We also introduced magnetic field for the first time to the process of electrochemical anodization of TiO_2 nanotube arrays and demonstrated its advantages in addressing limitations of the conventional anodization method. The use of magnetic fields provides the possibility of anodic growth of TiO_2 nanotubes through anodization of discontinuous Ti films which is unprecedented. It expands the possibilities of employing TiO_2 nanotube arrays in complex devices such as MEMS, lab-on-a-chip and microchips.

Preface

Results of the research presented in chapter 3 has been published as Mohammadpour A and Shankar K, "Anodic TiO_2 nanotube arrays with optical wavelength-sized apertures", Journal of Materials Chemistry 20(39) 8474-8477 2010. I ran the experiments and performed data collection and analysis as well as manuscript composition. Shankar K was the supervisory author and was involved with manuscript composition.

Results of the research presented in chapter 4 has been published as Mohammadpour A, Waghmare PR, Mitra SK and Shankar K, "Anodic Growth of Large-Diameter Multipodal TiO_2 Nanotubes", ACS Nano 4(12) 7421-7430 2010. I was the first to observe the serendipitous formation of multipodal nanotubes. Subsequently, I designed and conducted experiments on the growth of multipodal nanotubes and performed data collection and analysis as well as manuscript composition. Waghmare PR performed data collection on capillary forces and its effect of nanotube bending and manuscript composition. Shankar K and Mitra SK were the supervisory authors and were involved with manuscript composition.

Results of the research presented in chapter 5 has been published as Mohammadpour A, Utkin I, Bodepudi SC, Kar P, Fedosejevs R, Pramanik S and Shankar K, “Photophysics and Energy Transfer Studies of Alq_3 Confined in the Voids of Nanoporous Anodic Alumina”, Journal of Nanoscience and Nanotechnology 13, 2647-2655 2013. I designed and performed the experimental work related to chromophore placement, and also performed the collection of optical data and its analysis as well as manuscript composition. Utkin I and Kar P assisted in time-resolved-photoluminescence data collection, Bodepudi SC generated porous

AAO and Fedosejevs R, Pramanik S and Shankar K were the supervisory authors and were involved with manuscript composition.

Results of the research presented in chapter 6 has been published as Mohammadpour A, Farsinezhad S, Wiltshire B.D and Shankar K, "Majority carrier transport in single crystal rutile nanowire arrays", Phys. Status Solidi RRL 8, No. 6, 512–516 (2014). I ran the experiments and performed data collection and analysis as well as manuscript composition. Farsinezhad S obtained the TEM images and Wiltshire B.D assisted in data collection. Shankar K was the supervisory author and was involved with data analysis and manuscript composition.

Results of the research presented in chapter 7 have been submitted to the Journal of Materials Chemistry A and has been accepted as Mohammadpour A and Shankar K, "Magnetic Field-Assisted Electroless Anodization: TiO_2 Nanotube Growth on Discontinuous, Patterned Ti Films", Journal of Materials Chemistry A 2 13810-13816, 2014. I ran the experimental works and performed data collection and analysis as well as manuscript composition. Shankar K was the supervisory author and was involved with manuscript composition.

Dedicated to My Beloved Wife, Zohreh.

Acknowledgements

First and foremost I would like to express my deepest gratitude to my supervisor, Professor Karthik Shankar for his support, his encouragement and the depth of his knowledge. The achievements attained during my PhD research would have been impossible without his unique supervision, dedication and motivation. I learned from him that success in all aspects of life requires creativity, persistence, and multitasking. For all this I will always be thankful to him.

I would also like to extend my sincerest appreciation to Professor Michael Brett, member of my supervisory committee for providing me valuable comments in order to improve my thesis and also for wonderful experience I had for being TA for his "Microfabrication and Devices" course. I am very thankful to my committee members Professor Sandipan Pramanik, Professor Venkataraman Thangadurai and Professor Hyun-Joong Chung. I am also thankful to Professor Sushanta Mitra, Professor Mojgan Daneshmand, Professor Robert Fedosejevs, Professor Eric Rivard, Dr. Xuejun Sun, Dr. Ilya Utkin, Dr. Prashant R. Waghmare, Dr. Gang He and Srikrishna Chanakya Bodepudi for their help and support during collaborative research. I also appreciate the nanoFAB and NINT management and staff for their technical support and for training me on various pieces of equipment to carry out my research.

In my daily work I have been blessed with a helpful and cheerful group of friends. Special thanks to Dr. Piyush Kar, Dr. Xiaojiang Zhang, Dr. Himani Sharma, Dr. Mohammad Hossein Zarifi, Mourad Benlamri, Ling-Hsuan Hsieh, Joel Boulet, Benjamin Wiltshire, Kaveh Ahadi, Yun Zhang, Ramireddy Boppella, Jordan Goldthorp, Jared Geisinger, Timothy Ho, Conrad Vanden Brink and Matthew Steele. Special thanks to Samira Farsinezhad for assistance in collecting XRD and diffuse-reflection data.

My heartfelt appreciation goes to my parents and my two brothers. They were always there to support and encourage me with their best wishes. Words cannot express my appreciation to my parents for their faith in me and for allowing me to be as ambitious as I wanted. Last, but not least, I would like to dedicate this thesis to my beloved wife, Zohreh. Her support, patience and unwavering love was in the end what made this work possible.

Table of Contents

List of Tables

List of Figures

List of Symbols

Symbol	Definition	First Use
r	Distance between the donor and acceptor molecules	9
n	Refractive index	9
κ	Dipole orientation factor	9
N_A	Avogadro number	9
Φ_D	Fluorescence quantum yield	9
τ_D	Fluorescence lifetime	9
J	Spectral overlap integral	9
F_D	Normalized donor emission spectrum	9
ε_A	Acceptor absorption spectrum	9
ε_∞	Permittivity at infinite frequency	32
λ	Wavelength	32
$\varepsilon_r(\omega)$	Dielectric function	32
$\varepsilon_{r,\infty}$	Relative permittivity at infinite frequency	32
Ω_m	Plasma frequency	32
ω_m	Resonant frequency	32
Γ_m	Damping factor (collision frequency)	32

V_{TFL}	Trap-free limit	88
N_T	Trap density	88
d	Nanowire diameter	88
n_s	Surface state density	88
E	Field	142
β_{PF}	Barrier lowering coefficient of the PF emission	145
ϕ_T	Ionization energy	145
k_B	Boltzman constant	145
T	Temperature	145
β	Field enhancement factor	147
ΔW^s	Surface barrier potential increase	147
ΔW^p	Surface barrier potential decrease	147
β_{Sc}	Barrier lowering coefficient of the Schottky emission	150

List of Abbreviations

Abbreviation	Description	First Use
AAO	Anodic Aluminum Oxide	2
FRET	Förster Resonant Energy Transfer	2
MEMS	Microelectromechanical System	2
UV	Ultraviolet	2
TOF	Time of Flight	8
EG	Ethylene Glycol	15
DEG	Diethylene Glycol	15
DMSO	Dimethyl Sulfoxide	15
RIE	Reactive Ion Etching	17
DI	Deionized	17
XRD	X-ray diffraction	17
FTO	Fluorine Doped Tin Oxide	20
SERS	Surface Enhanced Raman Scattering	26
SEM	Scanning Electron Microscope	28
FESEM	Feld Emission Scanning Electron Microscope	28
FDTD	Finite Difference Time Domain	30
APML	Anisotropic Perfectly Matched Layer	33
XPS	X-ray Photoelectron Spectroscopy (XPS)	44
AR	Aspect Ratio	52

Chapter 1

1. Introduction

1.1. Overview

In 1959 Richard Feynman gave a lecture at the California Institute of Technology on the possibility of molecular level manipulation of materials. Many believe it was the first lecture on the topic of nanotechnology. In the mid-1980s, the term nanotechnology introduced by Eric Drexler and experienced a fast growth worldwide since then[1]. Nowadays it is an indispensable part of the human life and can be traced in a vast number of applications such as food industry[2, 3], water treatment [4, 5], clothes[6, 7], energy conversion[8, 9], constructions[10, 11], medicine[12, 13], environmental protection[14, 15] and many cutting edge technologies. Nanotubes[16-19], nanowires[20-23], mesoporous materials[24-26], nanoshells[27, 28], nanorings[29, 30], nanofibers[31, 32], nanocages[33, 34] and many other nanostructures have been introduced so far among which the first three are the subjects of the works of present thesis. Depending on the applications and their requirements different materials have been employed in the fabrication of the nanostructures. Nanotubes of carbon[16], titanium dioxide[17], boron nitride[19], tungsten sulfide[35], molybdenum disulfide[35] and tin sulfide[36], nanowires of titanium dioxide[37], zinc oxide[23], indium phosphide[38], gallium nitride[39] and silicon[22] and mesoporous structures in materials such as alumina[26], titanium dioxide[40], silica[24] and magnesium oxide[41] are examples of well-studied nanostructures which have been exploited in variety of applications. There have been different methods reported for nanotube and nanowire growth such as templating[42], sol-gel[43], seeded growth[44, 45], hydrothermal[46-48] and anodization[49-52] among which electrochemical anodization and hydrothermal methods have been utilized for synthesis of TiO_2 nanotube and nanowire arrays respectively. Porous anodic

aluminum oxide (AAO) has been generated using anodization method as well. As a general outline of the works presented in present thesis, novel titanium dioxide nanostructures have been generated, different properties in particular optoelectronic properties of TiO_2 nanostructures have been directly investigated for the first time, deterministic placement of chromophores into the nanostructured materials has been performed, Förster resonant energy transfer (FRET) has been studied using a novel geometry for embedding two types of chromophores into the structure of porous AAO, a new technique called magnetic-field-assisted electrochemical anodization has been established for growth of TiO_2 nanotube arrays which makes it possible for the first time to grow TiO_2 nanotube arrays through anodizing discontinuous Ti films. It is also advantageous in facilitating the incorporation of titania nanotube arrays in applications such as microelectromechanical system (MEMS) devices, lab-on-a-chip devices and sensors.

1.2. Titanium dioxide as a semiconductor

Titanium is the fourth most abundant metal in the world and is exceeded in abundance only by aluminum, iron and magnesium. It is also the ninth most abundant element that constitutes 0.63% of the earth's crust. Its oxide in the form of TiO_2 is a large band gap n-type semiconductor and has attracted lots of attention due to retaining a variety of unique and remarkable properties such as chemical stability, non-toxicity and low cost[53]. Possessing relatively high reactivity and chemical stability under ultraviolet (UV) light makes it a decent candidate for photocatalytic applications. Photocatalytic activity of the TiO_2 has been enhanced by extending its photo-response towards visible spectrum through reducing its band gap by doping it by metallic and non-metallic compounds[54]. Photoinduced superhydrophilicity has been

observed by trapping holes at the surface of TiO_2 which results in high wettability[53]. Majority of TiO_2 applications rely on its nanostructured forms which will be discussed later.

Rutile, anatase and brookite are three polymorphs of TiO_2 which have the same chemical structure but different crystal structures. The crystal structures of rutile, anatase and brookite are tetragonal-$P4_2/mnm$, tetragonal-$I4_1/amd$ and orthorhombic-Pbca respectively[55]. When TiO_2 is synthesized via hydrolysis of inorganic or organic titanium compounds it is in anatase and rutile phases mainly and brookite is usually a by-product which is presented along with the other two forms[56]. One of the properties of titanium dioxide is the fact that its crystal structure changes under the temperature variation. At low temperatures lower than about 100 ^oC brookite phase is present, at temperatures higher than 700 ^oC, TiO_2 is mainly in rutile phase and anatase can be isolated from the other two phases at intermediate temperatures[57]. Reported research results have revealed that brookite-to-anatase and anatase-to-rutile conversions occurring due to temperature increment are irreversible; furthermore phase transition temperature depends upon several parameters such as grain size, impurity content, heat treatment and synthesis methods[58]. Rutile is thermodynamically the most stable phase of TiO_2 which has the lowest Gibbs free energy[59]. When the particle size is smaller than 14 nm, the anatase phase is more stable than rutile[60]. This is due to the lower surface free energy of the small size anatase polymorph[61]. The coordination number of neighboring octahedra is different for anatase and rutile. In the case of anatase, each octahedron has connection with 8 nearest neighbor octahedra such that 4 share an edge and the other 4 share a corner. In rutile, there exists a connection with 10 neighbors where 2 share an edge and 8 sharing a corner. Since the number of TiO_2 units per cell are 4 and 2 for anatase and rutile respectively, the former has a larger unit cell than the latter one[62]. Rutile is hence known to be denser than anatase. Moreover, the shapes of OTi_3 units are Y and T in rutile and anatase

respectively and repulsion between Ti cations is smaller in rutile compared to anatase[63]. Highest part of the valence band and lowest part of the conduction band in TiO_2 correspond to the O_{2p} and Ti_{3d} states respectively. In fact, there is a strong hybridization between O_{2p} and Ti_{3d} orbitals which influence the electronic properties as well as the band gap size[63-65]. Larger unit cell of anatase results in a smaller Brillouin zone concomitant with narrower bands. This is why anatase has a larger band gap (3.2 eV) than rutile (3.0 eV)[62]. Rutile phase has the higher refractive index of 2.6 compared to anatase with refractive index of 2.5[66,67]. TiO_2 nanostructures exhibit distinctive chemical, electrical and optical properties in different phases which make them better fits for certain applications. However, fabrication of certain types of nanostructures is still challenging. For instance, despite the success in the fabrication of polycrystalline anatase TiO_2 nanotube arrays[68] as well as polycrystalline rutile nanotube arrays[69, 70] and single crystal rutile nanowire arrays[71], growing monocrystalline vertically oriented TiO_2 nanowire arrays in the anatase phase is not well-established and forms the subject of research work for many researchers worldwide.

1.3. Titanium dioxide nanostructures

Among the variety of TiO_2 nanostructures - nanotubes, nanowires and nanoparticles have attracted lots of attention due to variety of applications they have employed in, including but not limited to solar cells [9, 72-74], water photoelectrolysis and photocatalysis [75-77], hydrogen sensors [78, 79], stem cell differentiation[80, 81], glucose sensors[82, 83], biomarker assays[84], bone emplants[85] and drug delivery [86, 87]. TiO_2 nanotube and nanowire arrays were the subject of interest in research works presented here because of their remarkable properties that are advantageous for applications they are employed in including high surface to volume ratio[88, 89], mechanical

robustness[90], easily functionalization[91, 92] and ability to provide vertical electron percolation pathways[93, 94]. The methodology of electrochemical anodization and solvothermal methods that were employed for generating TiO_2 nanotube and nanowire arrays, respectively, will be discussed in chapter 2.

1.3.1. Motivation and research goals

As mentioned, TiO_2 nanostructures play a decisive rule in numerous scientific and technological applications and many researchers worldwide competitively work on such a hot topic. In spite of significant improvements during the last few years, there is still room for improvement and many challenges still need to be addressed to meet the requirements of novel applications. Some the challenges which were the subject of research work during my PhD study and were successfully addressed are as follows.

Geometrical properties of anodized TiO_2 nanotube arrays including pore diameter, length, wall thickness, inter-tubular distance can be manipulated using anodization parameters. Maximum achievable pore diameter was limited to about 350 nm[95]. Reaching the pore diameters in the range of several hundreds of nanometers was always a subject of interest for researchers due to advantages such a structure could introduce. More importantly diameter could be adjusted to fall in the range comparable with the wavelength of the visible light (400-700 nm). It could facilitate performing unprecedented studies such as light and TiO_2 nanotube array interaction in effective medium regime, resonant scattering of visible light and confining light in a way such that nanotubes act as waveguides.

Most of the studies were focused on anodically grown vertically oriented cylindrical TiO_2 nanotube arrays[75, 96, 97]. Despite the impressive progress in tuning the length, wall thickness,

diameter, and pattern order of anodically formed TiO_2 nanotube arrays, there was still an unmet need for more complex hierarchical nanostructures, which not only improve their functionality in present applications but also make novel applications possible. Applications and techniques which rely on volumetric filling or surface functionalization of nanotubes will particularly benefit from the production of multipodal (multiple legs) nanotubes with a more complex topology. The differential chemical functionalization of the individual legs allows for multiplexed sensing and the loading of multiple drugs. Moreover, since the multipodal structure provides more than one leg for each of the nanotubes, a more robust attachment of nanotubes onto desired substrates is possible, which also renders them good loadbearing elements for mounting heavier structures. The branched topology of multipodal titania nanotubes consisting of a large diameter nanotube dividing at the end into several smaller size nanotubes could be applied for molecular separation in a multiphase multicomponent fluid and for microfluidic and optofluidic applications. The multipodal topology also lends itself to use in three-terminal devices, electrical interconnect networks, and nanoelectromechanical systems. The multipodal structure is highly advantageous in applications such as photocatalysis and photovoltaics due to the larger surface-to-volume ratio and more facile charge separation at the core-leg interfaces.

Electrochemical anodization is a well-established technique for growing TiO_2 nanotube arrays[98-102]. However, there are several drawbacks which limit incorporation of TiO_2 nanotubes in particular applications. First of all, Ti sample is not free standing into the electrolyte and needs to be connected to the anode electrode. Hence, some area of the sample needs to be devoted to electrode connection or for O-ring sealing which is wasteful especially in small samples. Since sample cannot be fully immersed into the electrolyte, fast anodization rate of Ti at air/electrolyte or o-ring/electrolyte interface due to higher local electric fields is another concern. More

importantly, in the present method continuity of the deposited Ti film is required when growing TiO_2 nanotubes on various substrates. Therefore, nanotube growth through anodization of discontinuous/patterned Ti (on MEMS devices for example) becomes impossible. It seems to be impossible to address all these issues using the present anodization technique and introducing new external parameter(s) may resolve the problem. If so, it would fulfill the requirements of novel applications and TiO_2 nanotube arrays will be used more easily and vastly in the structure of MEMS, sensor and photovoltaic devices.

1.4. Optoelectronic properties of titanium dioxide nanostructures

TiO_2 is a widely studied transition metal oxide for electronic applications. In nanocrystalline films consisting of sintered anatase nanoparticles, TiO_2 has been used to generate high performance as the electron transporting scaffold in dye-sensitized[103] and bulk heterojunction solar cells[104], as the electron injecting layer in organic light-emitting diodes[105] and active layer in photocatalysts[106, 107]. However, charge transport in nanocrystalline films of titania is known to be highly dispersive and posited to follow a continuous random walk[108-111]. Structural disorder, hopping transport and trapping states are frequently cited as the reasons for dispersive transport.

1.4.1. Motivation and research goals

Improving charge transport in TiO_2 nanostructures has been an enduring goal to improve device performance. In response, one-dimensional nanostructures oriented vertically from the substrate, such as arrays of nanowires and nanotubes, have been synthesized and applied in electronic devices in order to provide vectorial charge percolation paths and thereby, prevent a random-walk type of transport[71, 112-115]. Anodically grown and annealed TiO_2 nanotubes are

polycrystalline structures[116] and charge carrier transport in such structures is slow due to thermally-activated hopping across grain boundaries. Solvothermal-grown rutile nanowire arrays on the other hand, have the advantage of eliminating hopping at grain boundaries due to their monocrystallinity and ensuring band-like transport. Polycrystalline TiO_2 nanotubes and single crystal rutile nanowire arrays have been used in conjunction with dyes, organic semiconductors and lead halide perovskites to generate high performance solar cells[117-121] and in high-rate photoelectrochemical water-splitting[37, 122]. Rutile nanowire arrays are also attracting research interest as potential lithium ion battery anodes, photocatalysts and field emitters[123-125]. Therefore, an improved understanding of charge transport in TiO_2 nanotubes and nanowires is much needed. There has been no report on direct measurement of charge transport on such structures and it has hitherto been inferred indirectly via impedance/intensity-modulated spectroscopy[126, 127] and terahertz spectroscopy techniques[128, 129]. These techniques have been employed to study charge transport through dye-coated TiO_2 nanotube/nanowire arrays in dye sensitized solar cells for instance. Present research work includes direct measurement of charge transport in titania nanostructures using a method called time of flight (TOF) in an experimental configuration adapted to the transport regime in TiO_2. The methodology of performing the TOF measurement will be discussed in more detail in chapter 2.

1.5. Förster resonance energy transfer

Highly distance sensitivity of Förster resonance energy transfer (FRET) especially at distances in the range of tens of angstroms have introduced them in lots of applications including but not limited to biological applications[130-132], accurate distance determination of acceptor and donor fluorophores[133], light harvesting in photovoltaic devices[134, 135], highly sensitive sensors[136,

[137] and labeling[138, 139]. In contrast to spontaneous radiative decay processes such as fluorescence and phosphorescence, FRET is a non-radiative transmission process of the electronic excitation from a donor (initially excited) to an acceptor (at ground state) when there is enough overlap between their emission and absorption spectra respectively[140]. The rate of FRET between isolated point dipoles is given by

$$K_{FRET} = \frac{9000 \ln(10)\kappa^2.\Phi_D}{128\pi^5 N_A n^4 \tau_D r^6} J \qquad (1.1)$$

where r is the distance between the donor and acceptor molecules, n is the refractive index of the medium, κ is the dipole orientation factor, N_A is the Avogadro number, Φ_D is the fluorescence quantum yield od donor, τ_D is the fluorescence lifetime of the donor, and J is the spectral overlap integral given by the relation:

$$J = \left[\int_0^\infty F_D(\lambda)\varepsilon_A(\lambda)\lambda^4 d\lambda\right] \qquad (1.2)$$

where F_D is the normalized donor emission spectrum (dimensionless property) and ε_A is the acceptor absorption spectrum (expressed as an extinction coefficient)[141]. As can be seen in equ. (1.1), the energy transfer rate is inversely proportional to the sixth power of the r, distance between the donor and acceptor molecules which is an indication of high distance sensitivity of the FRET.

There has recently been a surge of interest in the construction of arrays of hierarchical nanostructures consisting of pores on two or more size scales[142-144]. Hierarchical nanostructures offer the opportunity to place distinct molecules or nanoparticles with plasmonic, excitonic, catalytic, magnetic and other properties in close proximity to each other, and to study and exploit

their interactions. The nanoscale pore systems of zeolitic crystals have been used to incorporate dyes and nanoclusters of metals and semiconductors. Zeolite-encapsulated dyes can act as chemical sensors, second harmonic generators, optical switches and dye microlasers[145]. By using optically inert stop-cock molecules to spatially position and isolate dye molecules in zeolite channels, donor-acceptor dye assemblies have been constructed for use as light harvesting antennas and as functional energy transfer labels in biosensing[145, 146]. Energy transfer from zinc phthalocyanine molecules confined in the inter-nanowire spaces of a close-packed rutile nanowire array to Ru-based organometallic dye anchored to the surface of the nanowires was used to improve the harvesting of red photons in dye-sensitized solar cells[135, 147, 148]. Likewise, exciton-plasmon interaction effects were noted in Au-AgI nanoparticle pair structures electrochemically prepared in porous anodic aluminum oxide (AAO) to either be in contact or separated by the porous host[149]. AAO has been used to prepare SERS-active substrates[150]. AAO with its cylindrical pores filled with Alq_3 dispersed in a polymeric host has also been used to construct an organic electroluminescent device[151]. In addition, confining organic molecules in a rigid solid state matrix is known to improve their photostability[152] and alter their spontaneous emission characteristics[153].

1.5.1. Motivation and research goals

TiO_2 nanostructures are large band gap semiconductors and absorb photons in the UV range hence need to be sensitized using appropriate dyes/quantum dots in order to extend their absorption towards visible and IR region to be functional in light harvesting applications such as solar cells, photocatalysis and photoelectrolysis. Most of the utilized sensitizers suffer from week absorption in the red and near-infrared region. Since the solar spectrum includes a large number of photons in the red and near-infrared region, addressing the light harvesting issue of sensitized

TiO_2 nanostructures in that spectral region would improve the efficiency of applications they are employed in. FRET is a promising candidate for promoting broad spectrum light absorption by utilizing appropriate donor and acceptor dyes. Using FRET, an improvement in the solar cell efficiency have been reported in which donor and acceptor dyes were placed onto inner/outer walls of nanotubes[154] and surface of the nanowires and electrolyte[147] in the cases of TiO_2 nanotube/nanowire based solar cells respectively. FRET has also been used to improve the crystalline TiO_2 nanoparticle based solar cells in which donor quantum dots coated onto the TiO_2 nanoparticles were separated from acceptor dyes by a very thin layer of amorphous titania layer[155, 156]. There is still room for improvement by finding new arrangements for distinctive placement of donor and acceptor dyes onto the structure of TiO_2 nanotubes in order to improve FRET efficiency. FRET happens at distances in the range of 2-10 nm and smaller the distance, higher the energy transfer efficiency[157-159]. The closest imaginable distance proximity is achieved when donor and acceptor molecules are embedded onto and into the walls respectively. While finding techniques for embedding acceptor molecules into the walls of TiO_2 nanotubes is still under investigation, the possibility of FRET phenomenon can be tested in another material's nanostructures which can fulfill the requirements of proposed geometry of donor-acceptor placement. Presence of cracks has already been reported onto the inner wall of pores in porous AAO. High stress accompanying the volumetric change from Al to Al_2O_3 during the rapid anodic growth results in the creation of 1-2 nm sized voids connected to the surface through narrow cracks.[160] Wall cracks provided a site for encapsulating dyes into it. Testing the possibility of FRET phenomenon using voids of the porous AAO is one of the goals of present research work. If performed successfully it could be applied for TiO_2 nanotubes as well.

1.6. Thesis outline and organization

Chapter 2 includes a detailed description of the methodology used in performing experiments. Electrochemical anodization for growing TiO_2 nanotube arrays and solvothermal method for generating TiO_2 nanowire arrays are explained. These methods have been utilized for generating required titania nanostructures for the research works presented in chapters 3, 4, 6 and 7. It also contains explanation about the methodology of performing time of flight measurement for studying charge transport properties of TiO_2 nanostructures.

Chapter 3 contains the report on fabrication of large diameter TiO_2 nanotubes with pore sizes comparable with optical wavelength. Finite-difference time domain (FDTD) simulation of such nanotube structure has been performed and obtained light interaction behavior has been compared with experimentally measured values.

In chapter 4 the first report on fabrication of multipodal TiO_2 nanotube arrays is presented. A detailed study on the mechanism of generation of such nanostructures is also performed.

Chapter 5 reports on the possibility of performing Förster resonance energy transfer (FRET) through embedding dye molecules into the voids in the walls of porous AAO and coating the walls with another type of chromophore. Finding such geometry for placement of donor/acceptor molecules makes it feasible to be applied to other structures including TiO_2 nanotube arrays for the sake of improving the efficiency of applications that deal with light harvesting.

Studying charge transport properties of TiO_2 nanowires and nanotubes is of special importance for variety of applications. However charge carrier transport along the length of such

nanostructures has never been directly performed. Chapter 6 reports on the first direct study of charge transport along rutile TiO_2 nanowires using the time of flight measurement method.

Although the electrochemical anodization method is well-established for growing TiO_2 nanotube arrays with a variety of geometrical and morphological structures, however it alone seems to be incapable of generating more complex nanotube structures in order to meet the requirements of novel applications. Chapter 7 contains the first report on the utilization of magnetic fields in the process of anodization of TiO_2 nanotube arrays and shows how this modification addresses many of the drawbacks of the conventional electrochemical anodization method.

The conclusion of present dissertation and suggested future research works are presented in chapter 8.

Chapter 2

2. Methodology

2.1. Electrochemical anodization of TiO_2 nanotube arrays

A variety of electrochemical cells such as the Tait cell, Corrosion cell, Haber-Luggin capillary and Flat Cell are used to perform electrochemical anodization. We have found that a flat two electrode electrochemical cell provides maximum flexibility for the anodic growth of TiO_2 nanotube arrays, in which the anode electrode is a Ti foil or Ti coated substrate and the cathode consists of Ti foil, Pt or graphite. As shown schematically in Figure 2.1, anode and cathode need to be partially soaked into the electrolyte.

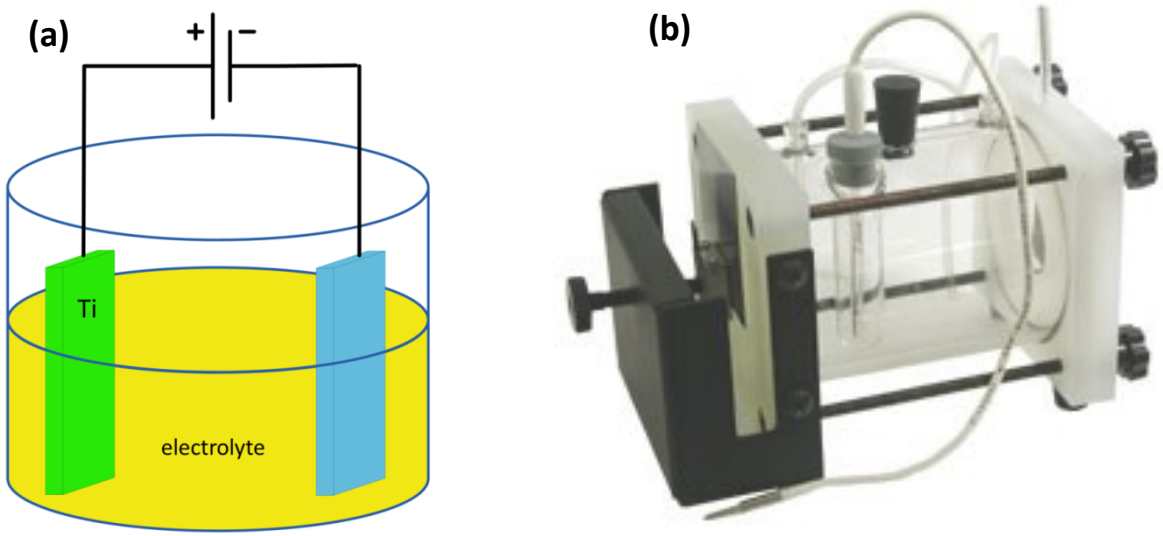

Figure 2.1 (a) schematic image of the electrochemical anodization setup used by us. If needed, a reference electrode, thermometer, or gas purge could be introduced. (b) Photograph of a commercially available O-ring sealed flat electrochemical cell (Princeton Applied Research, Inc.).

In the case of Ti coated substrates, a higher anodization rate at the air-electrolyte interface is problematic and precautions need to be taken into account. Otherwise Ti will get fully anodized at the interface, causing the anode to be electrically disconnected from the rest of the sample which is soaked into the electrolyte following which anodization will stop and sample will not be fully anodized. Deposition of second Ti layer at the interface area could be a solution[115]. We found that this problem could be simply addressed by covering the interface area with parafilm during anodization. The electrolyte consists of aqueous or organic solutions such as ethylene glycol (EG), diethylene glycol (DEG), glycerol, dimethyl sulfoxide (DMSO) and formamide containing fluoride based chemicals such as HF and NH_4F. The advantage of electrochemical anodization is that the geometrical and morphological properties of TiO_2 nanotubes including length, pore diameter, wall thickness, order and roughness can be controlled by manipulating anodization parameters including electrolyte composition, pH and applied voltage. Pore diameter of the nanotubes for instance is directly dependent on the applied voltage. Chemical reactions occurring during anodization are presented in chapter 4. In summary, field-assisted oxidation initiates the nanotube formation process by generating a thin oxide layer known as the "Barrier Layer" (Figure 2.2a) which is followed by pit formation as a result of field-assisted oxide dissolution (Figure 2.2b). The electric field, which is strongest at the pore bottom, promotes the solid-state migration of oxidizing ions ($O2^-$, OH^-) in the barrier layer and enables the pores to grow deeper into the Ti. Due to the equilibrium between the field-assisted oxidation at the metal/oxide interface and field-assisted oxide dissolution at the oxide/electrolyte interface, the metal-oxide interface keeps moving into the Ti (Figure 2.2c). While the barrier layer penetrates deeper into the Ti, the stronger electric field affects the un-anodized metal existing in the walls and due to the field-assisted oxidation and oxide dissolution inter-pore voids are generated which

give rise to nanotubes instead of nanpores (Figure 2.2d). Chemical dissolution is always present at the mouth of the nanotubes and gradually etches them away. Nanotube length continues to increase as long as the rate of movement of the Ti-oxide interface is higher than the chemical dissolution rate. Optimizing the water content in organic electrolytes is crucial because it affects the rates of oxidation and oxide dissolution hence the rate of nanotube growth[161].In fact, the effect of water content is two-fold. Basically the presence of water is needed in order to generate the oxide layer at the pore bottom, at the same time it increases the chemical oxide dissolution at the mouth of the nanotubes. Its concentration needs to be adjusted properly otherwise the nanotubular structure begins to vanish if the chemical dissolution rate of the nanotubes overcomes the nanotube growth rate[162].

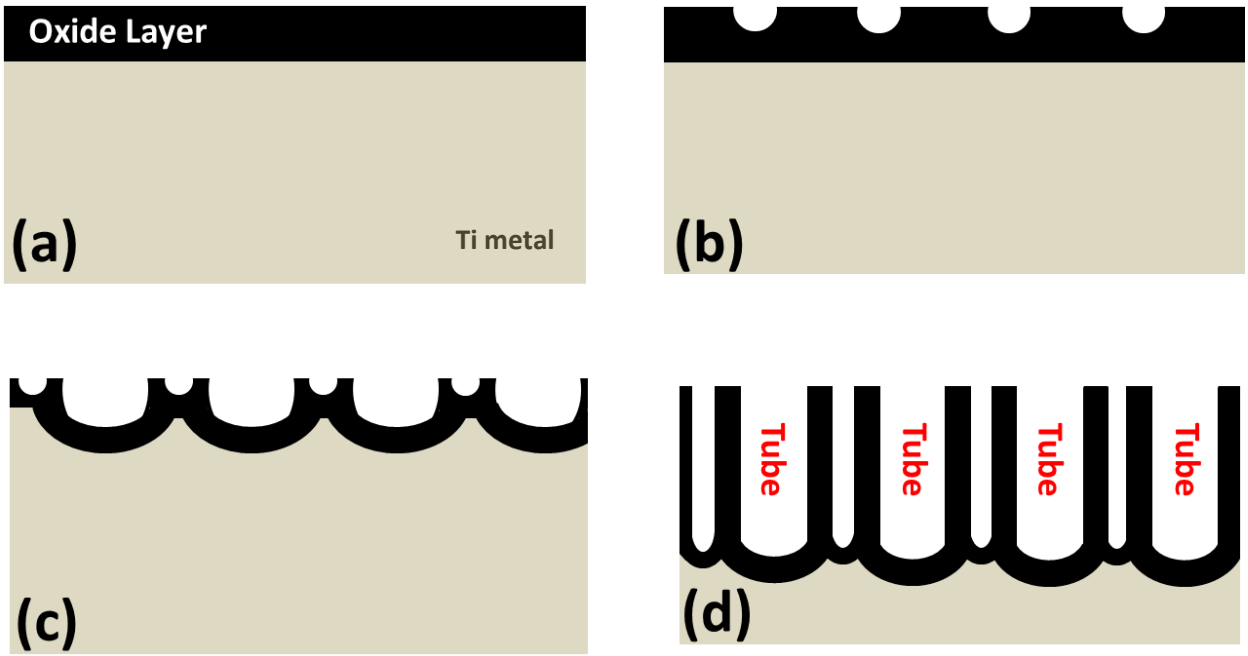

Figure 2.2 Schematic images showing the mechanism of TiO_2 nanotube growth including (a) formation of oxide layer (b) formation of pits (c) penetration of barrier layer into the Ti foil/thin film (d) tube formation.

The fact that TiO_2 is transparent can be used to realize the anodization stop point while anodizing Ti coated substrates. If anodization continues for too long chemical etching at the mouth of the nanotubes will etch them away. Too long anodization is not also good when anodizing Ti foil because chemical etching rate will become progressively stronger as the reaction proceeds (due to the acidification of the electrolyte), and will eventually start dissolving the nanotubes.

Anodized TiO_2 nanotube arrays are amorphous and annealing them in air/oxygen renders them polycrystalline. Annealing at temperatures lower and higher that 700 ^oC will result in anatase and rutile phases respectively. Annealing has other advantages such as filling the oxygen vacancies and converting the any remaining Ti metal into TiO_2 and making the sample completely transparent. Anodized TiO_2 nanotube arrays are usually coated with a thin debris layer with the thickness of about 200 nm. I established an optimized method for removing the debris using SF_6-based reactive ion etching (RIE).

Characterization of TiO_2 nanostructures have been very well documented in the literature[71, 163-170]. In our work, morphologies of grown nanostructures were imaged using JEOL6301F and Hitachi S4800 field emission scanning electron microscopes, X-ray diffraction (XRD) patterns were obtained using Bruker D8 Discover and Rigaku powder X-ray diffractometers and diffuse reflectance and transmittance UV-Vis spectra were collected using Perkin Elmer, Lambda 1050 and 900 spectrophotometers respectively. Figure 2.3 shows cross-sectional SEM image of highly ordered, closely packed, TiO_2 nanotube arrays generated by anodizing Ti foil in an ethylene glycol (EG)-based electrolyte containing 0.3 wt.% NH_4F and 2 vol.% deionized water at 40 V.

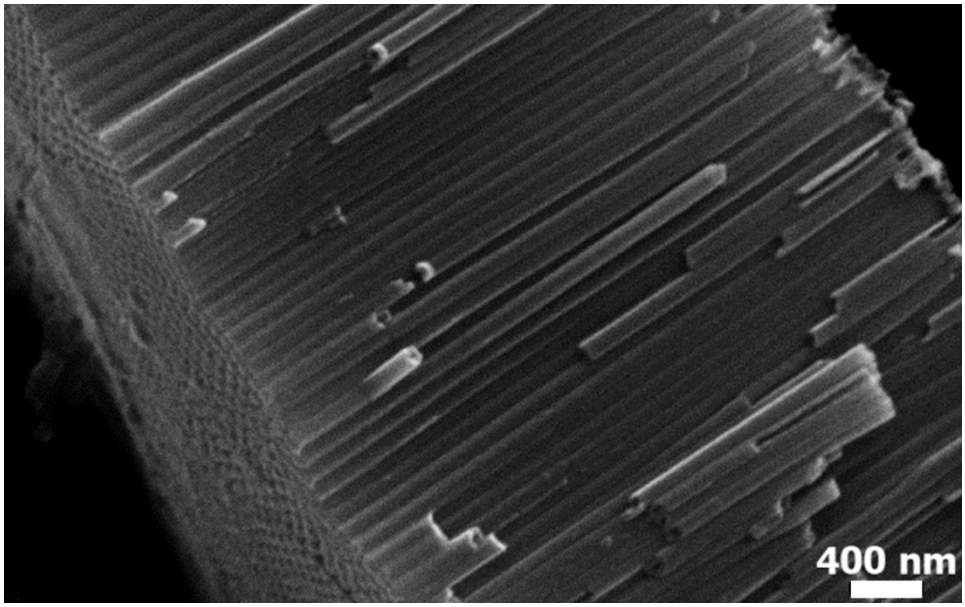

Figure 2.3 SEM image of ordered TiO_2 nanotube arrays grown on Ti foil.

Anodically grown TiO_2 nanotube arrays were amorphous and were crystallized by annealing. Annealing was performed at 500 ^{o}C for 2 hours in air and 1 hour in flowing oxygen with temperature ramped up at 5 ^{o}C/min. After the annealing process was completed, the furnace was turned off and samples cooled down overnight. X-ray diffraction patterns of crystalline TiO_2 nanotube arrays are presented in Figure 2.4a which clearly indicate that fabricated nanotubes are polycrystalline. Ti foil was considered to be the substrate for anodized TiO_2 nanotube arrays. Due to non-transparency of the substrate, optical properties of nanotube arrays could not be investigated using transmission UV-Vis spectroscopy. Hence, absorbance of the nanotube sample was obtained using diffuse reflectance UV-Vis spectroscopy which is depicted in Figure 2.4b. It showed that annealed semiconducting TiO_2 nanotube arrays had their absorption edge at roughly 380 nm.

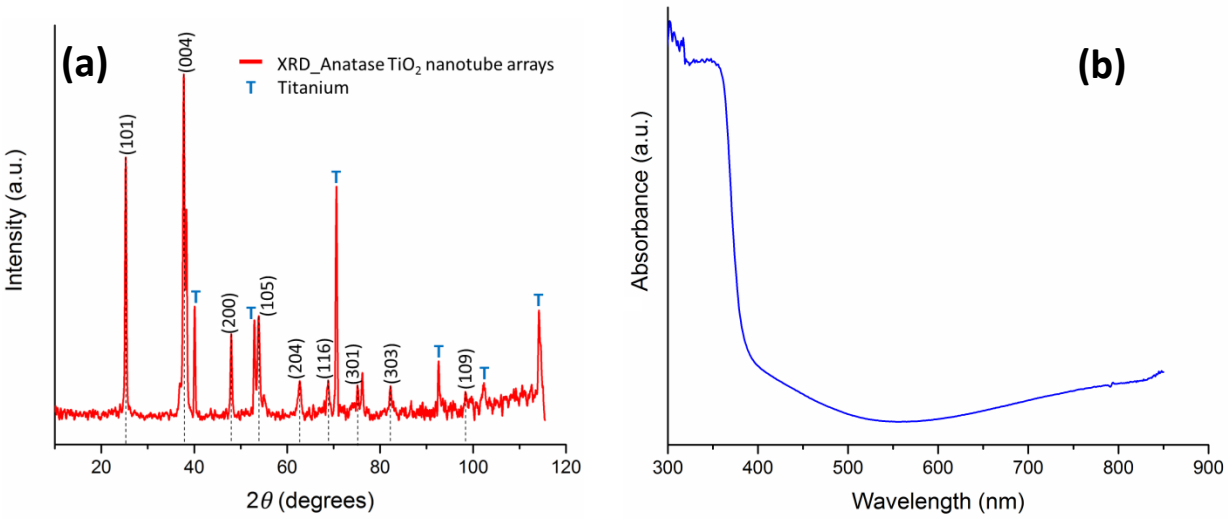

Figure 2.4 (a) XRD patterns and (b) UV-Vis diffuse reflectance spectrum of TiO_2 nanotube arrays grown on Ti foil.

2.2. Hydrothermal growth of TiO_2 nanowire arrays

Single crystal rutile TiO_2 nanowire arrays have been grown using a hydrothermal method for the research works presented in chapter 6. The terms "hydrothermal" and "solvothermal" refer to chemical reactions in a closed system containing one or several precursors in the presence of water and other solvents respectively at temperatures higher than the boiling point of the solvent [171, 172]. The key factors governing these processes are solvent, thermodynamic parameters (temperature and pressure) and chemical composition/concentration of precursors [171, 172]. Hydrothermal method is used for the synthesis of new materials, establishing novel processes for generating functional materials, stabilization of hybrid materials (inorganic/organic, inorganic/biological), crystal growth and producing well-defined micro/nano crystallites in terms of size and morphology. Hydrothermal growth is performed at mild temperatures ($T < 400\ ^oC$) [173]. Pressure plays a key role in the process and depending on the application and required structure wide range of pressures can be applied to it. In the case of growing micro/nano crystallites, pressure controls the crystal size. Since the crystal size is mainly controlled by

nucleation and crystal growth, higher pressures result in larger crystallites by improving the concentration of the solvated species [173]. Pressure also improves the solubility which is favorable for hydrothermal process [172]. In most hydrothermal processes taking into account the presence of some additives is indispensable. The additives might be favorable for the whole process by modifying one or more parameters including solubility, oxidation-reduction properties and crystal growth. For the latter parameter, the additives could be capping agents, surfactants or bio-molecules. These materials have the capability of controlling growth orientation in order to obtain anisotropic nanostructures such as TiO_2 nanowire arrays[171].

In this work, TiO_2 nanowire arrays were grown on fluorine doped tin oxide (FTO) coated glass. The morphology and pattern order of nanowire arrays were controlled by manipulating solution composition. Highly compact, vertically oriented and small diameter nanowire arrays were grown in a solution containing water, acetic acid, hydrochloric acid and titanium butoxide. Without acetic acid, separated larger diameter nanowire arrays were generated. The chamber was a chemical digestion vessel in which a teflon container was filled with solution up to a certain level (10 mL solution) and FTO coated glass was placed against the wall face down at an angle of about 45 degrees. The teflon vessel was secured into a specially designed metallic container in order to tolerate high pressures. Hydrothermal setup was then placed into an oven at the temperature of 180 ^{o}C for at least 1.5 hours. Several micrometer length nanowire arrays were generated using this method and longer process times resulted in longer nanowires. Length of the nanowire arrays was also sensitive to the cleanness of the teflon vessel. In the course of time materials coated onto the vessel walls were acting as nucleation centers consuming the solution agents and leaving fewer agents into the solution to be used for nanowire growth onto the FTO coated glass. After the required time was passed the hydrothermal reactor was taken out of the

oven and cooled down in water for 15 minutes before being opened. TiO_2 nanowire coated sample was rinsed with deionized (DI) water and dried in nitrogen flow. Obtained TiO_2 nanowire arrays were monocrystalline and of the rutile phase.

Top and cross-sectional view SEM images of hydrothermally grown TiO_2 nanowire arrays (generated in 5mL DI water, 2.5 mL hydrochloric acid, 2.5 mL acetic acid and 0.2 mL titanium butoxide) has been depicted in Figure 2.5a and b respectively. It can be seen that nanowire arrays are vertically oriented and highly compact and that possess rectangular cross-section with the width of about 20 nm.

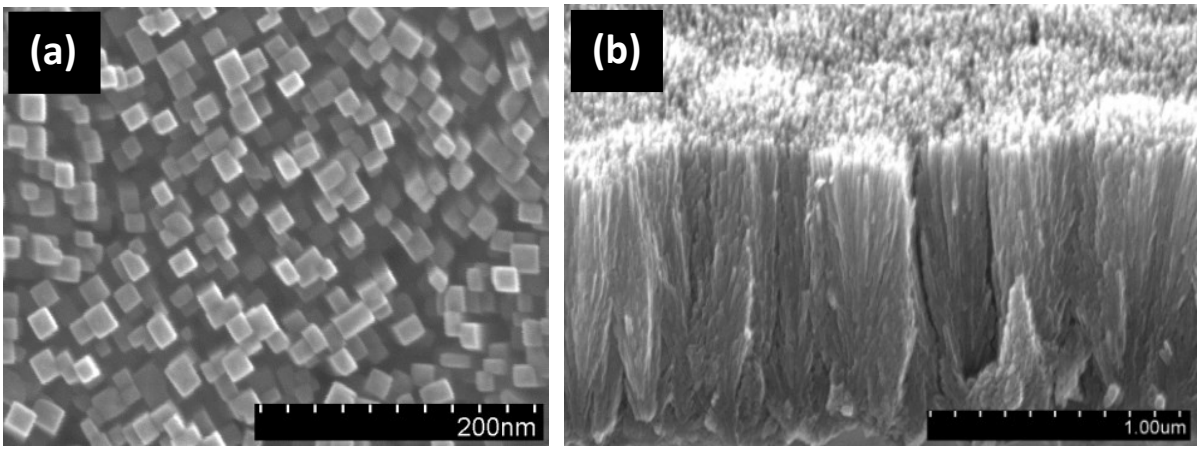

Figure 2.5 (a) Top and (b) cross-sectional view FESEM images of hydrothermally grown TiO_2 nanowire arrays.

Rutile TiO_2 nanowire arrays grown on FTO were monocrystalline which can be seen in XRD pattern spectrum shown in Figure 2.6a where a single dominant peak corresponding to the (200) reflection is observed, indicative of vertical *c*-axis orientation of the nanowires. UV-Vis spectrum of the nanowire sample is also shown in Figure 2.6b with a clear semiconductor band-edge at 405 nm together with an Urbach tail at longer wavelengths.

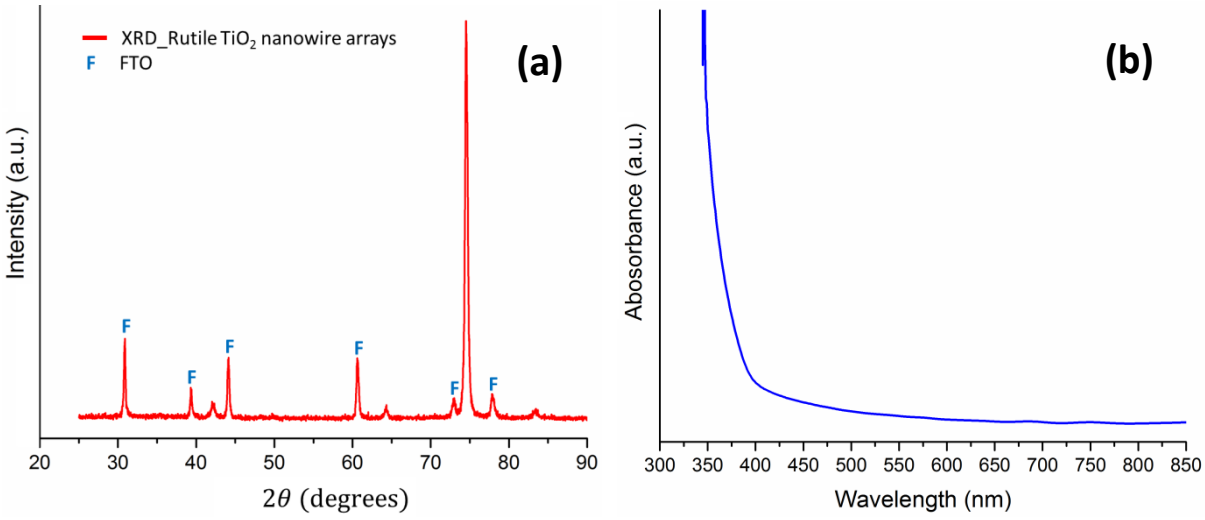

Figure 2.6 (a) XRD patterns and (b) UV-Vis spectrum of TiO_2 nanowire arrays grown on FTO.

2.3. Time of flight measurement

Time of flight measurement is a technique for studying charge transport behavior of low conductivity materials including but not limited to, intrinsic or low-doped inorganic semiconductors, wide band gap metal oxide semiconductors and organic semiconductors. Chapter 6 of the present thesis reports on time of flight measurements on single crystal TiO_2 nanowire arrays for the first time. As shown schematically in Figure 2.7, TiO_2 nanostructures need to be sandwiched between two conducting layers.

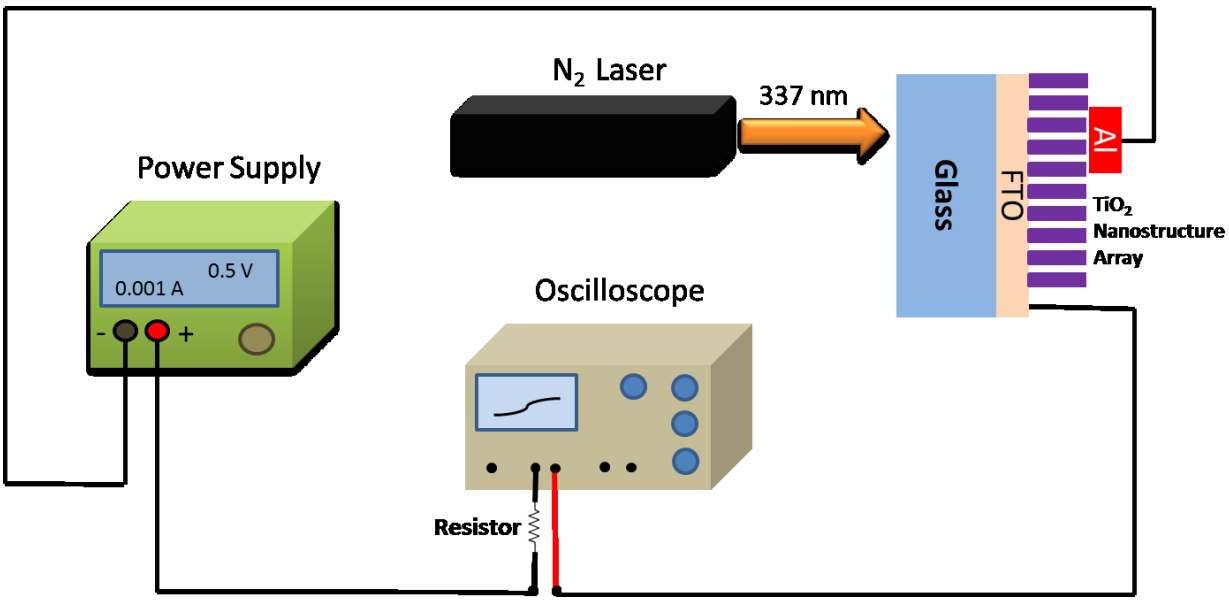

Figure 2.7 Schematic image of the time of flight measurement setup

TiO_2 nanotube and nanowire arrays were directly grown on conducting substrates such as FTO coated glass, which served as one of the contacts. The top contact was generated later by depositing a metallic layer such as aluminum. A N_2 laser was used to generate charge carriers at one end of titania nanostructures by illuminating the pulsed laser beam through transparent glass and FTO layers. In order to avoid double injection and to ensure that purely the drift of optically excited charge carriers of a single type are observed, blocking contacts are preferred; applied electric fields were typically lower than 10^5 V cm^{-1}. Transit of charge carriers along the length of the sample was stimulated by applying a potential difference between the two electrodes. Polarity of the applied voltage determined which type of charge carriers (electrons or holes) transited and which type vanished quickly due to carrier collection and/or recombination. The time that it takes for the charge carriers to travel along the length of nanostructures is an indication of their mobility in the sample and will be discussed in more details in chapter 6. The laser beam needs to meet several criteria to be suitable for TOF measurement. Penetration depth

of the beam needs to be small compared to the thickness of the sample to guarantee the generation of charge carriers at one end of the sample. In this case, the penetration depth of 337 nm laser light was *ca.* 200 nm and TiO_2 nanotube/nanowire arrays needed to be more than one micrometer in length. Pulse duration needs to be short enough to approximate a delta-function to generate charge carriers almost instantaneously (in relation to the transit time) and the pulse repetition time should be longer than transition time of charge carriers to ensure that generated charges complete their transition before new sets of charge carriers get generated. Utilized laser had the pulse duration and frequency of 4 ns and 30 Hz respectively. The laser pulse was close to rectangular and generated harmonics higher than the fundamental, a behavior intrinsic to pulse waveforms. Keeping all the above factors in mind, to measure the transit time of charge carriers, a digital sampling oscilloscope with a band-width of at least 50 MHz, a memory depth of at least 16,000 points and a sampling rate of at least 1 GSa/s was used in the circuit. Generated current passes through a resistor and enters the oscilloscope to be depicted in terms of signal voltage versus time. A higher utilized oscilloscope input resistance increases the voltage signal in oscilloscope as result of ohm's law. However a higher resistance also increases the RC time constant of the measurement circuit thereby effecting the measured time of flight value. In order to understand the dielectric relaxation time of the samples and the system response time, steady-state current-voltage (I-V) and capacitance-voltage (C-V) measurements were performed prior to TOF measurements using a Keithley 4200-SCS semiconductor parameter analyzer. A transimpedance amplifier was sometimes used but once again, the response time and bandwidth of the amplifier are critical. Hence there exists a tradeoff between measured signal strength and accuracy of measured transit time. Therefore, the sample capacitance was typically measured before the measurements, allowing estimation of the parasitic delays. Also, triggering issues

were important for transit detection and measurement. When the signal was strong, the oscilloscope could be triggered on the rising edge of the sharp initial increase in current, associated with charging of the parasitic measurement capacitances. When the signal was weak, the oscilloscope needs to be triggered on the firing of the laser pulse. Even though the pulse width was a few nanoseconds, the fast photodiode used to trigger the oscilloscope had a delay time of at least 70 ns. To compensate for this delay, a 70 ns delay was artificially introduced in the signal-to-oscilloscope line by using a 50 ft RG-58 BNC cable. A Faraday cage was used to attenuate laser noise, especially for the measurement of weak signals. Also, shielded cables were used for all connections. Arc lamps, computers and electronic equipment in the vicinity of the sample, not directly required for the experiment were turned off to minimize electromagnetic interference. An oscilloscope terminal resistance of 50 Ω was most frequently used for measuring the TOF of TiO_2 nanowire arrays but occasionally, resistances as high as 1 kΩ were used.

Chapter 3

3. Growth of large diameter TiO_2 nanotube arrays[1]

3.1. Introduction

Extending the diameter of the nanotubes to larger sizes on par with the wavelength of visible light is an important frontier in the synthesis of TiO_2 nanotube arrays. Macropore arrays with pore diameters comparable to optical wavelengths allow exploitation of the geometrical resonances due to interaction of light with the nanotube architecture which contains a high refractive index contrast between the TiO_2 (n = 2.42 for anatase) and the surrounding environment (typically air or organic solvent or polymer-depending on the application). If the pattern order of the visible wavelength-sized macropores is regulated and periodicity is produced, either by superior control of the anodization process or by seeding the pores with suitable structuring techniques, two-dimensional photonic crystals can result[174]. Macropore arrays, upon coating with organic dyes and filling with noble metals, also form excellent substrates for Surface Enhanced Raman Scattering (SERS)[175]. Optical simulations have shown that cylindrical dielectric rods with diameters in the 300 nm to 3 mm range embedded in a low permittivity matrix function as all dielectric metamaterials exhibiting negative refractive index at infrared and microwave frequencies[176]. TiO_2 nanotube array-based metallodielectric architectures have also been proposed to construct negative index material lenses at optical frequencies[177]. Apart from the applications resulting from the unique optical properties and

---

[1]Results of this work were published as a journal paper entitled "Anodic TiO_2 nanotube arrays with optical wavelength-sized apertures" in Journal of Materials Chemistry 20(39) pp. 8474-8477, 2010.

periodicity of visible wavelength-sized pores, large diameter nanotubes are also useful in drug delivery to achieve faster drug elution rates, and as catalytic surfaces and supports, adsorbents and chromatographic materials. In spite of the technological importance of pores in the 350–900 nm size regime, few bottom-up synthetic methods exist for producing materials with uniform pores at these larger length-scales. We demonstrate that anodization, a general method for producing porous valve metal oxides, can also be used to produce visible wavelength-sized pores. Macak et al.[178] formed TiO_2 nanotube arrays with diameters as large as 300 nm by anodization in electrolytes containing glycerol, water and NH_4F. Yoriya and Grimes[95] synthesized TiO_2 nanotube arrays with a pore size as large as 350 nm in an electrolyte containing DEG, water and HF. However, the pore-sizes reported by the aforementioned papers were still short of the size range of visible wavelengths. We report here for the first time, the anodic synthesis of nanotube arrays with controllable diameters in the range 350–900 nm, comparable in size to visible and near-IR wavelengths.

3.2. Experimental details

Titanium foil (99.7%, Sigma Aldrich) with a thickness of 0.25 mm was anodized for synthesizing large pore size nanotube arrays. A two electrode anodization setup was used in which both the anode and cathode were titanium foils with dimensions of 1.25 cm × 3.8 cm and 0.6 cm × 3.8 cm respectively and only half of their length was immersed into the solution. Anodization was carried out at room temperature in an electrolyte consisting of a mixture of DEG (Fisher Chemical), HF (48% solution, Sigma Aldrich) and de-ionized water. The applied voltage was 120 V and water concentration was kept constant at 1% of the solution. Subsequent to anodization, the cleaning process was completed by immersion of the foils into 0.1 M HCl for one hour followed by drying them in the oven for one hour at 100 ^{o}C. Morphology of the

nanotubes including their length, diameter, wall thickness and separation was investigated using a hot filament scanning electron microscope (SEM, ZEISS) as well as a cold cathode field-emission scanning electron microscope (FESEM, JEOL 6301F).

3.3. Results and discussion

Figure 3.1a and b show nanotubes with optical wavelength-sized pores obtained by anodization for 47 hours and 42 hours respectively at an applied anodization voltage of 120 V in DEG electrolyte containing 0.25% HF and 1% water; it can be clearly seen that most of the pores are larger than 600 nm. From the measurements of 34 nanotubes, we found the average diameter of nanotubes shown in Figure 3.1a to be 709 nm with a standard deviation of 144 nm. We found that in DEG-based electrolytes, the diameter of the nanotubes depends sensitively on both the anodization duration and the fluoride ion concentration, in addition to the usual dependence on voltage. This is in sharp contrast to the behavior in most of the electrolytes employed to perform the fabrication of anodic TiO_2 nanotube arrays where the outer diameter of the nanotubes is primarily determined by the anodization voltage within a large range of anodization durations and fluoride ion concentrations.

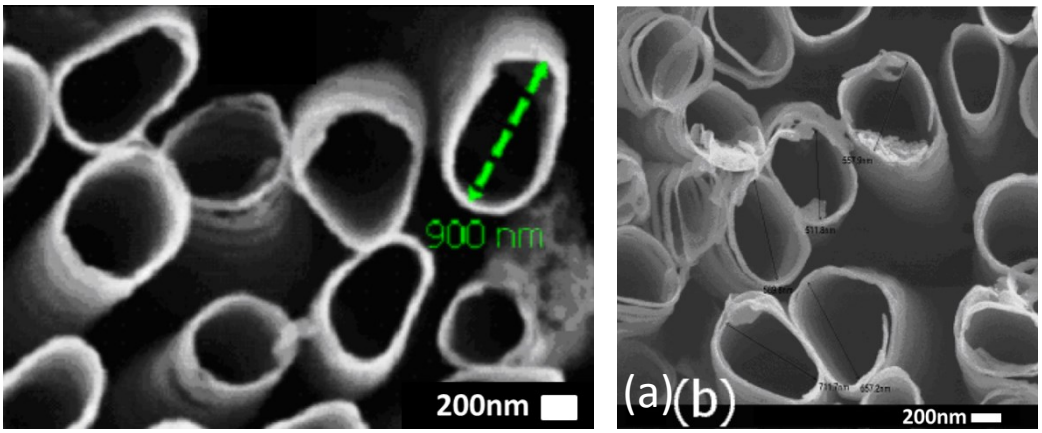

Figure 3.1 (a and b) SEM images of very large diameter nanotubes with optical wavelength-sized pores.

For instance, nanotubes of nearly identical diameter were formed by anodization at 20 V for 3 hours in a water/glycerol electrolyte containing different concentrations of NH_4F (varied from 0.135 M to 0.54 M)[178]. Similarly, Shankar et al. found that the diameter of the nanotubes formed in formamide/water/F^- electrolytes was mainly a function of anodization voltage and was only weakly dependent on the type of cation, the anodization duration or the concentration of fluoride ions[179]. We were able to generate such large diameter TiO_2 nanotube arrays due to using DEG as an organic electrolyte that introduced C into the barrier layer[180, 181] and increased its breakdown voltage by reducing its dielectric constant. Hence higher voltages could be applied in order to generate larger diameter nanotube arrays compared to aqueous electrolytes. Secondly, it was due to using an optimized electrolyte recipe which introduced a balance between the conductivity and viscosity of the electrolyte. In general, organic electrolytes result in longer TiO_2 nanotube arrays than aqueous electrolytes because of thinner barrier layer formation; hence increased ionic conductivity and concominant faster tube growth into the Ti foil. Water concentration used in this work was high enough to maintain the required conductivity for nanotube formation and was low enough to keep the chemical dissolution rate at the mouth of the nanotubes lower (by decreasing the H^+ concentration) than the growth rate at the tube bottom. More importantly it kept the electrolyte viscosity in a level that was favorable for large diameter TiO_2 nanotube growth. Thirdly, the species incident on the barrier layer were not naked ions but large diameter solvated ionic shells which while attacking the oxide surface during the pit formation process, generated large diameter pits. Fourthly, the high viscosity damped local inhomogenuities in concentration, field and ion velocities thus reducing local geometrical non-uniformities in the barrier layer. This resulted in a uniform distribution of large diameter TiO_2 nanotube arrays by eliminating localized filamentary currents.

Figure 3.2 shows nanotube arrays with different inter-tubular spacings. We have found that by tuning the processing conditions, we can tailor the spacing between the tubes in three regimes: (a) nearly close-packed architecture with adjacent nanotubes touching each other, (b) nanotubes located such that the inter-tubular spacing is approximately equal to the nanotube diameters and (c) nanotubes located significantly distant from each other where the average inter-tubular spacing is several times the nanotube diameter.

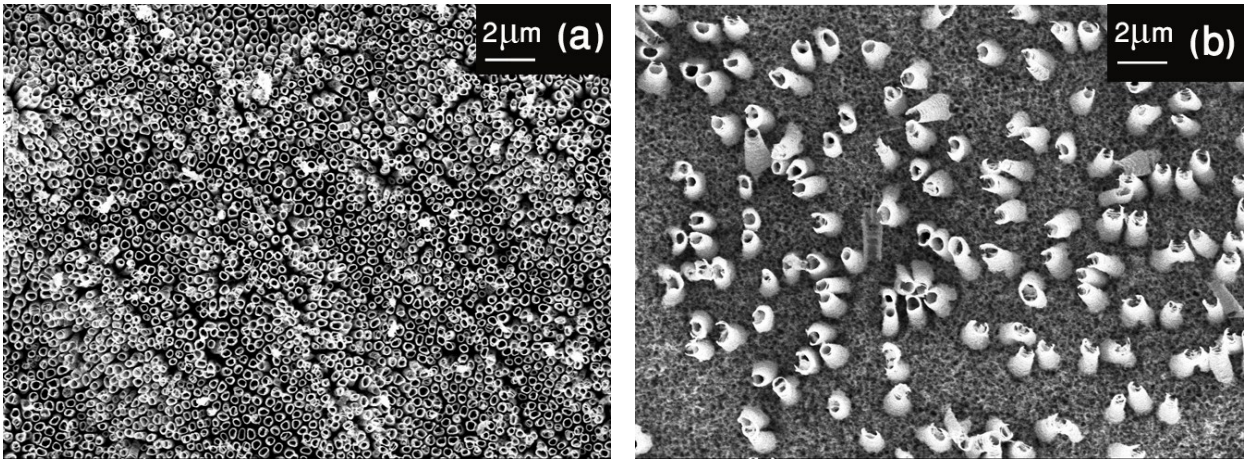

Figure 3.2 FESEM micrographs showing (a) compact close-packed nanotubes and (b) widely separated nanotubes.

While Yoriya and Grimes[95] have shown how to form nanotube arrays with separations of the order of the nanotube diameters (regime b), we demonstrate the formation of widely spaced nanotubes (regime c). For all the light harvesting device applications of large diameter nanotubes, such as photocatalysis and excitonic solar cells, the transmission, reflection and absorption of light in the pore direction are important. We have used three-dimensional finite-difference time domain (FDTD) method[182] for the first time to simulate the propagation of electromagnetic waves in the pore direction for geometrically well-defined arrays of straight large diameter TiO_2 nanotube arrays. The simulations offer an efficient way, in terms of cost and

time, to examine the optical properties of the architecture while varying the length, pore-size and wall-thickness. Although this method can be very helpful in optimizing the architecture of ever developing titanium dioxide nanotube/nanowire arrays for light harvesting applications, we are aware of only two reports on FDTD simulations of small diameter TiO_2 nanotube arrays, and in both two-dimensional FDTD simulations were performed[183, 184]. Unlike small-diameter nanotubes (diameter <50 nm) which lend themselves to a simplified analytical treatment using various effective medium theories, the size scale of the pores of large diameter nanotubes is equal to or comparable to the wavelength of light considered, so that the high refractive index contrast large diameter TiO_2 nanotube array architecture cannot be treated as an effective medium. This fact necessitates the use of a more powerful computational technique, such as one afforded by FDTD. Herein, three-dimensional (3-D) FDTD simulations of large diameter TiO_2 nanotube arrays are presented for the first time, which provide a more realistic understanding of optical properties under different illumination conditions. The presence of a finite wall-thickness differentiates the nanotube architecture from a typical macropore array. To distinguish the unique optical properties that result, we simulated both a TiO_2 nanorod architecture (with no pore) as well as TiO_2 nanotube arrays of the same diameter but possessing different finite wall-thickness. OptiFDTD 8.0 (Optiwave, Inc.) was used for simulation of TiO_2 nanotubes in which the nanotubes were characterized with respect to their length, inner diameter, outer diameter and the refractive index of the nanotube material. The mesh used for most simulations had dimensions of 25 nm, 25 nm and 30 nm in x, y and z directions respectively. The size of the time step was 4.2×10^{-17} s and each simulation was run for 5000 steps. The simulations were run one wavelength at a time on a 16-CPU computer equipped with 128 GB of random access memory (RAM). The run-time of each such simulation was approximately 150 minutes. A finer

mesh with dimensions of 5 nm × 5nm × 30 nm (X × Y × Z) was used to simulate thin-walled nanotube arrays. The optical investigation was performed in the wavelength range from 350 nm to 1000 nm in which the refractive index of TiO_2 was defined through Sellmeier equation and Lorentz–Drude model for the wavelength regions of 350–399 nm and 400–1000 nm respectively. In fact, the imaginary part of the refractive index is negligible for the wavelengths larger than 400 nm and only its real part is taken into account for that region. The Sellmeier equation has the general form of

$$n^2 = \varepsilon_\infty + \frac{A_1\lambda^2}{\lambda^2-\lambda_1^2} + \frac{A_2\lambda^2}{\lambda^2-\lambda_2^2} + \cdots \qquad (3.1)$$

in which ε_∞ is the permittivity at infinite frequency and A_i and λ_i are constants. In the present work only the first two terms of the above equation were taken into account in a way that $\varepsilon_\infty = 1$, $A_1 = 4.6$ and $\lambda_1^2 = 0.1$ for anatase nanotubes. For the wavelengths of 350, 360, 370, 380 and 390 nm where TiO_2 absorbs significantly, the Sellmeier equation was used. For wavelengths of 400 nm and larger the Lorentz–Drude model was utilized in which the dielectric function can be expressed as

$$\varepsilon_r(\omega) = \varepsilon_{r,\infty} + \sum_{m=0}^{M} \frac{G_m\Omega_m^2}{\omega_m^2-\omega^2+j\omega\Gamma_m} \qquad (3.2)$$

where $\varepsilon_{r,\infty}$ is the relative permittivity at infinite frequency, Ω_m the plasma frequency, ω_m the resonant frequency and Γ_m is the damping factor or collision frequency. In the OptiFDTD program, the parameters for Lorentz–Drude model were defined as follows: S as strength of the corresponding resonance terms, P (rad s^{-1}) as plasma frequency, R (rad s^{-1}) as resonant frequency

and D (rad s^{-1}) as collision frequency or damping factor which were considered to be 1, 1.8×10^{-16}, 8.1×10^{-15} and 0 respectively for our simulations.

The first architecture to be simulated was one consisting of 300 nm length nanotubes with a pore size of 80 nm and a wall thickness of 30 nm which were standing on a barrier layer with a thickness of 50 nm. We considered 19 × 19 nanotubes organized adjacent to each other in a square lattice in the x–y plane and oriented in the z-direction. An x-polarized Gaussian beam with a time-offset of 3.5×10^{-15} s and a half-width of 1×10^{-15} s illuminated the sample in z-direction. We used Anisotropic Perfectly Matched Layers (APMLs) absorbing boundary condition to truncate our 3-D simulations; 15 APML layers with a theoretical reflection coefficient of 1×10^{-12} were used. The results of this simulation as well as the illumination geometry are shown in Figure 3.3. The obtained transmission is qualitatively similar to the empirical transmittance data[183] of transparent nanotube arrays of similar dimensions consisting of a broad peak in the short wavelength region, a trough in the mid-wavelength region and gently rising for longer wavelengths. The differences in peak and trough position are chiefly attributable to the differences in the underlying substrate–glass in the case of Ong et al.[183] and a 50 nm thick TiO_2 barrier layer in our case. Simulations were then performed for nanotubes with optical wavelength-sized apertures. Appropriate numbers of nanotubes were used for different nanotube diameters to ensure that the same area was covered by the nanotube array in each case. In each case, the nanotubes were considered to be organized in a square lattice in the x–y plane and the two x and y directions perpendicular to the light propagation direction had the same length of 8.4 μ m, each including 21 and 12 nanotubes for those with diameters of 400 and 700 nm respectively.

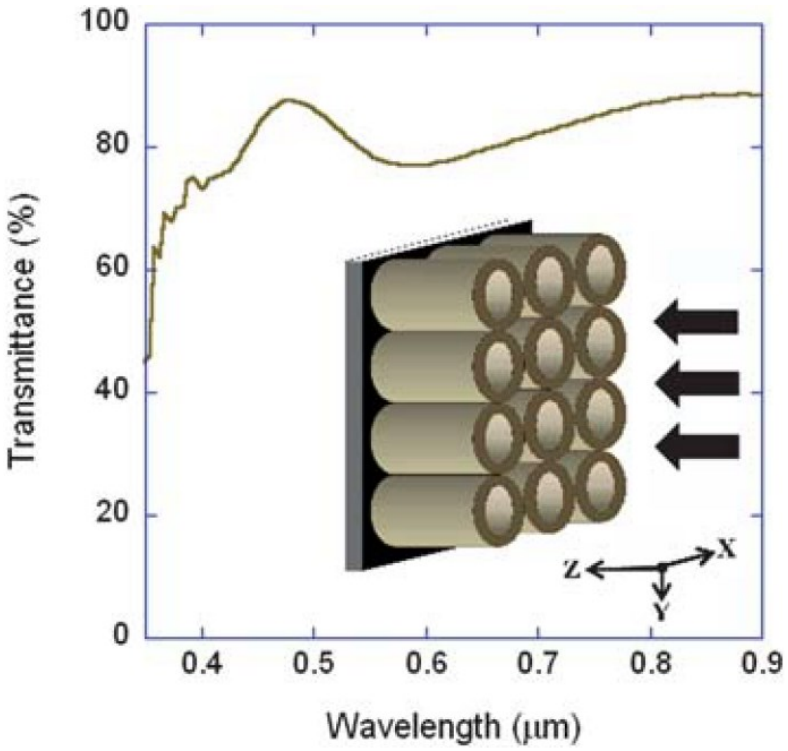

Figure 3.3 3-D FDTD simulation of the transmittance of 19 × 19 nanotubes with the length, pore size and wall thickness of 300, 80 and 30 nm respectively onto a 50 nm thick barrier layer. (Inset) Illumination geometry used for FDTD simulations.

Figure 3.4a shows a nanotube array with an average outer diameter of 400 nm formed by anodization in a DEG-based electrolyte containing 0.5% HF and 0.5% water for 49.5 hours at 80 V. Figure 3.4b shows the results of the corresponding optical simulations performed for a 2 μm thick (tube length) macroporous architecture consisting of features with an outer diameter of 400 nm and varying wall-thickness. The curve shown in red corresponds to a fully solid rod array while the curve in blue corresponds to a nanotube array with a wall-thickness of 100 nm. Figure 3.4c shows the corresponding results for an identical simulation performed for an architecture consisting of large-pore nanotubes with an outer diameter of 700 nm and varying wall-thickness. Unlike the gradual variation in transmittance with wavelength exhibited by the 300 nm long, 80

nm diameter nanotubes (Figure 3.3), the 2 μm long large diameter nanorod arrays exhibit rapid oscillations (Figure 3.4b and c) in the transmittance as a function of wavelength.

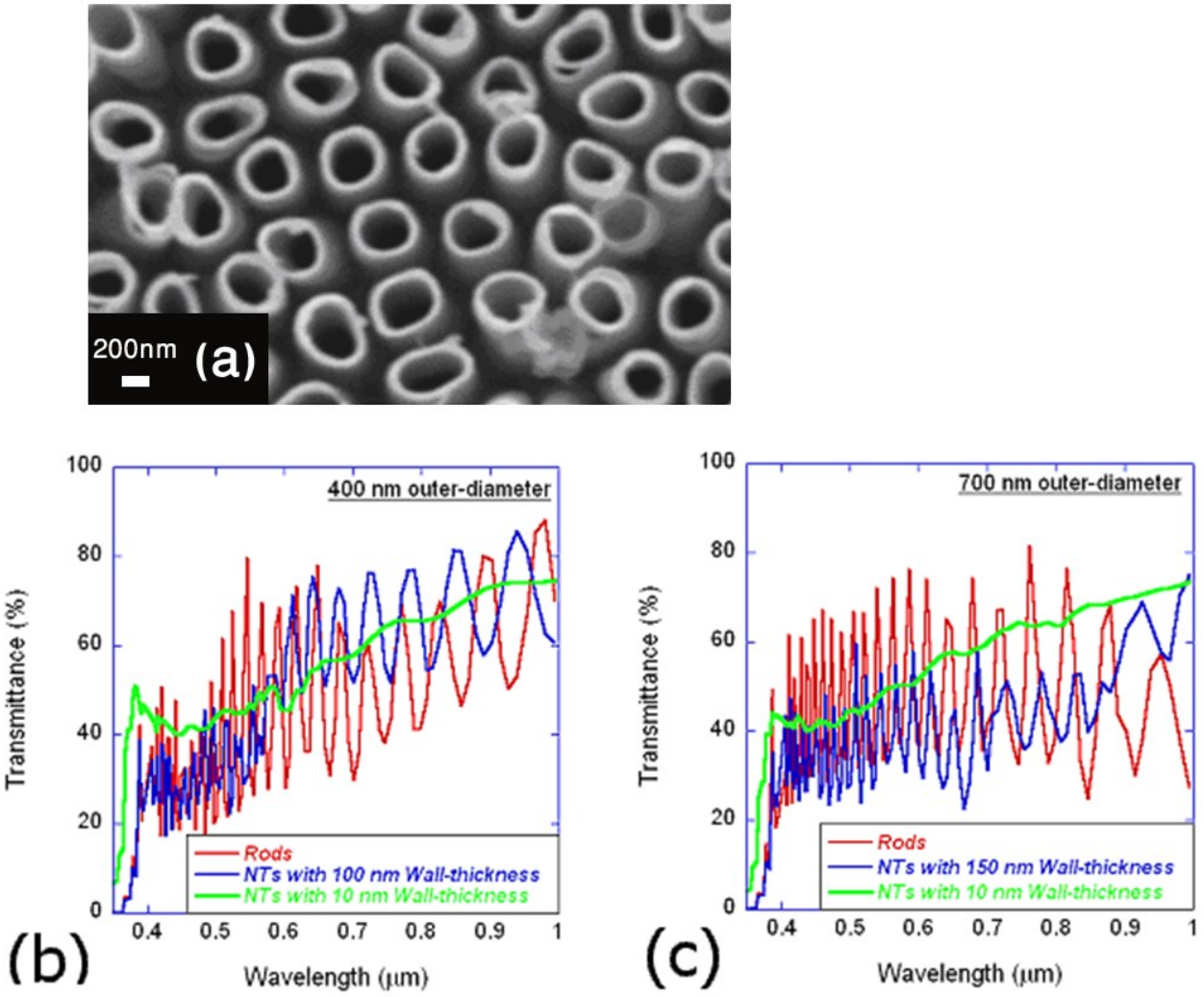

Figure 3.4 (a) SEM micrograph of an array of TiO_2 nanotubes with an average outer diameter of 400 nm. (b) Transmission through macroporous nanotybe array structures with a length of 2 μm, an outer diameter of 400 nm and varying wall-thickness. (c) Transmission through nanotubes with a length of 2 μm, an outer diameter of 700 nm and varying wall-thickness.

The oscillations depend strongly on the geometrical parameters of the nanotube array and are retained in the case of nanotubes with 100–150 nm thick walls. In our simulations, we have

assumed that the nanotubes are all of the same height, thus forming a regular top-surface. TiO_2 nanotubes longer than 1 μm grown by anodization do not, in general, present such a regular surface to incoming light. The resulting scattering would make it impossible to observe interference fringes. However, techniques to form a more regular top exist—for instance anodization in a double layer configuration has been successfully used to establish the requisite optical smoothness and obtain interference patterns from anodic TiO_2 nanotubes. The simulations show that light propagates through the TiO_2 rod array without pronounced scattering. Light propagating through large diameter nanotube arrays with a wall-thickness of 100 nm experiences some scattering but the interference pattern is still quite clear. For large diameter nanotubes with a wall-thickness of 10 nm, scattering dominates and the interference fringes are of poorer quality and barely visible. For nanotubes with very thin walls, wherein the wall-thickness is much smaller than the wavelength of light, the walls act as subwavelength Rayleigh scattering elements. Considering purely the relative volume fractions of low permittivity material (air) and high permittivity material (TiO_2), there is a more abrupt change in refractive index at the surface of the rod array compared to the tube arrays. Therefore, effective medium theories would suggest that the reflectance of the nanotubes would be much smaller than the reflectance of the nanorods through most of the visible wavelength region, resulting in increased transmittance for the tubular architectures (since the absorption of TiO_2 is negligible at visible wavelengths). However, the results of our simulations show that for TiO_2 cylinder arrays with a 400 nm outer diameter and 2 μm tube-length, nanotubes with a wall-thickness of 100 nm and 150 nm exhibit similar transmittance to the rods over much of the spectrum differing mainly in the positions of the peaks. For arrays of 700 nm diameter and 2 μm tube-length, the nanotubes have lower transmittance than the rods throughout the entire visible wavelength spectrum. Figure

3.5, which are snapshots of electric field distribution inside the TiO_2 nanotube/rod arrays when a 380 nm electromagnetic plane wave is propagating through them, shows the scattering and resonance of light within the architecture. Figure 3.5 shows the occurrence of both resonances between the discrete rods/tubes constituting the array and also within individual rods/tubes. Since the diameter of the nanorod (400 nm) is larger than the wavelength of incident light (380 nm), a discrete nanorod can accommodate waveguide modes, thus accounting for the resonances within individual nanorods in Figure 3.5a.

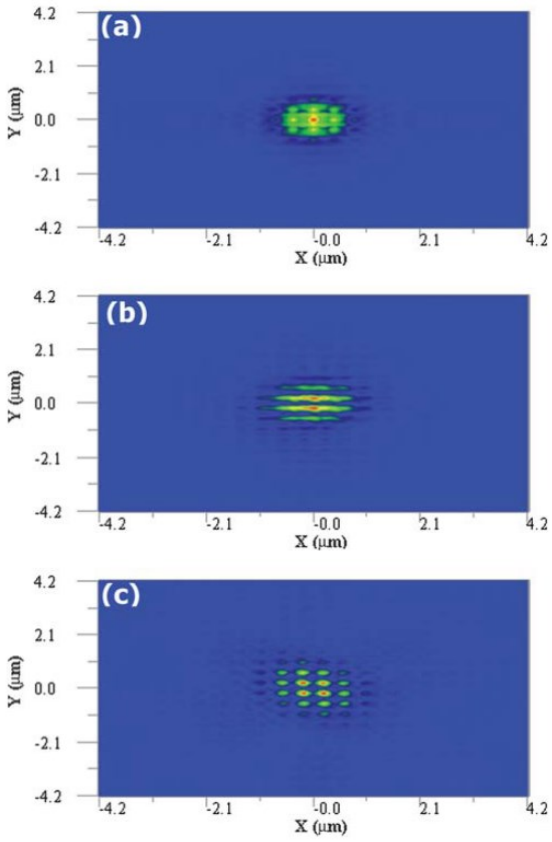

Figure 3.5 Snapshots of the electric field component (E_x) of an EM plane wave (λ =380 nm) propagating through arrays of 2 μm length and 400 nm outer diameter: (a) rods (no pore), (b) nanotubes with 100 nm wall-thickness and (c) nanotubes with 10 nm wall-thickness.

For the nanotubes of 200 nm wall-thickness (as well as for the nanorods), certain sections of the annulus in the x-direction can accommodate guided modes (of the x-polarized radiation), which also percolate between adjacent nanotubes, resulting in the elongated resonances in Figure 3.5b (and also in Figure 3.5a). For the nanotubes of 10 nm wall-thickness, the walls are too thin to significantly accommodate guided modes, due to which the resonances in Figure 3.5c are much weaker. For an infinite array of cylinders subjected to co-axial plane wave illumination (as in our case), the optical field modal structure is represented by slow (lower phase velocity) waveguide array modes mainly confined in the dielectric cylinders and fast modes which mainly propagate in the surrounding low permittivity medium[185]. Interference between the slow and the fast modes causes intensity oscillations. The fast modes are weak in the close-packed solid rod arrays and strongest in the thin-walled nanotube arrays, where the volume fraction of air is larger.

3.4. Summary

We have synthesized TiO_2 nanotube arrays with diameters similar in size to optical wavelengths. We are also able to form widely spaced TiO_2 nanotube arrays where the inter-tubular spacing is several times the nanotube diameter. The 3-D FDTD simulations presented here for the large diameter nanotubes provide a vivid picture of their optical behavior and enable us to determine what kind of architectures with respect to their pore size, wall thickness, length and separation work well for different applications. Extremely well-defined Fabry–Perot interference fringes are obtained for the TiO_2 rod arrays, both of 400 nm diameter and 700 nm diameter and for TiO_2 nanotube arrays with 100–150 nm wall-thickness.

Chapter 4

4. Growth of multipodal TiO_2 nanotubes[1]

4.1. Introduction

Despite the impressive progress in tuning the length, wall thickness, diameter, and pattern order of anodically formed TiO_2 nanotube arrays, there is still an unmet need for more complex hierarchical nanostructures which not only improve their functionality in present applications but also make novel applications possible. Applications and techniques which rely on volumetric filling or surface functionalization of nanotubes[186, 187] will particularly benefit from the production of multipodal nanotubes with a more complex topology. The differential chemical functionalization of the individual legs allows for multiplexed sensing and the loading of multiple drugs. Moreover, since the multipodal structure provides more than one leg for each of the nanotubes, a more robust attachment of nanotubes onto desired substrates is possible, which also renders them good loadbearing elements for mounting heavier structures. The branched topology of multipodal titania nanotubes consisting of a large diameter nanotube dividing at the end into several smaller size nanotubes could be applied for molecular separation in a multiphase multicomponent fluid and for microfluidic and optofluidic applications. The multipodal topology also lends itself to use in three-terminal devices, electrical interconnect networks, and nanoelectromechanical systems[188].The syntheses and applications of multipodal quantum dots (mainly tetrapodal nanocrystals of II-VI semiconductors such as ZnO, CdS, and CdTe[188]) are a focus of intense research activity.

---

[1]Results of this work were published as a journal paper entitled "Anodic Growth of Large-Diameter Multipodal TiO_2 Nanotubes" in ACS Nano 4(12) 7421-7430 2010.

The multipodal structure is highly advantageous in applications such as photocatalysis[189] and photovoltaics[190] due to the larger surface-to-volume ratio and more facile charge separation at the core-leg interfaces.

4.2. Experimental details

Titania nanotube arrays were obtained by anodization of a 0.25 mm thick titanium foil (99.7%, Sigma Aldrich) in a two-electrode anodization setup in which titanium foils were used as both the anode and cathode and only half of their length was immersed into the solution. Titanium foils were cleaned ultrasonically prior to anodization with soap, deionized water, and isopropyl alcohol and were dried with nitrogen gas. Anodization was carried out at room temperature in an electrolyte consisting of a mixture of DEG (Fisher Chemical), HF (48% solution, Sigma Aldrich), and deionized water under the applied voltages of 120 and 150 V. The electrochemical cell had a closed lid to reduce variation in electrolyte concentration with time, and the anodization was performed inside a fume hood with the sash half-closed. After anodization, the titanium foils containing the nanotubes were rinsed with isopropyl alcohol and dried in air. Subsequently, the cleaning process was completed by immersing the foils into 0.1 M HCl acid for an hour and drying it in the oven for 1 h at 100 °C.

Morphology of the nanotubes including their length, diameter, wall thickness, and separation was investigated using a scanning electron microscope (SEM, ZEISS) as well as a field-emission scanning electron microscope (FESEM, JEOL 6301F). Contact angles with the sessile drop technique and the surface tension with pendant drop technique were measured using Kruss DSA 100 (Kruss GmbH, Hamburg, Germany). For the surface tension measurement, electrolytes of different degree of aging were selected, whereas the contact angle of a fresh electrolyte on various TiO_2 substrate was measured. In the case of surface tension measurement, an image of a

drop in hydromechanical equilibrium condition is captured. DSA drop shape analysis, in-built software in the Kruss DSA 100 system, was used for the image processing to determine the surface tension and contact angle of the electrolytes. The software relies on the derivation of surface tension based on the Laplace pressure equation. As the hydromechanical equilibrium condition of the pendant drop is a more important parameter than the drop volume, the change in the drop volume was ignored during the surface tension measurement. Five measurements on each sample with a specific degree of aging were taken, and the average surface tension of the corresponding electrolytes was determined. For the contact angle measurement, the drop was disposed from needle to obtain a sessile drop on the substrate. It was observed that the substrate shows perfect wetting conditions. Further details of such measurement procedure can be found elsewhere[191].

4.3. Results and discussion

To the best of our knowledge, multipodal titania nanotubes have not been reported so far. Herein we report on the production of multipodal titania nanotubes (see Figure 4.1) which result from a newly introduced process that we call nanotube combination. Almost every nanotube in the images of Figure 4.1a and b 1b is at least bipodal. Figure 4.1c shows two bipodal nanotubes in the process of forming a tetrapodal nanotube, while Figure 4.1d is a tetrapodal nanotube, which appears bipodal at first glance because the process of nanotube combination for the constituent bipodal nanotubes is complete. We propose a mechanism that explains the formation of multipodal nanotubes and also explains some of the unique features associated with the growth of TiO_2 nanotube arrays in DEG-based electrolytes. Anodization in DEG-based electrolytes exhibits some unusual features such as the formation of nanotubes with very large pore sizes (up to 900 nm)[192] and discretization of nanotubes by large intertubular spacings[95, 192,

[193], a deviation from the close-packed architecture found in other electrolytes. Our studies indicate that the process of nanotube combination has a decisive role in the simultaneous increment of the both pore size and intertubular spacing of nanotube arrays anodically formed in a HF containing DEG electrolyte.

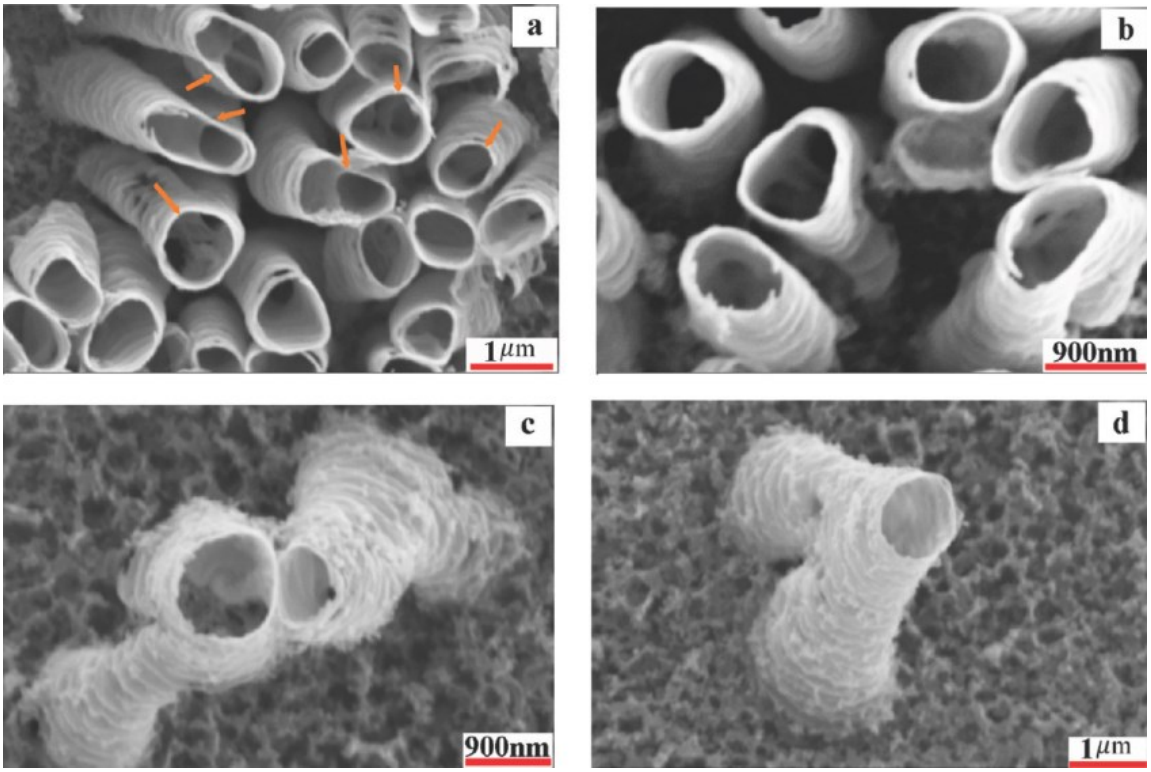

Figure 4.1 SEM images of multipodal titania nanotubes anodized in a DEG electrolyte with 0.25% HF and 2% water (a) at 120 V for 44 h, (b) at 120 V for 47 h, and (c,d) at 150 V after 47 h. Arrows in panel a point to easily identifiable multipodal nanotubes not obscured by the topology or tilt angle.

Field-assisted oxide dissolution and cation migration, field-assisted oxidation of Ti, and chemical etching are the competing reactions responsible for the growth of TiO_2 nanotube arrays (a key difference from the formation of nanoporous alumina, in which only the field-assisted processes are important). The field-assisted reactions occur on either side of the barrier layer at the bottom of the nanotubes and are responsible for driving the Ti/TiO_2 interface deeper into the

Ti foil, a process that increases the length of the nanotubes. Chemical etching shortens the length of the nanotubes[50, 194].

Field-assisted oxidation: $Ti + 2H_2O \longrightarrow TiO_2 + 4H^+ + 4e^-$ (4.1)

Field-assisted migration: $Ti^{4+} + 6F^- \longrightarrow [TiF_6]^{2-}$ (4.2)

Field-assisted dissolution: $TiO_2 + 6F^- + 4H^+ \longrightarrow [TiF_6]^{2-} + 2H_2O$ (4.3)

Chemical dissolution: $TiO_2 + 6HF \longrightarrow [TiF_6]^{2-} + 2H_2O + 2H^+$ (4.4)

Nanotubes formed in HF-bearing DEG-based electrolytes at large anodization potentials exhibit a definite taper with a wider base and a narrower mouth, as shown in Figure 4.2a. The taper occurs as a consequence of the significant variation in the conductivity of the electrolyte, which occurs over the course of the anodization process. The low conductivity of the DEG-based electrolyte has been remarked upon by others[95] and occurs due to a combination of three factors: (a) the high viscosity of DEG and the concominant low ionic mobilities;[195] (b) low concentration of ionic charge carriers due to low dissociation of the weak acid (HF); and (c) large hydrodynamic radius of dissociated ions due to solvation[179] by water and DEG molecules. As the anodization of Ti proceeds, the concentration of $(TiF_6)^{2-}$ ions increases with time due to the chemical reactions represented by eqs 4.2, 3, and 4. Due to a more delocalized distribution of charge in the complex[196], $(TiF_6)^{2-}$ ions are also less solvated and therefore more mobile. Consequently, the conductivity of the electrolyte increases with anodization duration, which manifests itself in a higher anodization current density at the same potential, an effect clearly seen in the anodization current transient plot of Figure 4.2b, during the first 20 h of anodization. The increase in the conductivity of the electrolyte makes a large proportion of the applied

anodization potential available for the anodization process since the potential drop across the electrolyte (anodization current i × electrolyte resistance R) reduces with time. Therefore, the base of the nanotubes which form later in the process experiences higher effective anodization voltages than the top (mouth) of the nanotubes, which are formed relatively early in the process.

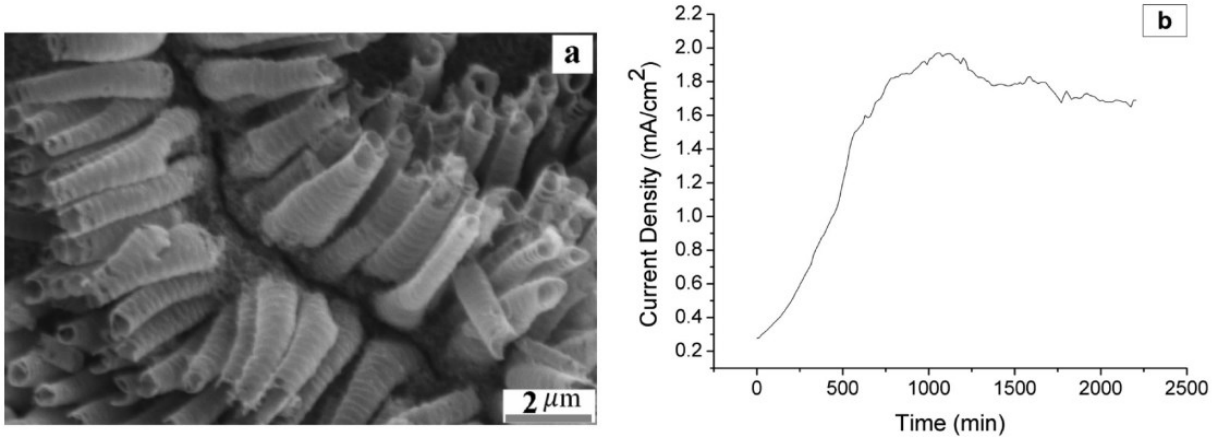

Figure 4.2 (a) SEM image of the cross section of titania nanotubes formed by anodization at 120 V in a DEG electrolyte with 0.25% HF and 1% water, showing a clear taper from mouth to base. (b) Anodic current density as a function of anodization time for 120 V anodization identical DEG electrolyte (0.25% HF and 1% water).

Due to the well-known dependence of the diameter of the nanotubes on the anodization voltage, a tapered nanotube morphology wider at the base than at the top is produced. The field-assisted oxidation process generates H^+ ions according to eq 4.1 and results in local acidification at the pore bottom[197]. On the other hand, F^- ions are consumed by dissolution reactions. Therefore, while F^- concentration is maximum at the mouth of the tubes (nearly equal to concentration in the bulk electrolyte) and drops to a minimum at the pore bottom, H^+ ion concentration is maximum at the pore bottom and decreases toward the mouth of the tubes. Such a fluoride ion concentration gradient along the length of the nanotubes has been confirmed by compositional analysis using X-ray photoelectron spectroscopy (XPS)[198]. It is also fairly well-

known that less fluoride results in a thick oxide layer which suppresses the transport of titanium, oxygen, and fluorine ions, and excess fluoride results in a thin oxide layer that enhances the transport of titanium, oxygen, and fluorine ions, thus inducing inward growth faster[199]. Nanotube length increases so long as the rate of movement of the Ti/TiO_2 interface is faster than the rate of loss of TiO_2 nanotubes by chemical etching. The anodization current is roughly proportional to the strength of the field-assisted reactions and is thus indicative of the rate at which the Ti/TiO_2 interface is moving into the Ti foil[200]. As shown in Figure 4.2b, the anodization current increases for the first ~20 h of anodization and then decreases nearly monotonically. As discussed previously, the increase in anodization current occurs due to an increase in electrolyte conductivity. Thus the rate of movement of the interface peaks ~20 h into the anodization process and declines thereafter due to a paucity of fluoride ions at the pore bottom. At this point in the anodization process, field-assisted dissolution weakens relative to field-assisted oxidation, resulting in an increase in the thickness of the barrier layer.

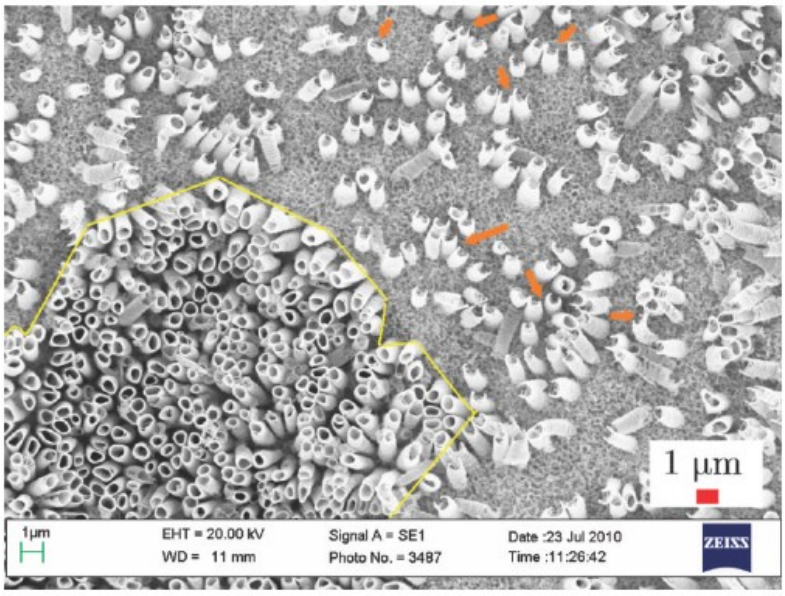

Figure 4.3 SEM images of the surface of a Ti foil anodized in a DEG-based electrolyte containing 0.25% HF and 1% H_2O for 43 h at 120 V. Two distinct regions consisting of close-packed and widely separated nanotubes are demarcated by the yellow border.

The thicker barrier layer retards the solid state ionic transport of reactants through the barrier layer and causes a decrease in the anodization current density. If purely high-field ionic conduction was involved, then the current would be expected to continuously decrease with time. If this was purely a mass transfer limited process, the anodization current would be expected to level off instead of decreasing. In our scheme, the anodization reaction is under mixed control of the high-field solid state ionic transport and mass transport. Chemical etching, in contrast, is relatively constant and becomes more dominant as the anodization current decreases. We propose a mechanism that explains our observations and accounts for the unique formation of multipodal TiO_2 nanotubes in HF/DEG/water electrolytes. As mentioned previously, a gradient in fluoride-bearing species exists along the length of the growing nanotube, with the highest concentration corresponding to that of the bulk existing at the mouth of the tube and decreasing toward the barrier layer. Consequently, in the first 20 h of the anodization process, when nanotubes are increasing in length, chemical etching, even though isotropic, only shortens the height of the nanotubes by etching from the top. The solid state transport of reactant ions through the barrier layer occurs through a high-field process exponentially dependent on the electric field across the barrier layer and therefore sensitive to barrier layer thickness. When the anodization current begins to decrease after 20 h, there is increased competition for the lower current from all of the nanotubes and minor variations in barrier layer thickness play a significant role in allocating current among nanotubes. As chemical etching becomes more dominant, nanotubes in regions where the barrier layer is slightly thicker grow into the Ti foil more slowly but experience the same rate of chemical etching, thus gradually becoming shorter than nanotubes in regions where the barrier layer is slightly thinner. Due to the tapered structure of the nanotubes, a decrease in the height of such nanotubes also increases intertubular spaces where the viscous

bulk electrolyte (richer in fluoride) can now penetrate thus the same nanotubes experience more accelerated rates of dissolution due to chemical attack from the sides in addition to etching from the top. Soon, these nanotubes are completely consumed. Also, since the Ti/TiO_2 interface in the regions of thicker barrier layer moves into the metal more slowly, these regions are gradually more elevated with respect to adjacent regions with a thinner barrier layer. This effect is clearly seen in Figure 4.3, which shows two such regions adjacent to each other. The region enclosed by the yellow border in Figure 4.3 has relatively close-packed nanotubes as well as dark regions indicative of depth and greater topographic contrast. The barrier layer is visible in the region outside the yellow border, which is lighter on account of being at a higher elevation. In this elevated region, several nanotubes have been consumed by chemical etching, resulting in a wider separation. Several of the still-remaining nanotubes in this region have experienced severe side wall etching (some of these are pointed out by the orange arrows in Figure 4.3).

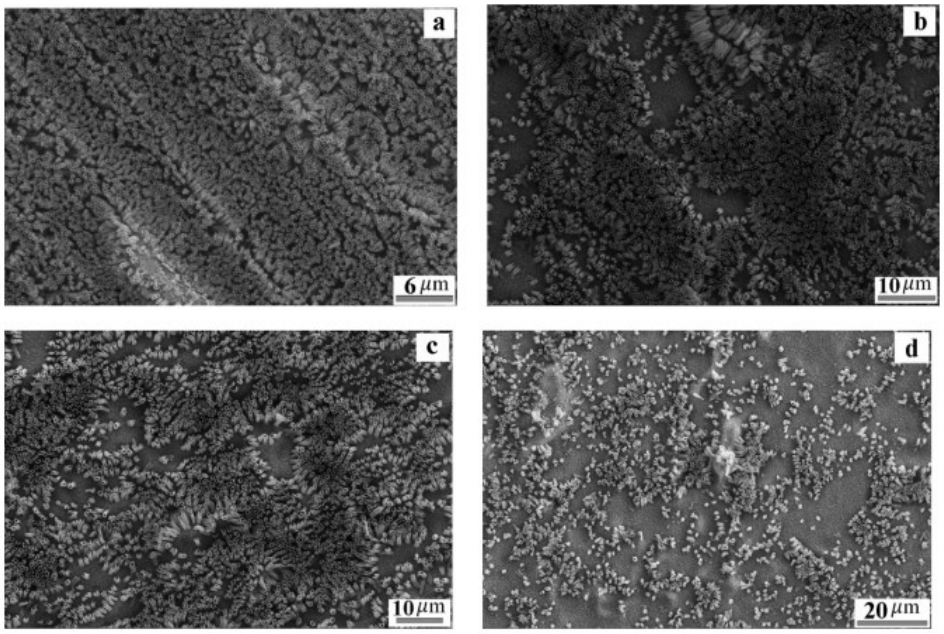

Figure 4.4 SEM images of titania nanotubes anodized at 120 V in a DEG electrolyte with 0.25% HF and 1% water after (a) 40 h, (b) 43 h, (c) 45 h, and (d) 47 h.

Figure 4.4 shows SEM images of the obtained titania nanotube arrays at different anodization times. After 40 h of anodization (Figure 4.4a), the nanotubes are still fairly close-packed, but from this point onward, chemical etching becomes dominant. From Figure 4.4b-d, it can be clearly seen that the nanotube structures become successively less close-packed in the course of the next few hours, resulting in a dramatic decrease in the areal density of nanotubes on the substrate. The absence of side wall chemical etching in the regions of closely packed nanotubes preserves those nanotubes. Nanotubes of very large diameter (extending to optical and near-infrared wavelengths) may be obtained in DEG electrolytes[192], as seen in Figure 4.5a,b. Two concurrent processes are responsible. Although closely packed nanotubes do not undergo significant chemical etching of their side walls, they do experience etching from the top, which shortens them because of the presence of the electrolyte at their mouth.

In process I, nanotubes of large pore size are formed by the top- etching process, which increases their diameter due to their tapered conical shape. In process II, nanotubes of large pore size form by the combination of small pore size ones. As shown in the diagram of Figure 4.5c, the pore size of both process I (individual nanotubes) and process II (multipodal nanotubes) was increased for longer anodization times subsequent to the formation of the self-organized nanotubular structures on the surface, growing from just more than 300 nm after 40 h of anodization to about 900 nm after 47 h for combined nanotubes. The reason for the pore size increment of the process I nanotubes is shown schematically in Figure 4.5d. The nanotube combination process is schematically shown in Figure 4.5e, in which Figure 4.5e (step I) represents the common surface area of the two leaning nanotubes.

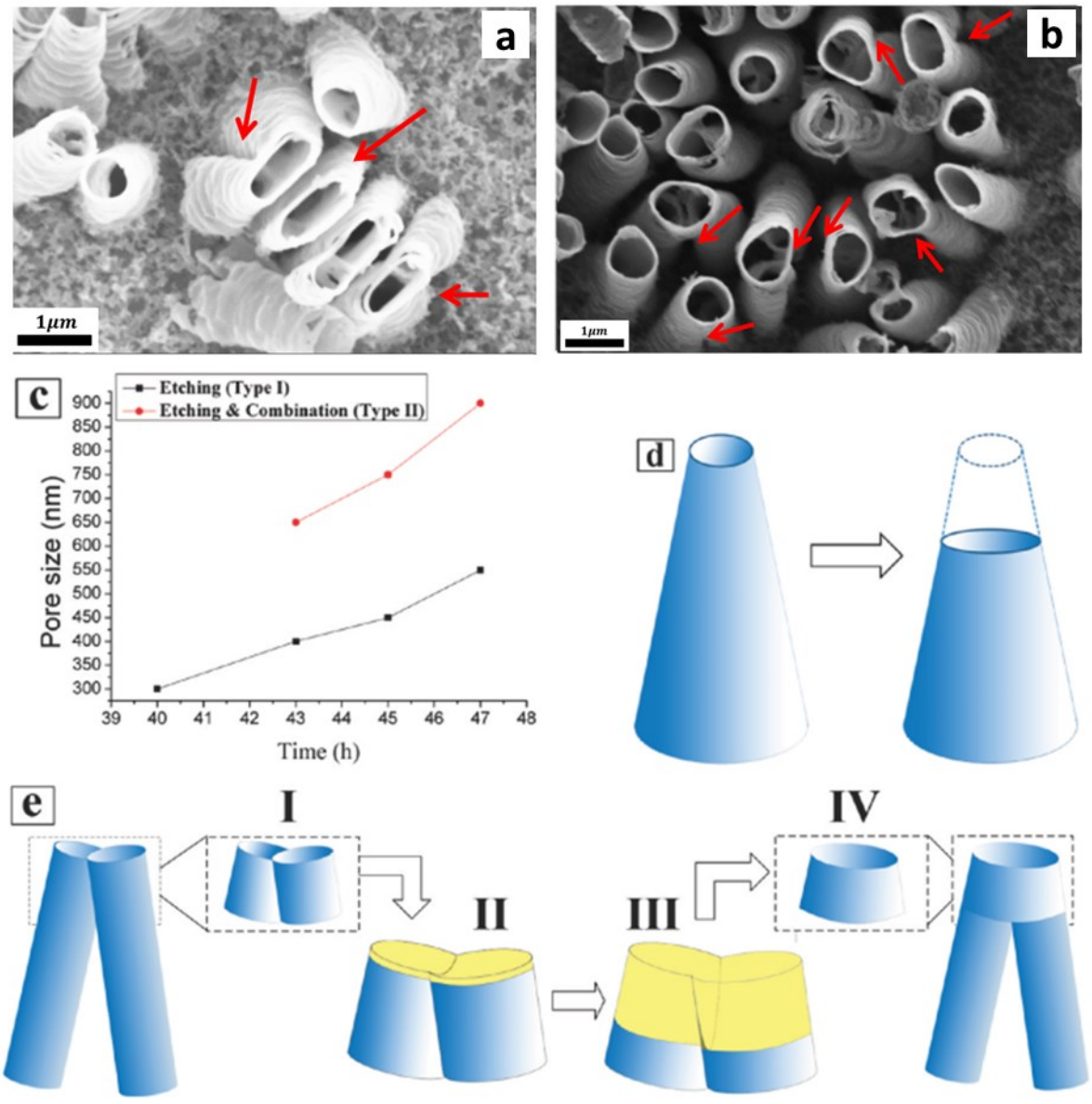

Figure 4.5 SEM images of titania nanotubes anodized at 120 V in a DEG electrolyte with 0.25% HF and 1% water (a) after 45 h of anodization and 1 h in the same bath without electric field. Four consecutive bipodal nanotubes can be seen and (b) top view after 45 h of anodization. (c) Pore size increment diagram of the individual and combined nanotubes vs anodization time and schematic image of the pore size increment in (d) individual and (e) combined nanotubes.

Like EG and water, DEG is a highly structured solvent with a three-dimensional spatial network of hydrogen bonds. It is known that H^+ ions, OH^- ions, and glycoxide ions have anomalously high conductance and mobility in these electrolytes due to the proton jump

mechanism. Halide ions, on the other hand, have much lower conductance and mobility in EG and DEG[201]. A consequence of this asymmetry is that hydroxyl ions and glycoxide ions consumed at the Ti/TiO_2 interface during oxidation are replenished from the bulk electrolyte more quickly than fluoride ions consumed in the electrochemical dissolution of the barrier layer, and this asymmetry becomes more pronounced as nanotube length increases. Also, the bulkier $[TiF_6]^{2-}$ ions produced at the pore bottom do not disperse quickly into the bulk electrolyte due to their low mobility in the viscous electrolyte and their Coulombic attraction to the anode. It should be mentioned that the chemical etching at the nanotube mouth occurs continuously and the high viscosity of the electrolyte limits the long distance movement of the dissolved material, which increases its concentration in the electrolyte/nanotube interface region. As depicted in Figure 4.5e (step II), this highly saturated electrolyte etches both the side wall and interface between the leaning nanotubes, the small amount of saturated electrolyte at the mouth becomes supersaturated, and additional dissolved nanotube material becomes deposited onto the inner surface of the nanotube (the electrolyte/nanotube interface). Hence, the side wall becomes thicker, which results in the reduction of in chemical etching rate relative to that of the nanotube interwall. The SEM images in Figure 4.5a,b clearly show this stage after 45 h anodization with the same electrolyte mentioned before. According to Figure 4.5e (step III), the difference in the chemical etch rate dissolves the interwall deeper into the nanotube, which results in the combination of nanotubes leaning toward each other, as seen in the SEM image in Figure 4.1d for 47 h of anodization. As can be seen in Figure 4.5a,b, if the leaning nanotubes possess a larger interface from top to bottom, the resulting combined nanotube looks like a single large pore size nanotube; otherwise, it would be a multipodal large diameter nanotube having several legs depending on the number of combined nanotubes. Less than 40 h of anodization resulted in a

closely packed compact nanotube architecture. To investigate the effect of the presence of electric field in preserving the nanotubes against the chemical etching, the electric field was removed after 40 h of anodization, and the results for different etching times are provided in Supporting Information. It can be clearly seen from Figure 4.5a that, during the first hour after voltage removal, the combination process was at its initial stage and the interwall between the nanotubes is still visible and has not etched very deeply into the nanotubes. Nevertheless, at longer times, the nanotubes are completely etched and an irregular film is redeposited from the supersaturated electrolyte (Figure 4.6a, b and c).

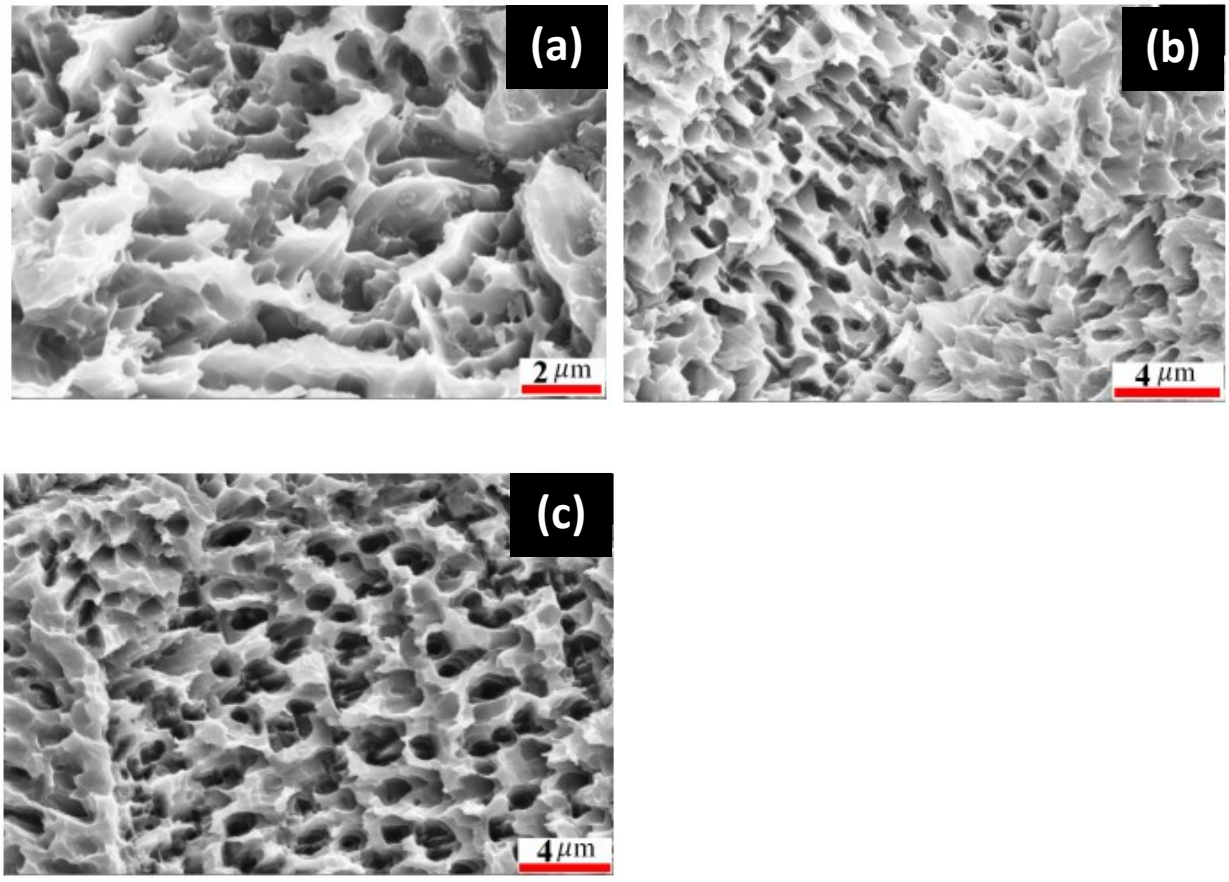

Figure 4.6 SEM images of titania nanotubes anodized at 120V in a DEG electrolyte with 0.25% HF and 1% water for 40 hours and etched without applied voltage for 5 h (a), 7 h (b) and 8 h (c).

It is clear from SEM images, such as those in Figure 4.1c, d and Figure 4.4a, b, that the nanotubes bend before combining. Bending and bunching of high aspect ratio (AR > 150) TiO_2 nanotubes grown in fluoride-ion-bearing glycerol water electrolytes has been previously observed due to surface tension effects during the drying process. By supercritical drying in CO_2 , such bending has been minimized or even eliminated[202]. The nanotubes formed in the present study have much lower aspect ratios of ~5-25, therefore implying that the force causing the bending is much larger. We present a theoretical analysis to support the bending of nanotubes to form bipodal nanotubes based on the calculation of deflection of the nanotube due to the capillary force on its surface. The capillary force is exerted on the nanotubes by the wetting of the electrolyte during the growth of the nanotubes. With high-viscosity ionic liquids, Roy et al.[203] found that preferential wetting occurred in the intertubular spaces of TiO_2 nanotube arrays. Furthermore, hardly any penetration of the ionic liquid into the nanotubes occurred even after 5 h, whereas the intertubular spaces were wetted. The wetting in such a scenario takes place preferentially between the nanotubes only, and the electrolyte penetration into the nanotubes is minimal[203]. In the present study using highly viscous DEG electrolytes, it is assumed that such wetting takes place along the circumference of the tubes only, which creates a circumferential interface formed between the nanotubes. The separation distance between the nanotubes is termed as the base separation distance (BSD). On the basis of the wetting properties of the electrolyte and the surface of the nanotubes, such as the surface tension of the electrolytes and contact angle of the same electrolyte with the nanotube surface, one can determine the capillary force as

$$F_c = \pi \gamma_{LV} \sin\theta \sin\phi D_0^t \qquad (4.5)$$

where, γ_{LV} is the surface tension of electrolyte, θ is the static equilibrium contact angle of the electrolyte with the nanotube surface, ϕ is the taper angle of the nanotube at the base, and D_0^t is the outer diameter of the nanotube at distance L from base, that is, at the tip of the nanotube. It is assumed that this is the only force responsible for the deflection of the nanotube at the tip. One can determine the deflection of the nanotube of Young's modulus E with capillary force as the pre scribed load at the tip as follows

$$\sigma_t = \frac{F_c L^3}{3EI} \tag{4.6}$$

where the moment of inertia I can be determined with the geometrical dimensions of the nanotubes. As anodized TiO_2 nanotubes are amorphous. The density of amorphous TiO_2 is known to vary from 3.0 to 4.0 depending on the conditions of growth[204]. We calculated the deflection of titania nanotubes in DEG due to capillary forces for limiting cases of the density of amorphous TiO_2, 3.88 g cm^{-3} representative highly dense TiO_2 tube walls and 3.0 g cm^{-3} for the condition of amorphous TiO_2 of much lower density. Figure 4.7 shows the variation in the deflection of the nanotube with different contact angles of the electrolytes. The point of attachment is the length at which the deflection of the nanotube crosses half the distance between the nanotubes (i.e., 0.5 times the tip separation distance (TSD)). The tapered configuration of the nanotubes has a direct bearing on the calculation of I and the capillary force. It is observed that for lower contact angle, that is, 20° with surface tension of 0.06 N/m, the magnitude of the deflection is too small to achieve the point of attachment. Further increment in the contact angle increases the deflection for the same length of the nanotube.

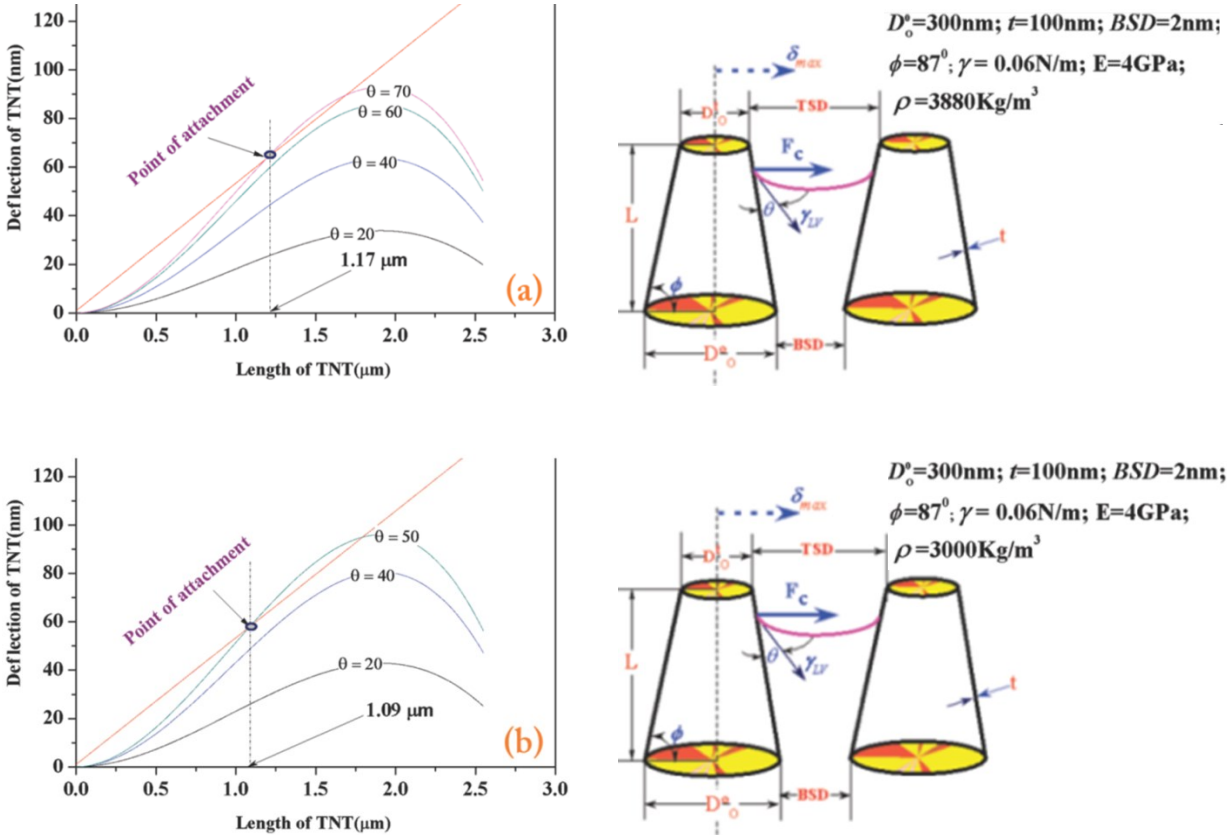

Figure 4.7 Variation in the deflection of the nanotube with the increment in the length of the nanotubes under different contact angle conditions assuming the density of amorphous anodized TiO_2 to be (a) 3.88 g cm3 and (b) 3 g cm3. BSD and TSD are the base separation distance and tip separation distance, respectively.

Under the assumption that the amorphous TiO_2 constituting the nanotube walls is highly dense (3.88 g cm^{-3}), the point of attachment is obtained for a contact angle of 70° and a tube length of 1.17 μm. When the amorphous TiO_2 is assumed to be less densified (3.0 g cm^{-3}), the nanotubes are easier to deflect. Therefore, for this case, the point of attachment occurs at a much lower contact angle of 50° but the tube length remains very similar at 1.09 μ m. The exact nanotube length at which combination occurs is not known; however, the point of attachment is inferred from SEM images to be in the range of ~1-2 μm, which supports the present analysis. It is to be noted that the measured value of the surface tension of electrolyte

(98.75DEG + 0.25HF + 1H_2O) increases from 0.386 to 0.403 N/m for 56 h, whereas with the same electrolytes, the TiO_2 nanotube array substrate shows perfect hydrophilic conditions. It is known that the chemical process and the operating conditions during the growth of the nanotubes have the ability to alter the surface tension and the contact angle in comparison to those measured values under ex situ sessile and pendant drop methods. Also, the nanoscopic surface roughness of the tube walls[205] affects imbibition, and their surface charge[205] can influence the contact angle of the liquid on the nanotubes. However, we ignore these effects in our simplified model. Hence, it is conceivable that the actual value of surface tension and contact angle are within the prescribed limits of those presented in Figure 4.7. Such a process-dependent change in contact angle for completely hydrophilic surfaces has been reported in the literature[206, 207]. There are reports of branched pores in anodically formed nanoporous alumina[208] and nanotubular titania[209]. In those reports, the branched pores with the inverted Y configuration were the result of modifying the growth parameters such as the anodization voltage or the temperature during anodization. In our case, we do not deliberately modify any growth parameters during the anodization. Furthermore, the operating mechanism is entirely different we have shown that the nanotubes are grown in a nonbranched fashion and become branched due to a process called nanotube combination. In our process, distinct nanotubes combine together, which is why we call the structures multipodal nanotubes instead of branched nanotubes. An important consequence of the mechanism being different is the ability to form multipodal nanotubes wherein the angle between the constituent nanotubes (branches) is large (> 20°). SEM images in Figure 4.1c,d and Figure 4.8 show several multipodal nanotubes where this angle is large. On the contrary, in the branching process reported in other papers (inverted Y), only a very narrow range of internanotubular angles are possible. Nanotube combination efficiently allocates scarce fluoride-

bearing species since two or more nanotubes can obtain fluoride-bearing species from the same puddle of bulk electrolyte after nanotube combination. Consequently, multipodal nanotubes that obtain access to fluoride-bearing species in the bulk electrolyte by the process of pore combination continue to grow subsequent to attachment (the Ti/TiO_2 interface below them keeps moving deeper into the Ti metal). This is clearly evident in Figure 4.8, where multipodal nanotubes are able to survive much longer than others subsequent to the first 40 h of anodization, when field-assisted processes weaken, leaving chemical etching dominant.

This is why we propose that the weaker dissociation of HF, which results in fluoride ion scarcity, and the nature of the solvent (DEG in this case) used to form the electrolyte are the critical factors for nanotube combination. When ammonium fluoride (which has higher dissociation) and tetrabutyl ammonium fluoride (which dissociates completely) are used instead of HF as the fluoridebearing species in the anodization electrolyte, F^- ions are not scarce, the formed nanotubes remain close-packed for very long anodization durations, and the diameters are capped at ~300 nm.

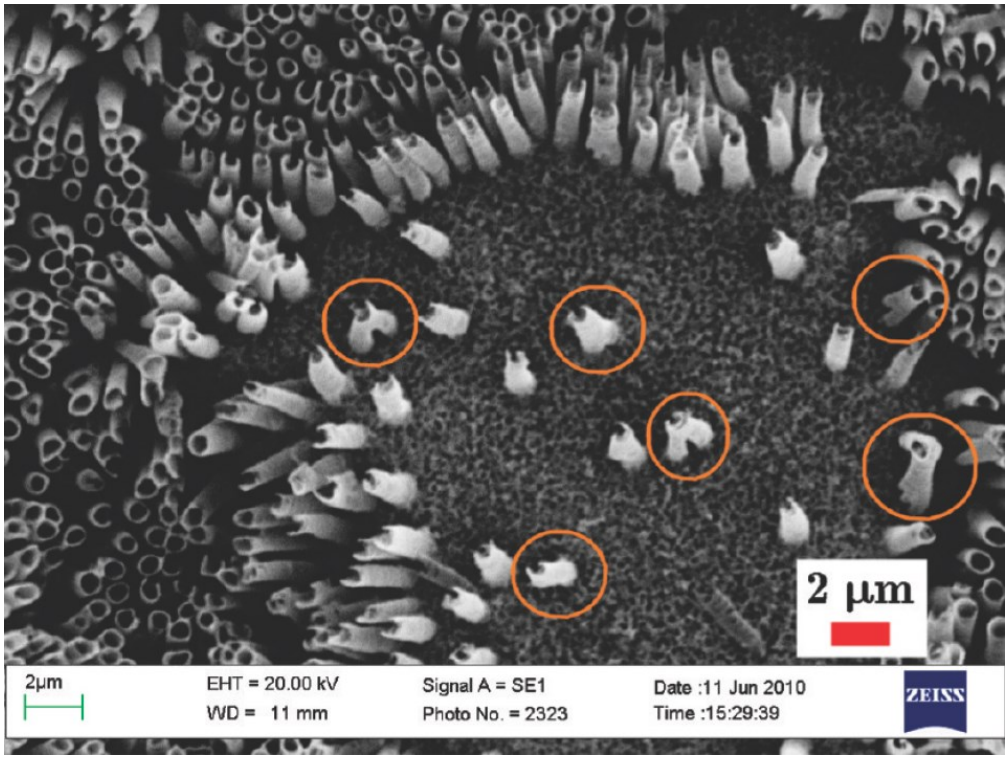

Figure 4.8 SEM image of the surface of a Ti foil anodized in a DEG-based electrolyte containing 0.25% HF and 1% H_2O for 45 h at 120 V. Similar to Figure 4.3, two distinct regions consisting of close-packed and widely separated nanotubes are seen; however, the chemical dissolution of the widely separated nanotube region is more advanced. Note how a majority of the surviving nanotubes in the chemically etched region are multipodal (orange circles point to obvious multipodal nanotubes; other surviving nanotubess are likely multipodal, too, but with one or more legs obscured).

We observe the formation of multipodal nanotubes in a narrow window of process parameters in DEG electrolytes: anodization voltages of 120 V or greater, anodization durations >40 h and HF concentrations lower than 0.5%.

Chapter 5

5. Förster resonance energy transfer through placement of chromophores in void & wall geometry[1]

5.1. Introduction

We report on a hierarchical nanoarchitecture wherein distinct chromophores are deterministically placed at two different types of sites in a nanoporous metal oxide framework. One chromophore, namely Tris(8-hydroxyquinoline)aluminium(III) (Alq_3), is embedded in the 1-2 nm sized nanovoids of anodic aluminum oxide (AAO) and another chromophore (carboxyfluorescein or pyrenebutyric acid) is anchored in the form of a monolayer to the surface of the walls of the cylindrical nanopores (~20 nm in diameter) of AAO. We found the luminescence maximum to occur at 492 nm, blueshifted by at least 18 nm from the value in solutions and thin films. The excited state decay of Alq_3 molecules in nanovoids was found to be biexponential with a fast component of 334 ps and a slower component of 2.26 ns, significantly different from Alq_3 thin films and solutions. Using a combination of steady state and time-resolved luminescence studies, we found that efficient Förster-type resonance energy transfer (FRET) from Alq_3 in the nanovoids to the carboxyfluorescein monolayer could be used to pump the emission of surface-bound chromophores. Conversely, the emission of nanovoid-confined Alq_3 could be pumped by energy transfer from a pyrenebutyric acid monolayer.

---

[1]Results of this research work were published as a journal paper entitled "Photophysics and Energy Transfer Studies of Alq3 Confined in the Voids of Nanoporous Anodic Alumina" in Journal of Nanoscience and Nanotechnology 13, pp. 2647-2655, 2013.

Such intra-nanoarchitecture interactions between chromophores deterministically placed in different spatial locations are important in applications such as organic light emitting diodes, chemical sensors, energy transfer fluorescent labels, light harvesting antennas and organic spintronics. As mentioned in section 1.5.1, for being used in applications involving light harvesting, TiO_2 nanostructures need to be sensitized using dyes/quantum dots to extend their light absorption towards visible and IR spectral region. Most of the utilized sensitizers do not absorb efficiently in red and near-IR region and FRET seems to be helpful in this regard. FRET efficiency is highly sensitive to the geometry of donor/acceptor placement. Generating cracks into the inner walls of TiO_2 nanotubes and embedding donor or acceptor molecules into the cracks and coating the wall surface with the other chromophore molecules seems to be a proper geometry for highly efficient FRET phenomenon since it provides required close proximity while keeping donor and acceptors strictly isolated from each other. While generating cracks into the inner walls of TiO_2 nanotubes is under investigation meanwhile possibility of FRET to occur in such geometry could be investigated using similar structures which are already present. As mentioned previously, presence of 1-2 nm voids connected to the wall surface through narrow cracks have already reported for nanoporous anodic aluminum oxide. This could provide a template for donor and acceptor molecular arrangement with a high similarity to what needed in TiO_2 nanotube arrays.

By controlling the preparation conditions, nanoporous AAO can be grown in a single or step to have pores corresponding to two different size scales, voids of size 1-2 nm embedded in the walls of the nanoporous scaffold and cylindrical nanopores with diameters of 10-200 nm. On the other hand, the widely used organic semiconductor Alq_3 exhibits unusual properties when confined in the nanovoids of AAO. The first such property is the shift in the wavelength of the

luminescence maximum of Alq_3 to 492 nm in the nanovoids. The luminescence maximum is blue-shifted by 18-20 nm from the peak of the thin film luminescence spectrum of Alq_3[160, 210]. The second unusual property is the anomalously long spin dephasing times exhibited by Alq_3 confined in the nanovoids as opposed to bulk Alq_3. The long dephasing time is attributed either to a phonon bottleneck resulting in a weakening of spin-phonon coupling within the nanovoid or to confinement-induced quenching of rotational/vibration modes, due to which the coupling of Alq_3's spin to these modes is suppressed[211, 212]. The exact mechanism underlying Alq_3 entrapment in the voids is still unknown but the correspondence of the size of Alq_3 molecules with the size of the voids and weak bonding interactions are clearly important. Once Alq_3 molecules are entrapped in the voids, even repeated and thorough rinsing does not remove them[213, 214]. Furthermore, not all molecules exhibit entrapment in the voids to the same degree. For instance, when we attempted to infiltrate metallophthalocyanine molecules into the voids using an identical procedure, all optical signals corresponding to residual molecules in the voids were removed after a thorough rinse. In this work, we first introduced Alq_3 molecules into the nanovoids and subsequently formed a self-assembled monolayer of a chromophore with suitable optical properties, on the remaining free surface of the nanoporous AAO architecture as shown in Figure 5.1a-d.

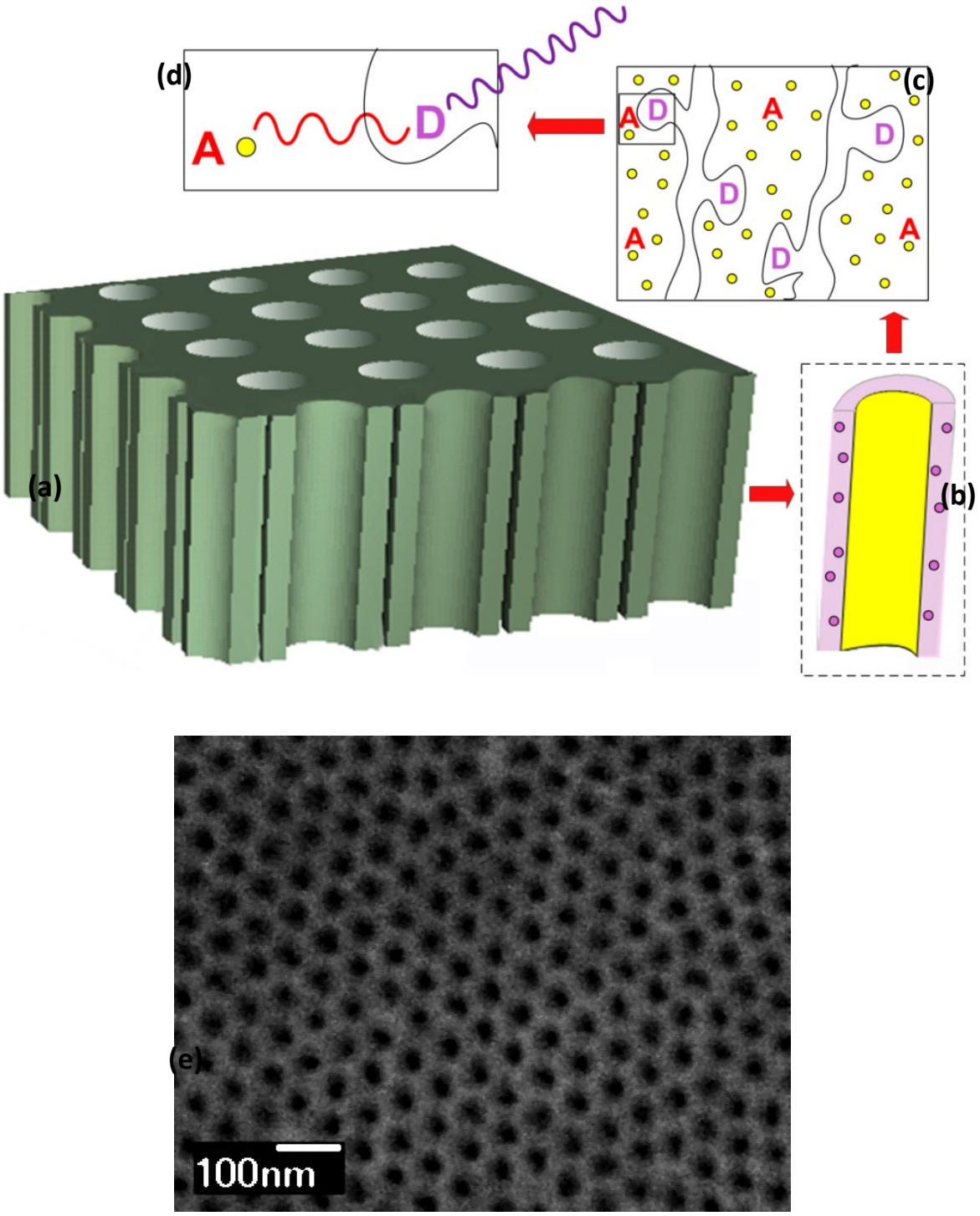

Figure 5.1 Schematic of the (a) porous alumina structure (b) cross-section of a single cylindrical pore showing self-assembled monolayer of a chromophore (yellow) on the surface and Alq_3 molecules in the nanovoids (c) donors in the voids/acceptors on the walls (d) FRET phenomenon[215] and (e) field emission scanning electron microscope (FESEM) top-view of AAO used in this work.

5.2. Experimental details

5.2.1. Sample preparation

Porous anodic aluminum oxide (AAO) has been frequently used as a template for the growth of variety of nanostructures including, but not limited to, nanowires of Ni[216], ZnO[217], CdS[218], CdSe[219], Fe[220], Co[221], Ag[222], Bi_2Te_3[223], Bi[224], multilayer nanowires of Co–Ni–Cu/Cu[225] and nanotubes of C[226], TiO_2[227], Co, Ni and Cu[228]. The length and diameter of the alumina pores can be controlled by anodization parameters such as applied voltage, anodization time and electrolyte composition[229]. There have been reports on the fabrication of porous alumina through anodization of Al foil[230] and Al thin films deposited on variety of substrates[226, 231, 232]. Electrolytes used for anodic fabrication of porous alumina are usually composed of oxalic acid[233], phosphoric acid[234], sulfuric acid, malonic acid[235] and their combinations[236]. Electric field-assisted processes of barrier layer formation and nanochannel dissolution contribute to the formation of AAO in which there is an equilibrium between oxide formation at the metal/oxide interface and oxide dissolution in the oxide/electrolyte interface[237] resulting in a constant barrier-layer thickness. Two-step anodization results in highly ordered porous structures[238]. In order to produce the nanoporous alumina template, 2 cm × 2 cm coupons of annealed high purity unpolished aluminum (99.997% Alfa Aesar) with a thickness of 250 μm were used. A highly regular pattern of cylindrical pores was obtained using the two-step process. The unpolished coupons were subjected to a chemical polishing step in an etchant consisting of 15 parts of 68% nitric acid and 85 parts of 85% phosphoric acid. The etching was carried out for 5 minutes at 85 ^{o}C and then the samples were neutralized in 1M sodium hydroxide for 20 minutes [239]. Subsequently, the polished samples were anodized for 1 hour in 0.3 M sulfuric acid electrolyte at 20 V DC bias at ~ 15 ^{o}C.[240] The nanopores formed in this step were randomly distributed on the

surface of the anodic alumina. This thin oxide film was dissolved away in hot (60 ^{o}C) chromic-phosphoric acid[239] leaving behind an array of textured scallops. Anodization was then performed in a second step. Highly order regular nanopores with a diameter of ~20 nm were formed over the surface after second step anodization in 0.1 M sulfuric acid (Figure 5.1e). The pore growth rate was ~12µm hr-1.[240] The morphology of the nanoporous alumina was imaged using a JEOL 6301F field emission scanning electron microscope (FESEM).

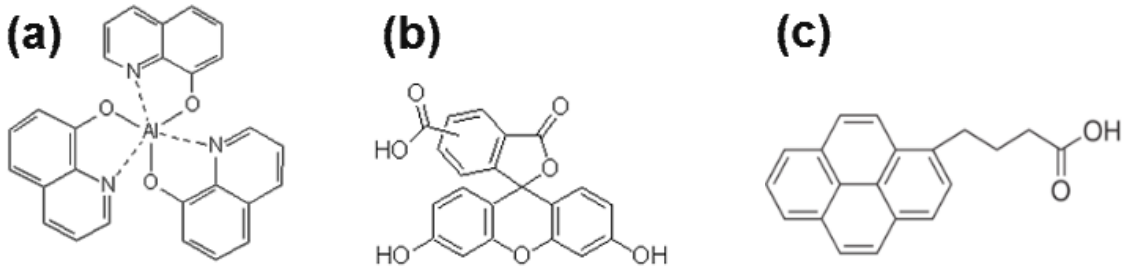

Figure 5.2 Molecular structure of the (a) Alq_3 (b) CF and (c) PBA

In addition to Alq3 (98% pure), 5(6)-carboxyfluorescein, (>95% pure, henceforth referred to as CF) and 1-pyrenebutyric acid, (97 % pure, PBA) were also used in this study. Figure 5.2 shows their molecular structures. All three chemicals were purchased from Sigma-Aldrich Corp. and used as obtained. Due to the size of the Alq_3 molecule (around 0.8 nm)[160] being smaller than that of the voids (1-2 nm), it is known that individual molecules of Alq_3 are able to penetrate into the voids and be encapsulated in them.[160] To perform the filling of the voids with the fluorescent Alq_3 molecules, a dilute (1mM) solution of the dye was prepared in chloroform and the porous alumina was left immersed in this solution for 21 hours. The long time is necessary for the Alq_3 molecules to diffuse and percolate through the cracks into the nanovoids. To completely remove the dye from the cylindrical pores and the sample surface, the sample was thoroughly rinsed with chloroform. On the other hand, to investigate the presence of the Alq_3 in the voids and its

difference from a film of Alq_3, another identical sample was dipped and dried for several times in a 10 mM solution of Alq_3 in the same solvent. In this case, an Alq_3 film was conformally coated on the surface of nanoporous AAO and Alq_3 penetration into the voids was expected to be minimal due to the higher concentration of the solution and the shorter film preparation time. Self-assembled monolayers of PBA and CF were formed by immersion for 30 minutes in 10 mM solutions in dimethylformamide (DMF) of the respective dyes subsequent to the filling of the nanovoids by Alq_3. The short immersion time and the high viscosity of the solvent (DMF) are chosen to cause as little disruption as possible to the Alq_3 molecules present in the nanovoids.

5.2.2. Spectroscopy

Optical absorption measurements were performed using a Perkin Elmer Lambda-900 spectrophotometer. Steady-state PL spectra were collected using a Photon Technology International MP-1 fluorimeter. Time resolved fluorescence measurements were performed using second harmonics of a femtosecond Ti:sapphire laser (Spectra Physics, Hurricane + May Tai system) for sample excitation. The laser pulses had 130 fs duration and energy of about 10 μJ with a repetition rate 1 kHz. The energy density on the surface of the samples was around 10 $\mu J/cm^2$. We did not observe the photobleaching-induced degradation of the photoluminescence signal during measurements. A fast vacuum photodiode (Hamamatsu, R1193U) with 250/100 ps rise/fall time and a fast oscilloscope (Textronics 7104) were used for the photoluminescence signal detection. The combined bandwidth of the detection system was 800 MHz. The time constants of the photoluminescence decay were obtained by deconvolving a recorded oscilloscope signal with the apparatus response function. Single photon fluorescence imaging of was performed using a Zeiss LSM 710 laser scanning confocal microscope. Two-photon

fluorescence imaging and fluorescence lifetime imaging (FLIM) was performed using a Zeiss LSM 510 NLO multi-photon microscope equipped with a FLIM module consisting of a Hamamatsu RS-39 Multi-channel plate detector, a filter wheel and a Becker Hickl SPC730 photon-counting board. Because of the random distribution of nanovoids from sample to sample, we verified our studies of energy transfer involving Alq_3 in the nanovoids by performing photoluminescence measurements on the same sample(s) before and after self-assembled monolayer (SAM) formation.

5.3. Results and discussion

5.3.1. Optical properties of the chromophores

Table 1 displays the absorption and photoluminescence (PL) maxima for the three chromophores in their solution phase at concentrations of ~0.001-0.01 M. The chromophores were chosen in such a way as to act as good FRET donors or acceptors to Alq_3. The emission of PBA in solution overlaps very well with the absorption of Alq_3, which when coupled with the high emission quantum yield of PBA, would suggest efficient energy transfer from PBA to Alq_3. Similarly, the emission of Alq_3 in the nanovoids overlaps with the absorption of CF suggesting that CF could function as a good FRET acceptor to Alq_3.

Chromophore	Absorption peak (nm)	Luminescence peak (nm)
Tris-(8-hydroxyquinoline)-aluminium(III)	368 (CHCl3)	512 (CHCl3)
5(6)-carboxyfluorescein	492 (Tris buffer, pH 8.0)	517 (Tris buffer, pH 8.0)
1-pyrenebutyric acid[241]	313, 325 and 346 (toluene)	377, 387 and 396 (toluene)

Table 5.1 Optical absorption and photoluminescence peaks of Alq3, CF and PBA in solution

5.3.2. Blue-shifted luminescence of Alq3 confined in the nanovoids of nanoporous AAO

The photoluminescence spectra of the two samples in Figure 5.3 clearly shows a 18 nm blue-shift from 510 nm to 492 nm for Alq_3 in the voids compared to the Alq_3 thin film on the surface of the alumina, which is known to be a signature of Alq_3 entrapment in the voids[213, 214]. Alq_3 molecules can exist in two geometric isomeric forms, namely facial (fac) and meridionial (mer) that differ in the relative position of oxygen and nitrogen atoms coordinated octahedrally to the aluminum atom. The green emitting mer form is the more commonly observed isomer in both thin films and solutions of Alq_3 while the blue emitting fac form is rarer. In some reports, the blueshift is attributed solely to the confined environment of the nanovoids, which suppresses aggregation and intermolecular interactions, further screened by the high dielectric constant of the Al_2O_3 host.[242] However, it is known that when Alq_3 molecules are confined in rigid solid state matrices such as SiO_2, a similar blueshift is obtained. For Alq_3 molecules doped into SiO_2 films by co-evaporation at concentrations of 1% or lower, Levichkova et al[243] found that ensembles of single molecules were predominantly obtained and claimed the presence of fac-Alq_3 on the basis of the observed blue-shift, the higher probability of formation of the facial form in a rigid matrix and matrix evaporation rate effects. Also, Muccini et al[244] used the differing NMR spectra of the fac and mer isomers to demonstrate the existence of pure fac-Alq_3 in a $CdCl_3$ solution at -50 °C whose fluorescence maximum was blue-shifted from that of mer-Alq_3 by 0.23 eV. At temperatures higher than -20 °C, the fac-isomer converted completely into the more thermodynamically favorable mer-form. It was further claimed that the blue emission was a molecular property and that the spectral fluorescence emission provided a distinctive fingerprint for each species. A different interpretation was provided by Baldachhini et al,[242] who explained the varying blue-shifts of Alq_3 trapped in various silica and zirconia matrices as occurring purely

due to mer-Alq_3 whose molecular orbitals were perturbed differently during interactions with different trapping matrices. The refractive index of alumina is 1.77, higher than air, SiO_2 and most organic solvents. Ignoring the polarity of the dye and the matrix, the higher index of alumina would suggest a redshift of the spectra instead of the observed blue-shift. Polar and non-polar dyes have been reported to show 5-10 nm redshifts upon confinement in an alumina matrix. In this context, the absence of a strong spectral feature at 429 nm in the excitation spectrum (Figure 5.4a) of void-confined Alq_3 corresponding to the theoretically predicted absorption peak of the facial isomer argues goes against the presence of fac-Alq_3.

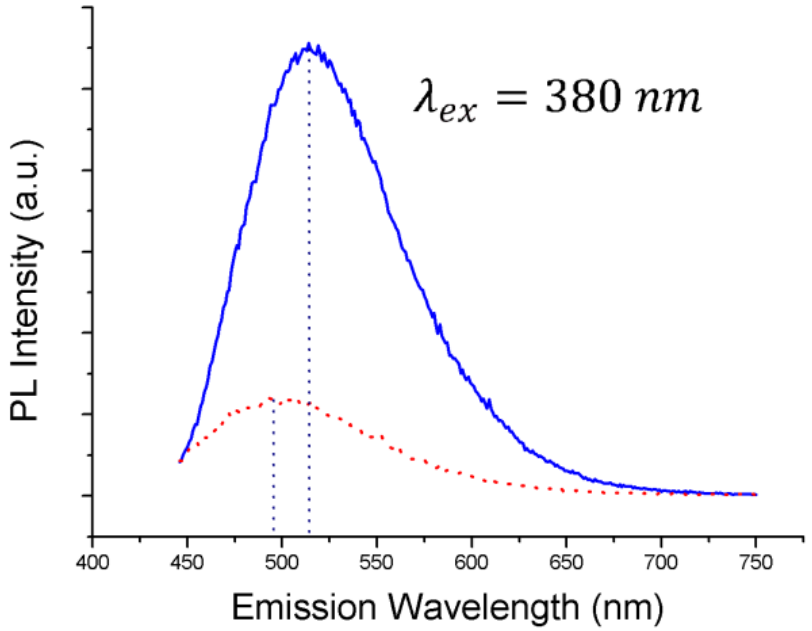

Figure 5.3 Emission scan spectra of a nanoporous alumina sample with Alq_3 on the surface (blue solid-curve) and in the voids (red dot-curve). Note the prominent blueshift of the Alq_3 emission maximum to shorter wavelengths when confined in the nanovoids.

5.3.3. Steady state studies of the Alq_3-CF system

The excitation spectra of the Alq_3-CF donor-acceptor system in nanoporous AAO are shown in Figure 5.4. In Figure 5.4a, wherein the emission is monitored at 515 nm, a wavelength at which

both Alq_3 and CF emit, the excitation spectrum of Alq_3 in the nanovoids (black curve) shows a characteristic broad absorption band centered around ~368 nm, corresponding to the optical absorption of Alq_3. The same absorption band is also seen in the excitation spectrum for the sample containing Alq_3 in the nanovoids and CF SAM on the surface (red curve). In addition, a new broad band from ~440-500 nm is observed, which corresponds to the optical absorption of the carboxyfluorescein. In Figure 5.4b, wherein the emission is monitored at 480 nm, only the sample containing Alq_3 alone displays the characteristic absorption feature of Alq_3, which is conspicuously absent in the sample containing both Alq_3 and CF. Such behavior is consistent with Förster-type energy transfer from the Alq_3 in the nanovoids to the CF SAM.

When energy transferred has occurred, the photons are finally emitted from CF, which however does not luminesce at 480 nm, due to which no feature is observed. On the other hand, when Alq_3 alone is present, the final emission of the photons occurs from the Alq_3 molecules in the nanovoids, which have an appreciable luminescence at 480 nm due to the confinement-induced blue-shift. The optical properties of the CF SAM in Figure 5.4c indicate twin absorption peaks at 459 and 483 nm, and an emission peak at 530 nm. The plot shows that a large spectral overlap between the emission of void-confined Alq_3 and the absorption of CF, a necessary condition for energy transfer from Alq_3 to CF, is present. Using the optical properties of Alq_3 and CF in dilute solutions, a Förster radius of 3.3 nm was calculated. The blue-shifted emission of Alq_3 confined in the nanovoids improves the spectral overlap with the absorption of CF and a Förster radius of 3.9 nm was calculated for this case.

Energy transfer from Alq_3 to CF is further confirmed by the data in Figure 5.4d, which shows a complete suppression of the Alq_3 emission with a peak at 492 nm, replaced only by the emission of the CF peaking at 530 nm. Figure 5.4e provides further confirmation that thin film

Alq_3 has significantly different optical properties from Alq_3 in the nanovoids and shows why the observed behavior does not result from intra-film energy transfer between Alq_3 and CF molecules at the surface of the walls. It clearly makes clear that in the Alq_3-CF donor-acceptor system, the emission at 516 nm originates only from Alq_3 in the nanovoids and from the CF self-assembled monolayer and not from thin film Alq_3, thus indicating that Alq_3 is found only in the nanovoids having been completely removed from the surface by the rinsing process. Also, unlike CF molecules anchored to the surface by carboxylate bonds, Alq_3 molecules are not bound and are easily removed by rinsing steps. The void distribution, which results from volumetric stresses during the anodization process, is random due to which no two samples even with identical preparation conditions, have exactly the same number density of voids per unit area. However on average, we observed as in Figure 5.4f, that the steady state emission intensity of the CF SAM normalized to sample area, was higher in the presence of Alq_3 in the nanovoids rather than in its absence, which we attribute to energy transfer from the Alq_3 increasing the emission of the CF SAM.

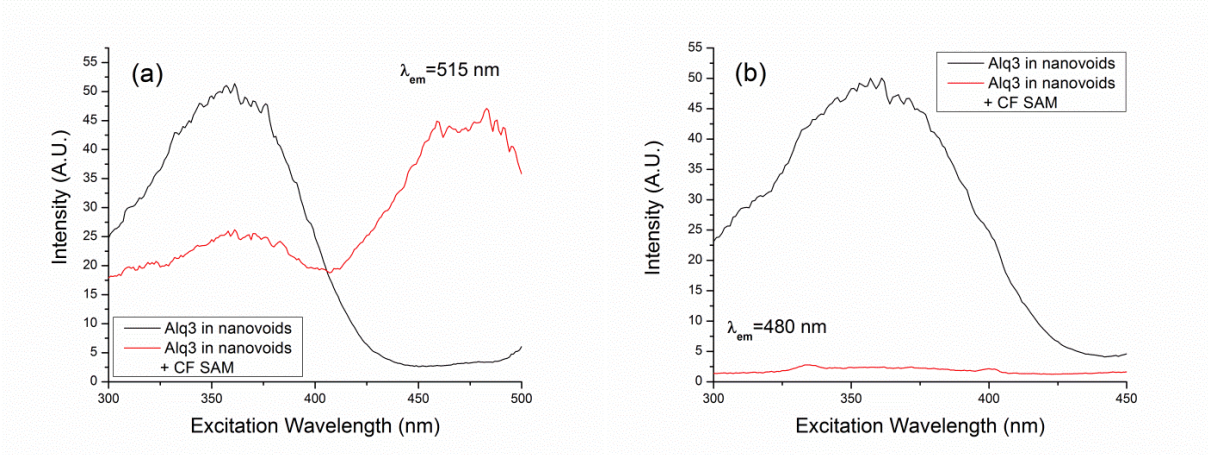

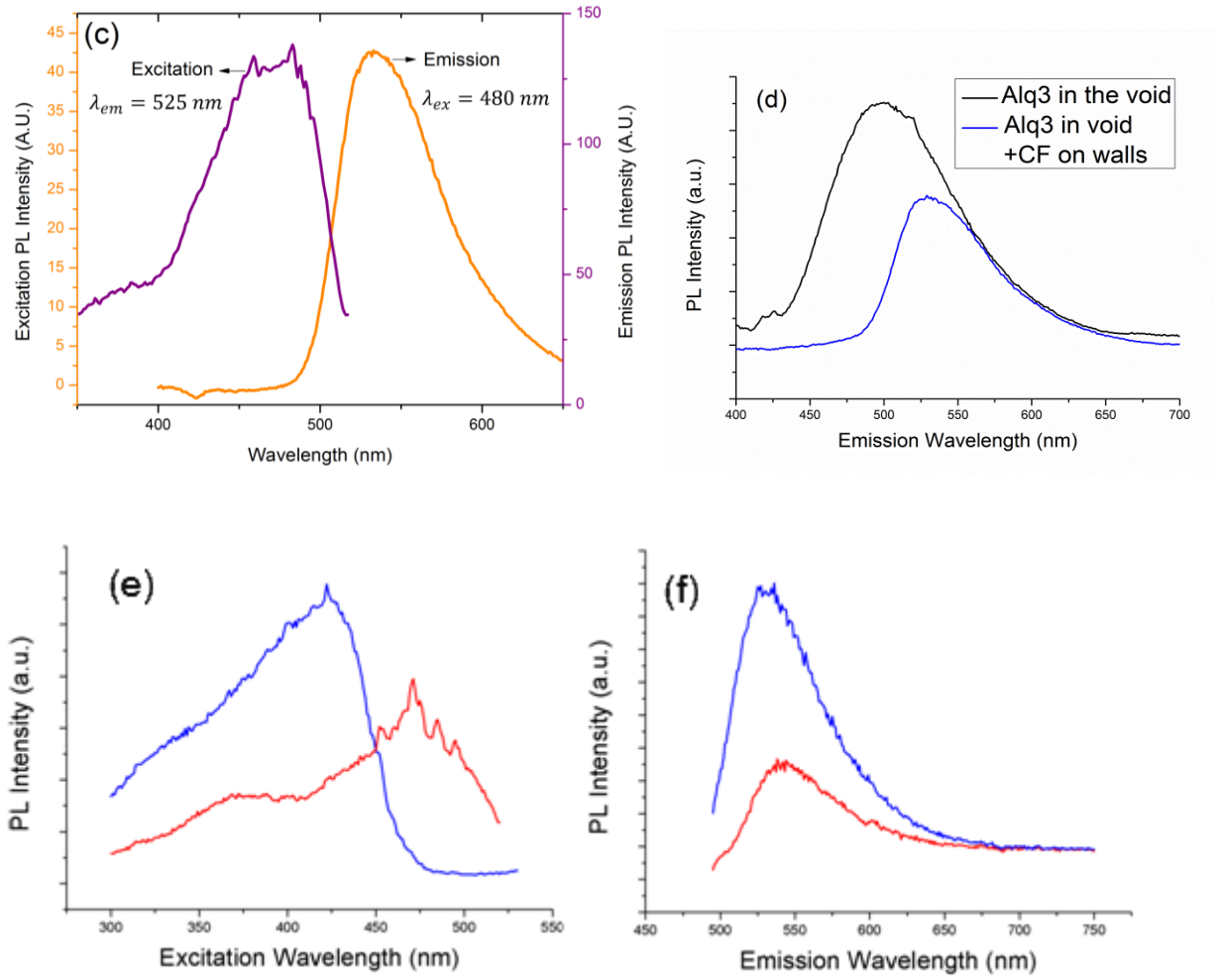

Figure 5.4 (a) and (b) Excitation scans of the nanoporous AAO samples with only Alq_3 in the nanovoids (black) and containing Alq_3 in the nanovoids along with a self-assembled monolayer of at CF (red) monitored at emission wavelengths of 515 nm and 480 nm respectively, (c) Excitation and emission spectra of CF SAM alone adsorbed onto nanoporous alumina, (d) Emission scans of nanoporous AAO samples with only Alq_3 in the nanovoids (black) and containing Alq_3 in the nanovoids along with a self-assembled monolayer of CF (blue) excited at 380 nm (e) Photoluminescence excitation spectra of the (blue) thin film of Alq_3 on nanoporous alumina formed by dip and dry method and (red) Alq_3 in the voids and CF on the walls ; the emission was monitored at 516 nm (f) Photoluminescence emission spectra (λexc=380 nm) of (red curve) a CF coated nanoporous alumina sample without Alq_3 in the voids and (blue curve) an identically prepared nanoporous alumina sample with CF SAM but with Alq_3 previously infiltrated into the nanovoids.

5.3.4. Steady state studies of the PBA-Alq3 system

The second FRET system studied by us, based on a supramolecular organization of dyes in a hierarchical nanoporous AAO architecture, consisted of a self-assembled monolayer of 1-pyyrenebutyric acid as donor and nanovoid-confined Alq_3 as acceptor. As indicated in table 1, monomeric 1-pyrenebutyric acid has emission maxima at ultraviolet wavelengths. However, when PBA molecules are present at high concentration, they form an excimer with a broad emission peaking at 470 nm. In addition to monomeric and excimeric emission, in rigid environments, PBA can also exhibit emission due to a bimolecular ground-state association (dimer) with a peak at ~450 nm, which is distinguishable from the excimeric form by its different fluorescence decay and depolarization dynamics.[245] The broad blue emission exhibited by PBA monolayers[246] with a peak wavelength of ~450 nm is attributed by some reports[247, 248] to the dimeric form. We observe this behavior in the PBA SAM on nanoporous alumina when no other chromophores are present, as shown in Figure 5.5. Also shown is the emission of Alq_3 in the nanovoids when no other chromophores are present, displaying the characteristic blue-shifted mission peak at 492 nm. When Alq_3 is present in the nanovoids together with a monolayer of PBA on the surface, we observe the disappearance of the PBA emission peak and an increase in the intensity of the Alq_3 peak, a signature of Förster-type resonance energy transfer from the PBA to the Alq_3. Due to the much higher number density of PBA molecules in the architecture compared to Alq_3 molecules in the nanovoids, energy is funneled from multiple PBA molecules into isolated Alq_3 molecules, resulting in a large increase in the Alq_3 emission. Monomeric PBA and Alq_3 have a very good spectral overlap while the spectral overlap integral of the PBA excimer and blue-shifted Alq_3 is poor (Förster radius = 1.8 nm) due to the shift in emission of the PBA in monolayer form. Yet, as Figure 5.5 shows, FRET from the PBA to Alq_3 is highly

efficient, which strongly suggests that energy transfer to Alq_3 occurs faster than excimer formation in PBA.

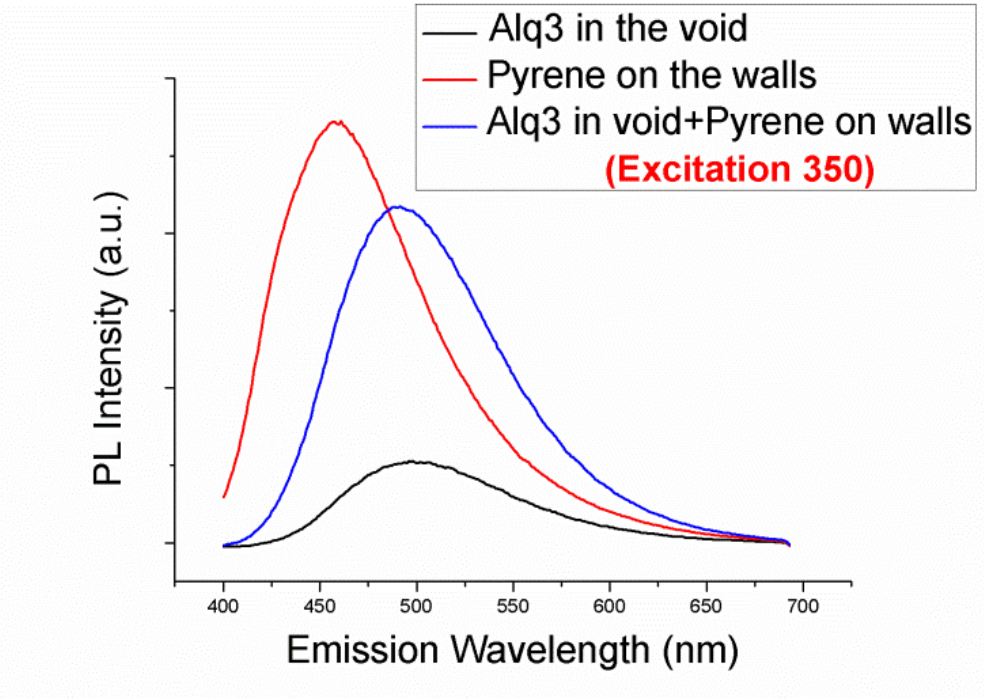

Figure 5.5 Emission scan spectra of a nanoporous alumina sample with only Alq_3 in the nanovoids (black curve), with only a PBA SAM (red curve), and with both Alq_3 in the nanovoids and a PBA SAM. The excitation wavelength used was 350 nm.

5.3.5. Time-resolved photoluminescence studies

We report on the first time-resolved fluorescence studies of Alq_3 in the nanovoids of AAO, which are shown in Figure 5.6 and Figure 5.7. The time evolution of the Alq_3 emission was fit to a single exponential with a lifetime of 1.7 ns (χ^2=1.9). But a superior fit (χ^2=1.0) was obtained to a biexponential fit consisting of a fast component of 338 ps and 2255 ps. This is significantly different from the reported lifetimes of Alq_3 thin films (~6-19 ns depending on purity) as well as dilute solutions of Alq_3 (~12-17 ns).[249]

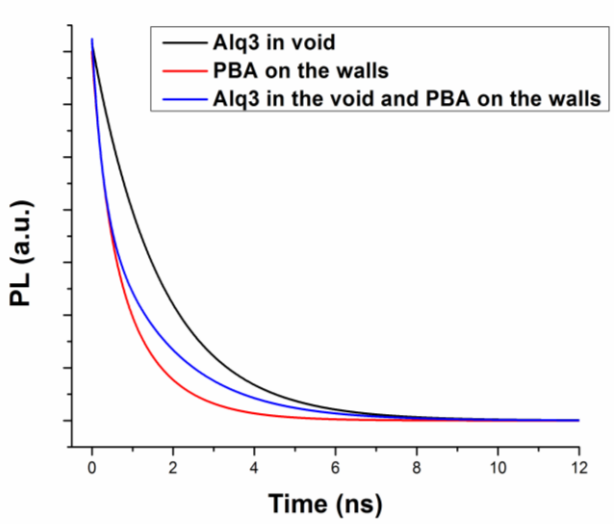

Figure 5.6. Time-resolved photoluminescence of a hierarchical nanoporous alumina sample containing void-confined Alq_3 acceptors and surface anchored PBA donors. The excitation wavelength used was 400 nm.

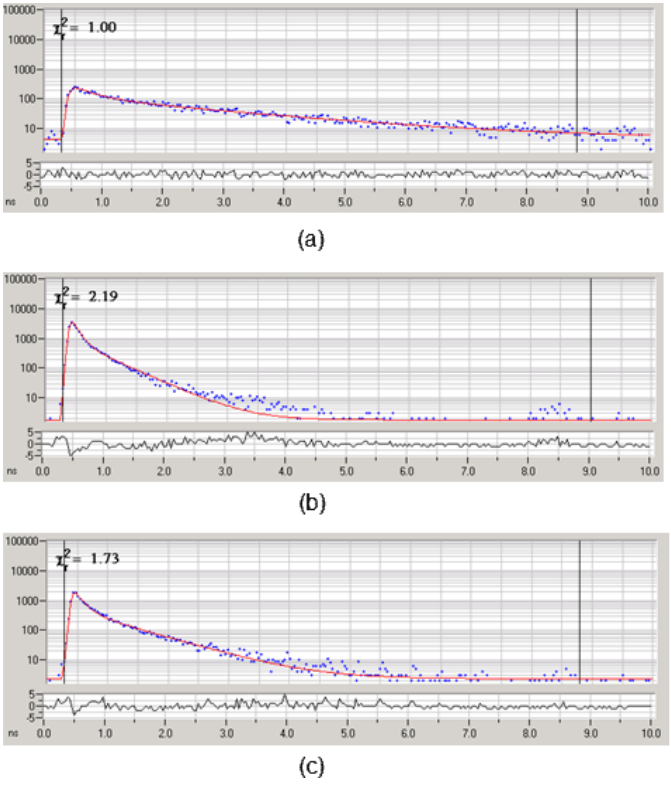

Figure 5.7 Time-resolved photoluminescence of hierarchical nanoporous alumina samples containing a) void-confined Alq_3 alone b) surface anchored CF SAM alone and c) void-confined Alq_3 donors together with surface anchored CF SAM donors. The decays were obtained using FLIM in a two-photon confocal fluorescence microscope. The excitation wavelength used was 800 nm.

The results from time-resolved fluorescence are summarized in Table 2. Steady state emission spectra in section 3.4 indicated near-complete extinction of the PBA fluorescence due to energy transfer to the Alq_3 molecules confined in the nanovoids despite a spectral overlap integral of only 1.85×10^{-15} cm^3 M^{-1}. Furthermore, Figure 5.5 clearly shows that the previously weak emission of void-confined Alq_3 is greatly enhanced in the presence of PBA donors due to FRET-mediated optical pumping. The fluorescence lifetime data indicates that the underlying processes are more complex. The fluorescence of the self-assembled monolayer of PBA on nanoporous alumina exhibits a bi-exponential decay with a two relatively fast components (244 ps and 493 ps). Thus, nanovoid-confined Alq_3 and PBA both possess faster components with lifetimes in roughly the 300 ps range but they differ more substantially in the lifetime of their slower components. In the presence of nanovoid-confined Alq_3, the fluorescence of the Alq_3-PBA system is still bi-exponential with a similar highly weighted fast component of lifetime 192 ps but the second component is slower with a lifetime of 1827 ps and a spectral weight of 5.5 %. The appearance of the longer-lived component with a lifetime of 1827 ns is definitive evidence of energy transfer from the PBA to Alq_3 and enables us to estimate the rate of energy transfer rate from PBA to Alq_3 to be in the range 2-5 $\times 10^9$ s^{-1}. This is also observable in Figure 5.6 where the fluorescence decay curve of the combined Alq_3-PBA system initially closely follows the decay of PBA but converges to the decay of Alq_3 for longer times.

	Lifetimes (ps) and component weights		
Configuration of dyes	$\tau 1$	$\tau 2$	$\chi 2$
Alq_3 in voids	338 (62.8 %)	2255 (37.2 %)	1.90
CF on surface	100 (85.5 %)	474 (14.5 %)	2.19
Alq_3 in voids and CF on surface	130 (82.9 %)	734 (17.1 %)	1.73
PBA on surface	244 (62.9 %)	493 (37.1 %)	1.00
Alq_3 in voids and PBA on surface	192 (94.5 %)	1827 (5.5 %)	1.00

Table 5.2. Summary of FLIM studies of donor-acceptor systems involving nanovoid-confined Alq_3 as either donor or acceptor. The second dye in the FRET pair was anchored to the free-surface of the nanoporous alumina as a self-assembled monolayer.

For the case of the Alq_3-CF system (Figure 5.7), a bi-exponential decay similar to that of the CF self-assembled monolayer in isolation is observed. The optical pumping of the CF emission due to energy transfer increases the lifetimes of both components of the CF emission and is fully consistent with the steady state PL studies in section 3.3 which indicated highly efficient FRET between void-confined Alq_3 donors and CF-acceptors in the hierarchical nanostructure through the complete suppression of donor fluorescence. Based on these results, we estimate the energy transfer rate from Alq_3 to CF to be $\sim 10^{10}$ s^{-1}. The higher rates occur due to the relatively large spectral overlap integral (1.82×10^{-13} cm^3 M^{-1}) between the emission of nanovoid-confined Alq_3 and the absorption of the CF monolayer.

In summary, a hierarchical porous anodic alumina consisting of a highly ordered array of ~20 nm nanopores and 1-2 nm-sized voids in the pore-walls has been used to construct a

supramolecular dye assembly with Alq_3 molecules embedded in the nanovoids, and a self-assembled monolayer of carboxyfluorescein or pyrenebutyric acid on the surface. The deterministic placement of distinct chromophores at defined locations in a nanostructured matrix is not-trivial since the potential for placement defects is enormous. However, we have found that ensemble-averaged steady-state and time-resolved luminescence data are consistent with Alq_3 molecules being confined primarily in the voids and other chromophores (CF, PBA) being located only on the surface of the walls. Confinement in the nanovoids not only prevents the aggregation of the Alq_3 molecules but also provides an environment suitable for highly efficient FRET if a layer of acceptor molecules is present on the surface of the pore walls. We present the first time-resolved fluorescence measurements of Alq_3 confined in the voids which showed an excited state lifetime of 1.7 ns. In the case of the CF-Alq_3 pair, the carboxyfluorescein self-assembled monolayer acted as a very efficient acceptor to Alq_3 donors in the nanovoids. In the case of the PBA-Alq_3 pair, energy transfer occurred from 1-pyrenebutyric acid self-assembled monolayer donors to the void-confined Alq_3 acceptors faster than the competing PBA excimer/dimer formation. The high efficiency of the FRET process in the hierarchical AAO architecture is promising for applications in biological labeling and spectroscopic rulers, organic electroluminescence and spin-Förster transfer.

5.3.6. FRET using mixed monolayers in TiO_2 nanotube arrays

While alumina is amorphous and non-conducting, other valve metal oxides which lend themselves to anodic nanostructuring, such as TiO_2, Ta_2O_5 and Fe_2O_3 have semiconducting and/or photocatalytic properties. In light of our results, extension of the dual pore size scale concept to such systems would be particularly attractive in enhancing the performance of solar cells and photocatalysts by the use of light harvesting antennnas. In order to apply FRET

phenomenon using crack and wall geometry (tested for insulating AAO) into semiconductors such as TiO_2 nanostructures, one needs to not only generate similar crack structures in them but also has to take into account their absorption as an additional interfering factor. Producing similar cracks on the walls of TiO_2 nanotubes is still under investigation. Meanwhile we thought it would be interesting to investigate the FRET using TiO_2 nanotubes while the chromophores co-exist on the walls of nanotubes and their excitation wavelengths overlap with the absorption spectrum of TiO_2 nanotube arrays. Such co-esistence of two different chromophores was engineered by forming self-assembled mixed monolayers of two different luminescent dyes. TiO_2 nanotubes were anodically grown on Ti foil in an EG based electrolyte containing 0.3 w% NH_4F and 2 v% DI water at 40V for 2 hours. Top debris layer was removed using RIE by SF_6 gas followed by annealing for 2 hours in air and 1 hour in oxygen flow with ramp up rate of 5 ^oC/min. After annealing was finished, furnace was turned off and samples cooled down overnight. Ti foil with TiO_2 nanotube layer on it was then cut into small pieces in order to fabricate different samples on identical TiO_2 nanotube arrays. 1 and 6.1 mg/mL solutions of poly[3-(3-carboxypropyl)thiophene-2,5-diyl] (P3HT-COOH) and CF were prepared in DMF. The reason we did not use Alq_3 in this experiment was that it lacks appropriate anchoring groups to be attached to the walls of TiO_2 nanotubes whereas carboxylic acid group present in both CF and P3HT-COOH makes them anchor well. P3HT has the additional advantage that it has been already utilized in TiO_2 nanotube-based solar cells[250-252] and studying FRET using it may result in further improvement in the efficiency of such devices. Individual annealed TiO_2 nanotube samples were immersed into each of the solutions for 17 hours to form the first layer of the corresponding dye. For second and third layer coatings, immersion time was 100 minutes. Figure 5.8a-c depict the emission scan spectra of blank and different types of dye-coated TiO_2 nanotube

arrays with the excitation wavelengths of 380, 400 and 440 nm respectively. Figure 5.8a shows that broad absorption from 550 nm to 650 nm can be attributed to P3HT-COOH since it does not exist in blank and CF coated annealed TiO_2 nanotube spectra. It can also be seen that strong defect emission of blank TiO_2 nanotube sample at wavelengths higher than 650 nm significantly decreases in chromophore coated samples, which is because TiO_2 absorbs photons of the 380 nm excitation wavelength and organic dyes (CF and P3HT-COOH) compete with it in absorbing photons hence reducing its emission. Figure 5.8b and c in which there is noticeable emission at higher wavelengths is absent, further prove that strong emission at wavelengths higher than 650 nm is due to TiO_2 since as can be seen in Figure 5.8d, both 400 nm and 440 nm excitation wavelengths are strongly absorbed by dyes compared to the blank TiO_2 nanotube sample. In Figure 5.8c, the strong green luminescence of the CF coated TiO_2 nanotubes is in stark contrast to the remaining spectra, and is attributable to both poor charge injection into the TiO_2 conduction band from the lowest unoccupied molecular orbital of CFand the high PL quantum yield of CF. When P3HT-COOH coexists with CF on the nanotube walls, the aforementioned green luminescence is completely quenched which is strongly suggestive of intra-monolayer FRET from CF to P3HT. This is not the only additional parameter since upon light absorption, since a noticeable imbalance in the absorption coefficients of two chromophore components (much higher for P3HT-COOH than CF)[253-255] makes P3HT-COOH preferentially absorb most of the photons when both chromophores are present. On the other hand, there is also imbalance in the luminescence quantum yields of P3HT-COOH and CF (much lower for P3HT and its compounds[256, 257]). This makes P3HT-COOH to act as a PL quencher if one supposes that FRET occurs from CF to P3HT-COOH. There is also a huge overlap between the absorption spectra of CF and P3HT-COOH[254, 258] which makes the FRET interpretation more challenging.

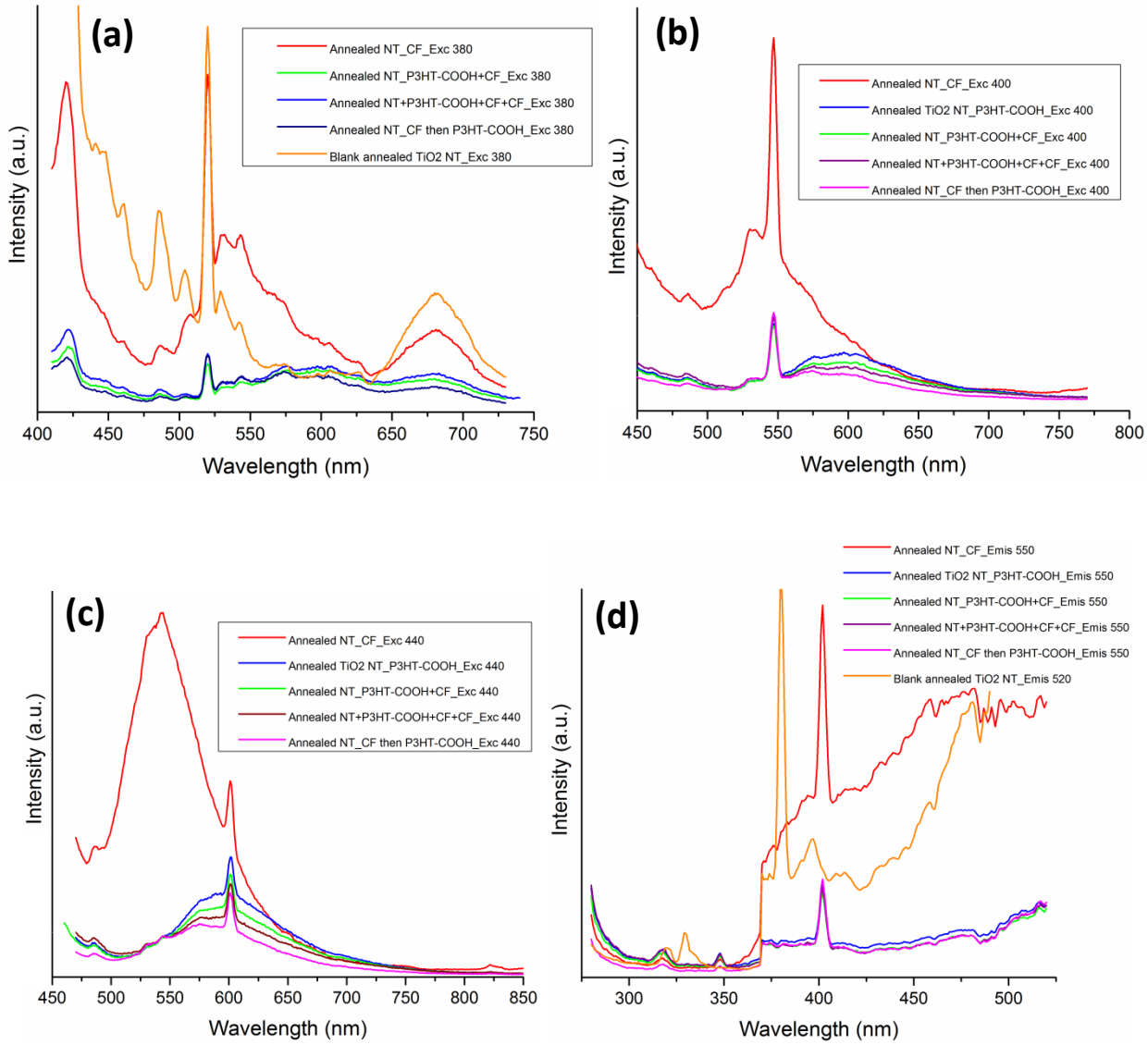

Figure 5.8 Emission scan spectra with the exciting wavelengths of (a) 380 nm, (b) 400 nm and (c) 440 nm. Excitation scan spectra with emission wavelengths of 550 and 520 nm for dye-coated and blank TiO_2 nanotube arrays respectively.

Initial experimental results presented here reveal the fact that studying the FRET on TiO2 nanotube arrays is more complicated than on AAO which was well studied in the previous sections. Hence, further experiments need to be designed and executed in order to address both

the proper interpretation of the observations presented above as well as the fabrication of voids in the walls of TiO2 nanotube arrays.

Chapter 6

6. Charge carrier transport in single crystal TiO_2 rutile nanowire arrays[1]

6.1. Introduction

TiO_2 nanotube and nanowire arrays constitute functional oxide nanomaterials with potential applications in photovoltaics[259, 260], photocatalysts[261, 262], field emitters[263, 264] and electrochemical battery anodes[265, 266]. Carrier transport in such nanostructures is of fundamental importance but to the best of our knowledge has never been directly measured. In this research work, we perform direct measurements of the majority carrier mobility of rutile nanowires obtained using transient and steady-state space charge limited currents (SCLC), and free carrier and trap densities obtained by SCLC.

6.2. Experimental

6.2.1. Nanowire synthesis and characterization

FTO-coated glass (TEC-15, 15 Ω/square) substrates were first cleaned with Triton-X detergent followed by thorough rinsing in water, then cleaned in acetone, methanol in an ultrasonic bath and subsequently dried in a nitrogen jet. The substrates were loaded into a 23 ml capacity, sealed Teflon reactor in a PARR acid digestion vessel containing 5 ml of H_2O, 2.5 ml glacial acetic acid and 2.5 ml concentrated HCl. 0.2 ml titanium butoxide was then added drop-by-drop and stirred until a clear solution was obtained. The hydrothermal synthesis was performed at 180 °C for 6 hours. Morphological and structural characterization were performed

[1]Results of this research work were published as a journal paper entitled "Majority carrier transport in single crystal rutile nanowire arrays" in Phys. Status Solidi RRL 8, No. 6, 512–516 (2014).

using a Hitachi S4800 cold field emission scanning electron microscope and a Hitachi HF3300 transmission electron microscope, respectively.

6.2.2. Time-of-flight and SCLC studies

Schematic image of the TOF measurement setup is shown in Figure 6.1. Aluminum electrodes were deposited onto the nanowires through a shadow mask in an electron beam evaporation system. The samples were mounted such that deposition occurred at an oblique angle, in order to minimize the depth of penetration of the deposited metal between the nanowires.

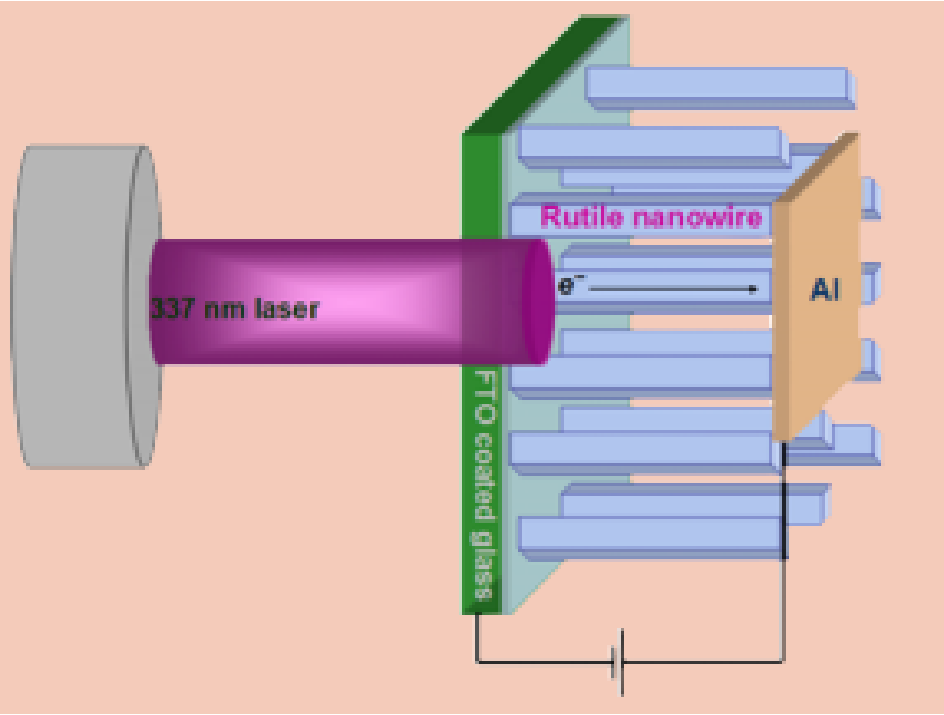

Figure 6.1 Schematic image of TOF measurement setup for TiO_2 nanowire arrays grown on FTO

Voltage bias was applied between the FTO:glass substrate and the aluminum top electrode using a DC power supply. The maximum electric field used was 2×10^4 V cm^{-1}. Charge carriers were optically injected into the sample from a nanosecond pulsed N_2 laser (VSL337ND-

S, Spectra-Physics) through the FTO:glass substrate which served as the transparent, blocking electrode. Transients were observed at room temperature and ambient air using an Agilent DSO1034B sampling oscilloscope using terminal resistances ranging from 50–1000 Ω. To enhance the measurements, signal-to-noise ratio (SNR), 256 single measurements were averaged, which increased the SNR by a factor of 16. The current–voltage characteristics and capacitance of the samples were measured using a Keithley 4200 semiconductor parameter analyzer equipped with a CVU module.

6.3. Results and discussion

As evidenced by Figure 6.2, the nanowires are ca. 1.26 μm in length, vertically oriented from the FTO:glass substrate, and 10–20 nm in width. The insets in Figure 6.2 show the square facets of the terminal (001) crystal planes and the d-spacing of 0.288 nm corresponding to the (001) crystal plane of rutile, obtained along the length of a nanowire. Figure 6.3 shows the transient photocurrent obtained when the Al top electrode is biased +2 V with respect to the FTO substrate. Under laser illumination through the FTO, most electron–hole pairs are generated within a penetration depth of the transparent contact. For 337 nm radiation, the penetration depth of rutile, given by the inverse of the absorption coefficient, is ~200 nm. Photogenerated holes are collected by the closely-lying FTO contact and electrons are injected into the bulk of the nanowires, where they drift under the influence of the applied field (2×10^4 V cm^{-1}).

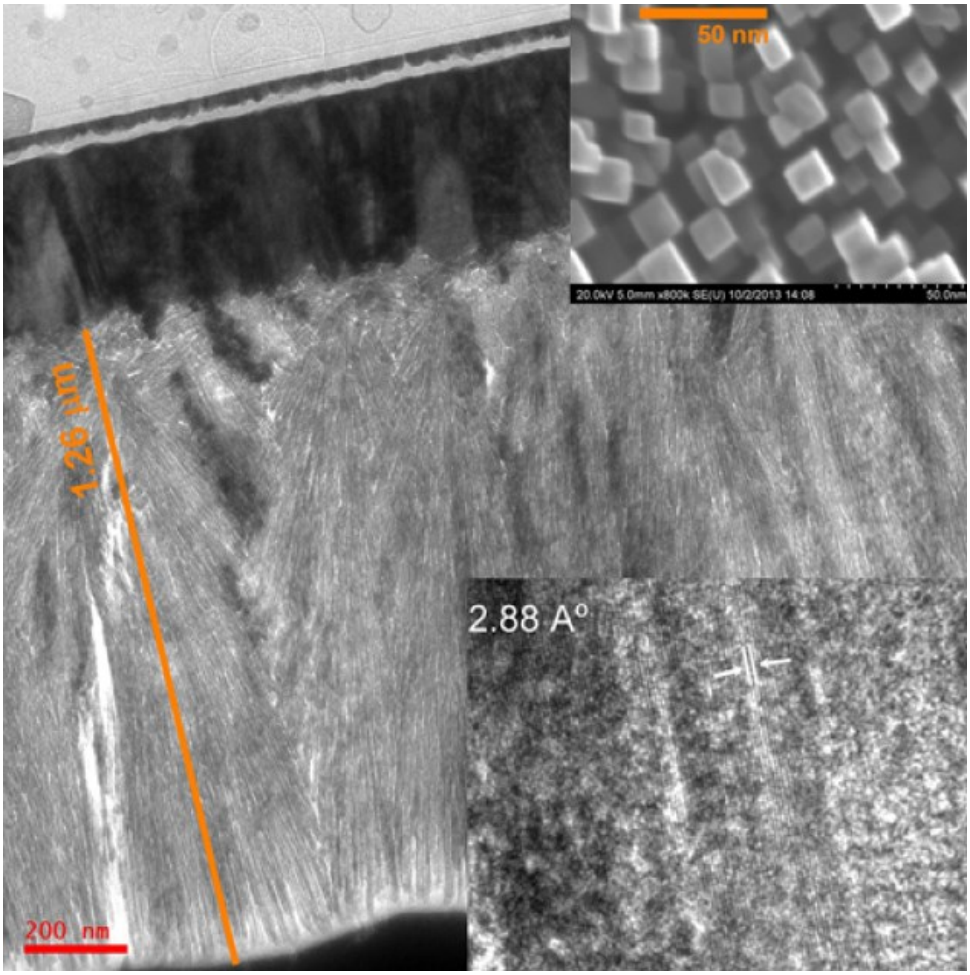

Figure 6.2 Transmission electron micrograph of the cross-section of rutile nanowire array. One inset (top-right) shows the FESEM top-view of the nanowires and another inset (bottom-right) is the selected area diffraction pattern of the lateral crystal plane of the nanowires.

By measuring the sample capacitance and by integrating the collected photocurrent, we estimated the injected charge in our experiment Q_{inj} and found it to be much larger than the charge Q_0 associated with the geometrical capacitance of the nanowires. Consequently, the excess carrier density is large enough to perturb or modify the electric field inside the nanowires and space-charge limited transport prevails during the drift of electrons through the nanowire. Under these conditions, a cusp is observed in the transient photoconductivity[267], whose temporal location is related to the electron transit time (t_{tr}) and drift mobility (μ_n) by

$$t_1 = 0.786.t_{tr} = \frac{0.786L^2}{\mu_n V} \quad (6.1)$$

where L is the effective nanowire length over which electron drift occurs and V is the applied voltage bias. Substituting in Eq. (6.1) the values of the parameters and the time at which the peak photocurrent occurred, we obtain an electron mobility of 1.4×10^{-5} $cm^2V^{-1}s^{-1}$. In the following paragraphs, we show that this value is an effective mobility corresponding to the case of fast deep trapping where the capture times are much larger than the release times[267]. The sharp peak at the very beginning of the photoconductivity transient corresponds to the electronic system response time, determined by the series resistance of the oscilloscope and cables, and sample capacitance. The transient photocurrent at the closure of the system response peak but still close to the beginning of the transient is approximately half the maximum photocurrent at the cusp. The instantaneous photocurrent density (j_0) at the beginning of the space-charge-limited TOF transient is given by[267]

$$j_0 = \frac{\varepsilon \mu_n V^2}{2L^3} \quad (6.2)$$

where ε is the permittivity of the rutile nanowires. Since the nanowires are oriented along their c-axis, a value of 170 was used for the anisotropic relative permittivity of rutile[268, 269]. Using the amplitude of the photocurrent given by Eq. (6.2), we extract a value of 1.8×10^{-5} $cm^2V^{-1}s^{-1}$ for μ_n. The maximum photocurrent (j_{max}) is expected to overshoot the steady state value by 21% such that $j_{max}/j_0 = 2.7$. However, the value of j_{max} is less than the value expected from theory due to trapping. The post-transit current in Figure 6.3 was fit to a monoexponential decay with a time constant of 1.8 ms.

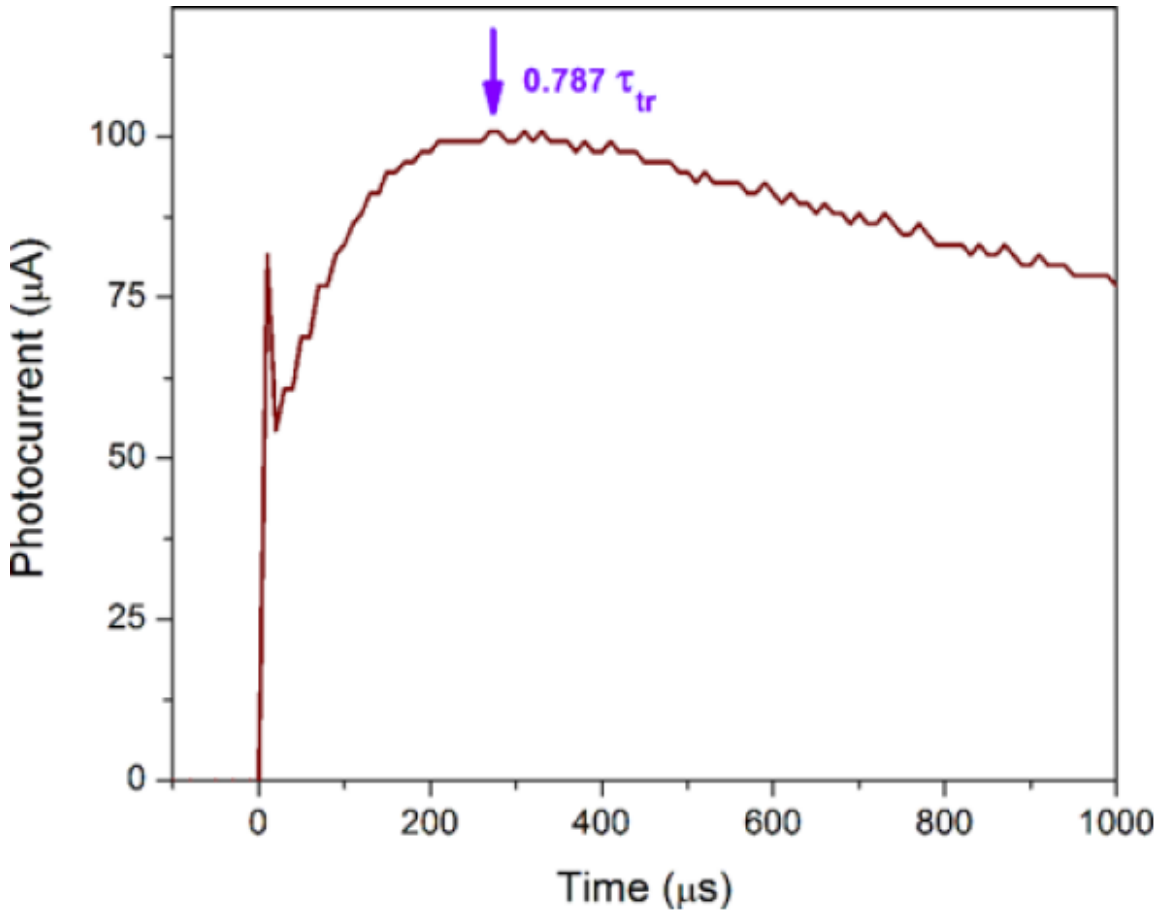

Figure 6.3 Experimental photoconductivity transient for rutile nanowire array sample with a bias of 2 V (Al – positive; FTO – negative).

The J–V characteristics of the rutile nanowires are plotted in Figure 6.4, and show distinct transport regimes. At low bias, the slope of the log–log plot is exactly 1 (Region I), corresponding to resistive transport due to the low concentration of mobile charge, the remainder being trapped. As the bias is increased, transport is eventually dominated by electrons injected from the cathode (Region II) and the slope of the plot is 2.

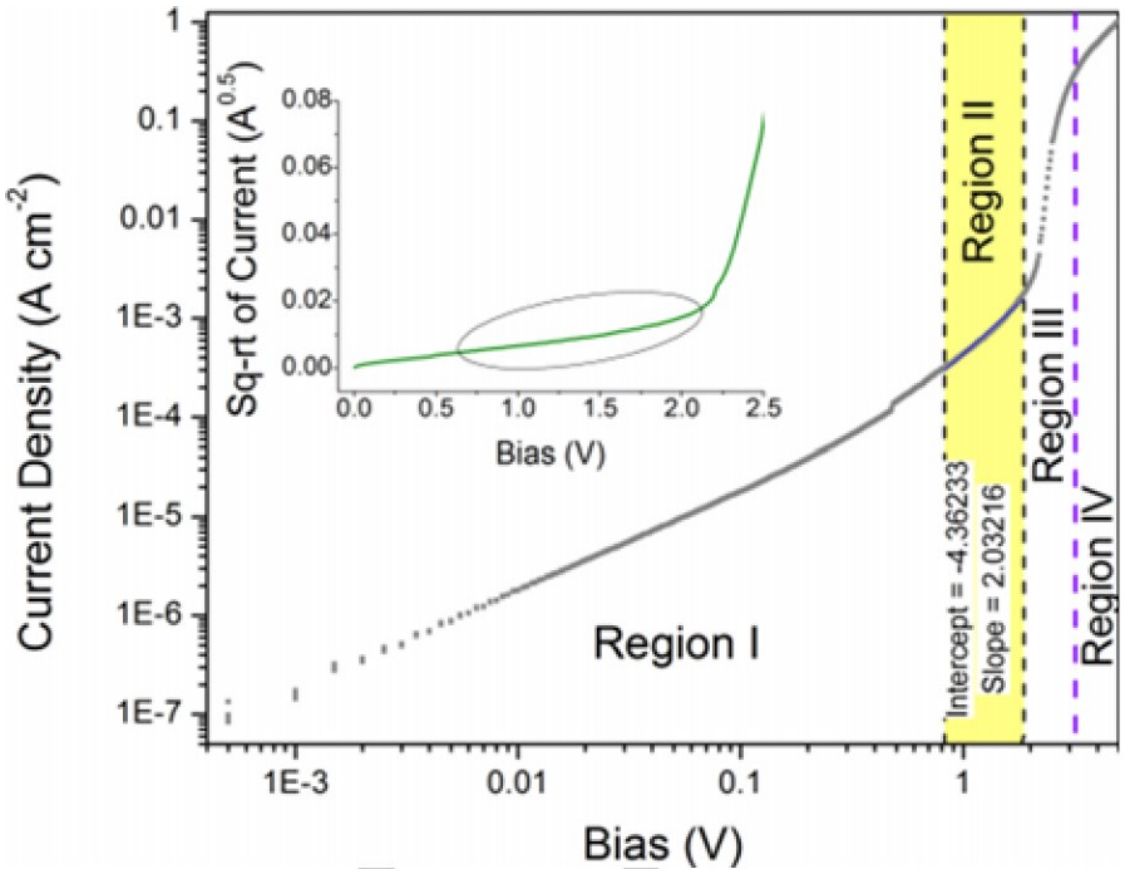

Figure 6.4 Log–log plot of the steady state current–voltage characteristics of the rutile nanowire array sample. Regions corresponding to different transport regimes are differentiated. The inset is the same J–V characteristic plotted on a linear scale with the square root of the current as the y-axis. The ellipse in the inset indicates the space charge limited transport regime where a linear fit is obtained.

As long as the quasi-Fermi level remains lower than the trap level, the ratio θ of free carriers to trapped carriers is a constant independent of bias. The resulting space-charge limited current is given by

$$j_{SCLC} = \frac{9\varepsilon\mu_{n,eff}V^2}{8L^3} \qquad (6.3)$$

where $\mu_{n,eff}$ is the effective electron mobility of a sample with trap-free mobility $\mu_{n,tf}$ in the presence of traps, given by

$$\mu_{n,eff} = \frac{\theta}{\theta+1}\mu_{n,tf} \quad (6.4)$$

Equation (6.3) applied to the SCLC regime (Region II) in Figure 6.4 gives a mobility of 2.56×10^{-5} $cm^2V^{-1}s^{-1}$. Substituting the extracted values of mobility in the linear (resistive) transport regime (Region I), an equilibrium free electron concentration of $\approx 10^{14}$ cm^{-3} is obtained for the rutile nanowires, which is in line with values inferred from other types of characterization[270, 271]. As the number of injected carriers increases in Region II, the quasi-Fermi level rises toward the conduction band until it eventually passes through the trap level filling all the traps, thus entering Region III. Above this trap-free limit (V_{TFL}), the current increases rapidly as no further trapping occurs until the injected free charge is approximately equal to the trap density N_T, at which point the current is predominantly composed of mobile charge (Region IV). The trap-free limit is given by[272]

$$V_{TFL} = \frac{eL^2N_T}{2\varepsilon} \quad (6.5)$$

From Figure 6.4 and Eq. (6.5), the density of deep traps in the rutile nanowire array sample was extracted to be 3.5×10^{16} cm^{-3}. The chemical and electronic properties of the surface exert a disproportionate influence on the electrical properties of semiconductor nanowires due to the large surface to-volume ratio in such one-dimensional nanostructures. Based on this fact, if the observed deep traps are attributed predominantly to acceptor-type surface trapping states, then the total density of traps is related to the nanowire diameter d and the surface state density (n_s) as

$$N_T = \frac{4n_s}{d} \quad (6.6)$$

Substituting the relevant parameters in Eq. (6.6), we find that a surface electron trap density of ca. 10^{10} cm^{-2} is sufficient to explain the observed electrical behavior.

Effects of top electrode contact, applied bias voltage and nanowire passivation on the mobility of the TiO_2 nanowire arrays were also investigated. As can be seen in table 6.1, for TiO_2 nanowire samples coated with titanium top contacts, different applied bias voltages of 2, 5 and 10 volts did not result in noticeable change in the obtained mobility value. It has also been shown that under the same applied bias, the mobility value is independent of top metal contact (aluminum and titanium in this case) as long as said contact is ohmic.

Top Contact	**Applied Bias Voltage (V)**	**SAM Passivation**	**Transit Time (s)**	**Electron Mobility** $(\frac{cm^2}{Vs})$
Titanium	2	No	3.6×10^{-4}	2×10^{-5}
Titanium	5	No	8.6×10^{-4}	0.3×10^{-5}
Titanium	10	No	15×10^{-4}	0.1×10^{-5}
Aluminum	2	No	3.4×10^{-4}	2.1×10^{-5}
Aluminum	3	Yes	5.9×10^{-7}	8.1×10^{-3}

Table 6.1 Electron transit time and mobility along single crystal rutile TiO_2 nanowires under different applied bias voltages and top contacts and effect of SAM passivation on them.

As mentioned earlier, surface traps are considered to be the dominant sources of lowering the mobility of the charge carriers in our nanowire samples. To address this issue, a self-assembled monolayer (SAM) of nonanoic acid was coated onto the walls of nanowire arrays. To do this, a nanowire sample was soaked in 1 mM solution of nonanoic acid in hexane for 12 hours. As can

be seen in table 6.1, electron mobility in SAM coated sample increased about 2-3 orders of magnitude compared to blank nanowires which is an indication of passivation of surface traps of TiO_2 nanowire arrays.

As discussed, we considered SCLC to be the dominant current mechanism in our rutile TiO_2 nanowire samples. Investigating the contribution of other current mechanisms such as Fowler-Nordheim (FN), Poole-Frenkel (PF) and Schottky might be interesting. A brief explanation of each mechanism is provided in the appendix section of the present thesis. Further experiments such as collecting temperature dependent current-voltage data and fitting them to different transport models are required to study the impact of each mechanism. As depicted in the appendix, a preliminary study has been performed.

6.4. Conclusions

The close correspondence between the electron mobility values extracted from three different techniques provides high confidence in the accuracy of the measurements. The averaged effective electron mobility for rutile nanowires in this thesis (1.9×10^{-5} $cm^2V^{-1}s^{-1}$) is more than three orders of magnitude lower than the value of 0.1 cm^2 measured in bulk single crystals of reduced rutile[273]. The value of the diffusion coefficient calculated from our measured mobility using the Einstein relation is (3–7) $\times 10^{-7}$ cm^2s^{-1}, which agrees well with the estimates obtained for single crystal rutile nanowires by Feng et al.[274] from intensity-modulated photocurrent and photovoltage spectroscopy (IMPS/IMVS) at low carrier densities. Likewise, Enache-Pommer et al. obtained a transport time constant >1 ms from IMPS in dye-sensitized rutile NWs synthesized by the hydrothermal method[275]. We attribute the difference in mobilities between rutile nanowires and bulk single crystals primarily to trapping states in the bulk and at the surface. Due to the relatively large lateral surface area of the rutile nanowires, dangling bonds and other

defects are expected at the surface. In addition, impurity atoms in the nanowires may act as bulk traps. Increasing the nanowire diameter would also reduce the relative influence of surface states (Eq. (6.6)). Further studies are planned to understand the nature of surface states in rutile nanowires in order to passivate them.

In dye-sensitized and bulk heterojunction rutile nanowire photovoltaics, the large number of electrons injected into the conduction band of rutile by panchromatic absorption of intense AM1.5 sunlight by the sensitizer, will fill traps and result in a higher effective mobility. Therefore, the extracted SCLC-TOF mobility establishes a lower limit for majority carrier transport rates in rutile nanowires. The measurement of the mobility by SCLC-TOF is also useful because the transport more realistically simulates charge transport in device operating conditions than either field-effect mobility[270] or time-domain terahertz conductivity[276].

Chapter 7

7. Magnetic-Field-Assisted Electrochemical Anodization[1]

7.1. Introduction

The potential of nanomaterials to offer unique properties and improved performance in a variety of sensing, energy harvesting and biomedical applications is responsible for the intense research activities in nanoscience and nanotechnology. From the very beginning, it has always been recognized that interfacing nanostructures with the macroscopic world to utilize their full potential would require the use of microstructures as intermediaries. However in many cases, techniques to perform such interfacing have lagged behind advances in the synthesis and property-engineering of nanomaterials. For instance, there has been impressive progress in controlling the geometrical and morphological properties of anodically formed TiO_2 nanotube arrays (length, wall thickness, pore diameter and pattern order)[192, 277, 278] over a very wide range, as well as generating more complex structures (multipodal[279], hierarchical[280] and periodically modulated TiO_2 nanotube arrays[281-283]) by optimizing anodization parameters such as applied voltage, electrolyte composition, temperature, pH and anodization time. Although such self-organized, vertically oriented TiO_2 nanotube arrays have been found to be promising for deployment in liquid junction dye-sensitized and solid-state ordered heterojunction solar cells,[9, 72-74, 114, 115, 284, 285] water photoelectrolysers and photocatalysts,[75-77] supercapacitors,[286-289] gas sensors,[78, 79, 290] stem cell differentiators,[80, 81, 291] glucose sensors,[82, 83] biomarker assays[84, 292] and

---

[1]Results of this research work were published as a journal paper entitled "Magnetic Field-Assisted Electroless Anodization: TiO_2 Nanotube Growth on Discontinuous, Patterned Ti Films", J. Mater. Chem. A, 2, 13810-13816 (2014).

drug delivery,[86, 87, 293] very little progress has been made in integrating TiO_2 nanotubes with microsystems.

The main obstacle for integration and interfacing with microscale structures has been the requirement of a continuous, conducting, vacuum deposited thin film of Ti as a necessary pre-requisite for subsequent anodic transformation into TiO_2 nanotubes (Figure 7.1). In applications such as micromachined resonators, TiO_2 nanotube arrays are often sought to be formed on high-aspect ratio features as depicted in Figure 7.1.a. When narrow gaps critical to device operation are present between high aspect ratio features, as is often the case with lateral resonators and comb-drives, the process of vacuum deposition to form the precursor Ti films closes the narrow gaps (Figure 7.1b and c), which are very difficult to subsequently re-open following the formation of TiO_2 nanotubes. When wide gaps are present between adjacent high-aspect ratio features, thermal evaporation of the titanium film results in discontinuous films due to poor step coverage, thus terminating the anodization process (Figure 7.1b). Sputtering Ti films results in better step coverage compared to evaporation, but the lower film thickness along the step-walls and non-uniform electric field distribution result in non-uniform nanotube formation and/or film discontinuities due to certain areas of the Ti film fully transforming into insulating TiO_2 before others (Figure 7.1c). This illustrates the near-incompatibility of the currently used TiO_2 nanotube growth process with high-aspect ratio micromachining. These problems, while reduced in severity, are nevertheless present even for low-aspect ratio micromachining. Another source of problems during integration and interfacing of the microscale with the nanoscale is the non-uniform growth of TiO_2 nanotubes on a substrate containing both conductive and non-conductive areas. Figure 7.1d illustrates a configuration consisting of TiO_2 nanotube arrays on metal electrodes separated by a dielectric, one that is often required to make electrical contact to the nanotube arrays. A key problem in transforming a Ti film deposited on such a hybrid metal-

dielectric surface is that the areas above the metal electrodes experience faster rates of anodization due to the higher conductivity resulting in non-uniform TiO_2 nanotube arrays (Figure 7.1e and f).

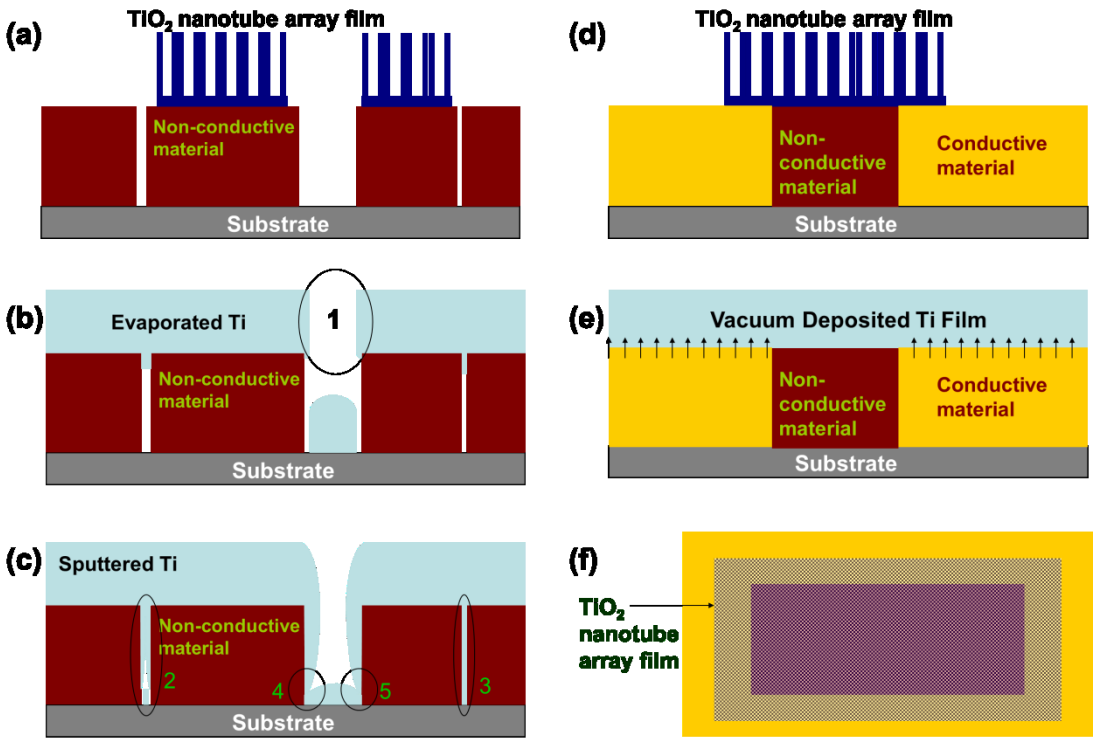

Figure 7.1 Schematic illustrations of patterned and micromachined cross-sections (a) Desired configuration of metal oxide nanotube arrays in defined areas of a substrate over patterned high-aspect ratio features (b, c) Profile generated by vacuum deposition of Ti on to a patterned surface containing high-aspect ratio features separated by wide and narrow gaps (d, e, f) Desired configuration, field and conduction non-uniformities, and expected top-view for nanotube arrays over a composite surface. See text for further explanation.

In order to achieve more structural complexity in TiO_2 nanotube arrays for present and emerging application, introducing new parameter(s) to achieve this goal is much needed, especially because on the synthetic side, exploration of the parameter space associated with the existing variables of the anodization process, such as anodization potential, anodization duration and sequencing, type of electrolyte, bath temperature, etc. is approaching exhaustion. Herein we

report on introducing magnetic fields for the first time into the process of anodization to form TiO_2 nanotube arrays. Magnetic fields have been used in the electrochemical synthesis of nanomaterials such as porous silicon and porous III-V semiconductors, but never without direct connection to an electrode in the manner we have described. In all magnetic-field-assisted anodization processes reported thus far, an electrode was connected to the sample during anodization and the external magnetic field was applied to improve a structural property. Such a configuration has been utilized mostly in generating porous Si in which an applied magnetic field led to morphological improvement of porous structure,[294] significant increment in photoluminescence intensity of porous Si[295] and higher porosity.[295] Magnetic fields have been also reported to enhance the controllability of periodic silicon nanostructures[296] and were also exploited in the formation of hole arrays on GaAs surfaces.[297] The innovation in our method relies on the fact that the Ti coated sample is free-standing into the electrolyte and ions are directed towards it using an external magnetic field to generate TiO_2 nanotube arrays. In other words, anodization occurs purely due to the Lorentz-force guided oxidation and etching of Ti/TiO_2 by ions, which releases the anodization process from the constraint of Ti film continuity and the requirement of either the film or substrate to be conductive. The conventional anodization method possesses several drawbacks. Continuity of the deposited Ti film is required when growing TiO_2 nanotubes on various substrates. Hence, nanotube growth through anodization of discontinuous/patterned Ti on a non-conducting substrate is impossible. Herein we show that magnetic-field-assisted anodization can be used to grow nanotubes from a patterned, discontinuous Ti film on a substrate that is at a floating potential in the electrolyte.

7.2. Experimental

Anodization was performed at room temperature in an ethylene glycol (EG)-based electrolyte containing 0.3 wt.% NH_4F and 2 vol.% deionized water at 50 V. The electrochemical cell consisted of a 1-cm spectroscopic cuvette adapted to this experiment. The sample that was sought to be used as a virtual electrode to grow TiO_2 nanotube arrays, was fully immersed into the electrolyte and attached to one of the walls of the cuvette using Kapton tape. The samples used were Ti foils as well as continuous and patterned, discontinuous Ti thin films deposited on different substrates. Patterned substrates containing discontinuous Ti films were created by depositing 400 nm of Ti onto the photolithographically defined features in HPR 504 photoresist by electron beam evaporation and then removing the unwanted metal by lift-off. The electrodes to which a potential difference (using a DC power supply) was applied to produce motion of the ions in the electrolyte were two rectangular Ti foils 5.5 cm x 0.6 cm in size, which were placed against two opposite walls of the cuvette adjacent to the sample wall, with 3.7 cm of their length immersed into the electrolyte. In some cases the surface area of the Ti electrodes was adjusted by covering some areas with parafilm to create windows of defined size exposed to the electrolyte and also to reduce high local electric fields at electrode edges and interfaces. Ti foils were ultrasonically cleaned using Micro-90 solution, deionized water, acetone and isopropanol for 10 min each. The cuvette cell was placed onto a stack of neodymium permanent magnets with magnetic fields of ranging from 0 to 0.8 tesla in total. The magnetic field strength at the sample was measured using a DC Gaussmeter model 1-ST (Alphalab). The orientation of the magnetic fields was perpendicular to the plane of the magnets and therefore, the magnetic field was directed from bottom to the top of the cuvette. The morphologies of the samples subsequent to anodization were imaged using JEOL6301F and Hitachi S4800 field emission scanning electron

microscopes (FESEM). Optical micrographs were obtained using an Axio Lab.A1 microscope (Zeiss) at magnifications of 10-50X. The anodization current densities were measured using a Keithley 4200 semiconductor parameter analyzer and PC-Link multimeter.

7.3. Results and Discussion

Figure 7.2 shows SEM images of three Ti foils placed at different positions in the cuvette cell during magnetic-field-assisted anodization. Looking into the erect electrolyte-filled cuvette from the cathode side, the three Ti foils were placed as follows: one foil at the left-hand-side (LHS) of the cathode while no electrode was connected to it, a second foil in front of and opposite to the cathode while electrically connected to the positive terminal of the power supply and a third foil at the right-hand-side (RHS) of the cathode with no electrode connection respectively. Nanotube growth on the LHS foil occurs without any electrode connection (Figure 7.2a), and is attributed to the negative ion deflection towards the foil using Lorentz force generated by external magnetic field. These negative ions include both film forming, oxidizing species such as OH^- and O^{2-}, and film etching species such as F^-. The magnetic field oriented along the height of the cuvette from the bottom to top, was responsible for steering the negatively charged oxide, hydroxide and fluoride ions to the left while they were transiting from cathode to anode under the influence of the applied electrochemical voltage. The Hall voltage thus set-up by the magnetic field-induced an asymmetric distribution of ionic charge carriers and produced virtual electrodes on either side of the cathode. In general, titania nanotube growth occurs due to the simultaneous occurrence of field-assisted oxidation, migration and dissolution processes. The OH^- and O^{2-} ions deflected toward the LHS electrode can produce oxidation and similarly deflected F^- ions can produce dissolution. Instead of the oxidation and dissolution processes being field-assisted, they are now assisted by the momentum of the impinging ions.

However the sign of the Hall voltage is such as to oppose further movement of negative charge toward the virtual electrode. The electric field that results across the LHS Ti foil-electrolyte interface is opposite to that required for the migration of positive ions. This suggests that field-assisted migration of positively charged ions is almost absent in the process discussed and provides the further insight that field-assisted migration of positively charged metal ions from the Ti bulk toward the electrolyte interface is not essential to the nanotube growth process. Nanotube growth on the Ti foil opposite the cathode constituting the anode of the circuit merely confirms the conventional anodic formation of TiO_2 nanotubes (Figure 7.2b). The importance of the Lorentz force was verified by the absence of nanotube formation at the RHS foil (Figure 7.2c) toward which only positive ions are deflected.

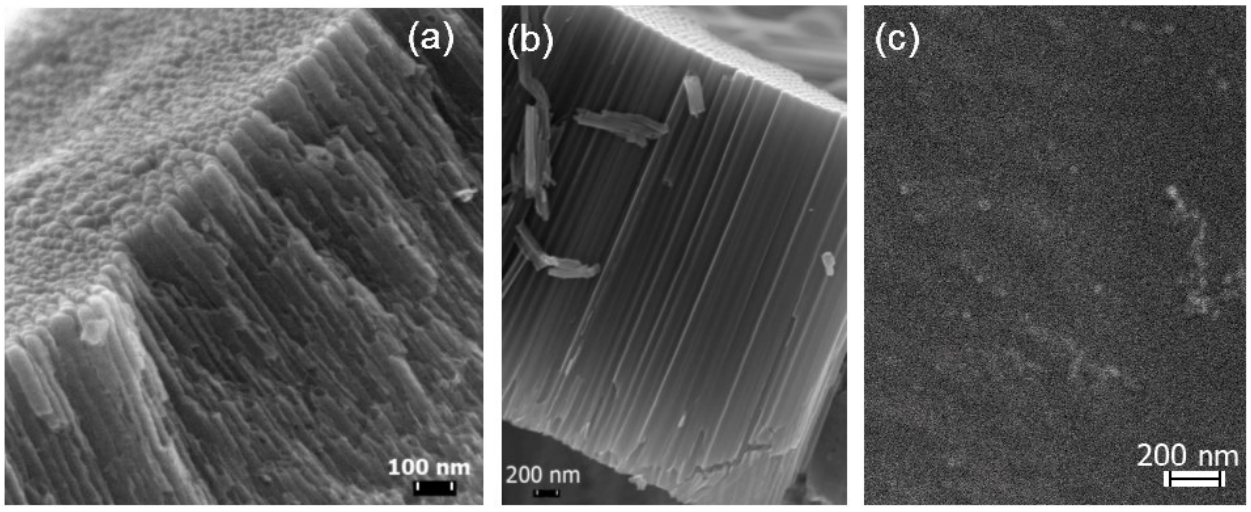

Figure 7.2 SEM images of Ti foils anodized in presence of magnetic field and placed into the cuvette a) at left-hand-side of the cathode (no electrode connected) b) in front of cathode (connected to the anode electrode) and c) at right-hand-side of the cathode (no electrode connected).

Being able to fabricate TiO_2 nanotube arrays onto a substrate without any electrical connection is advantageous since it opens a way forward to grow nanotube arrays through the

anodization of discontinuous Ti films deposited on substrates of any conductivity. To verify this possibility, we subjected a patterned, discontinuous Ti film to the same magnetic-field assisted anodization process. Figure 7.3 is a schematic of the experimental configuration used for this experiment.

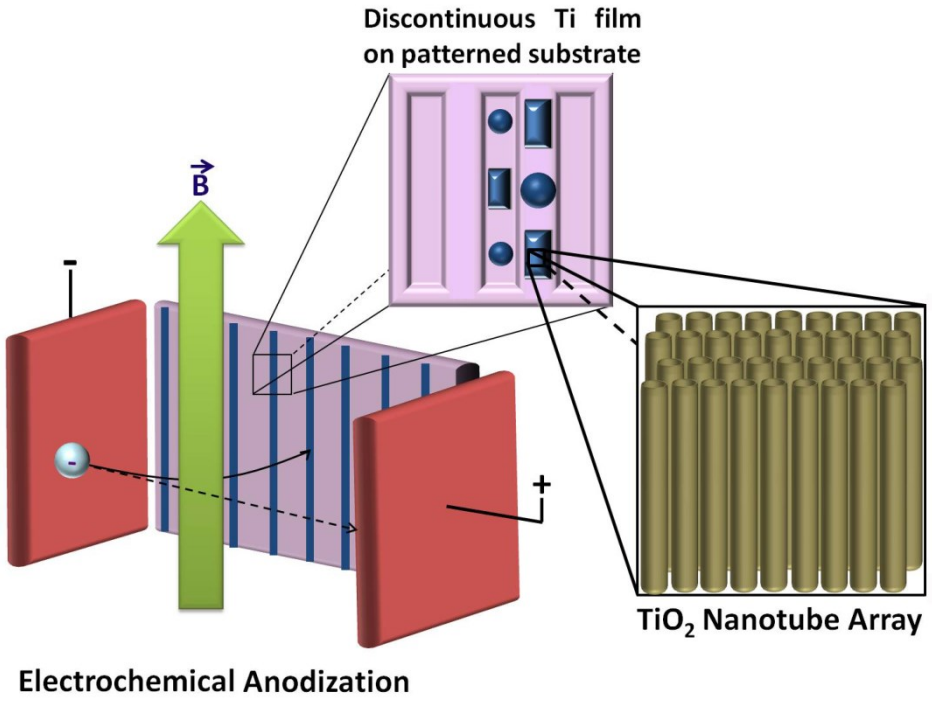

Figure 7.3 Cartoon showing patterned, discontinuous Ti film sample without any direct electrical connection placed along the wall in the cuvette electrochemical cell on the left hand side (LHS) of the cathode. The Ti on the LHS sample is transformed into TiO2 nanotubes upon magnetic field-assisted virtual anodization.

Figure 7.4a shows the optical microscope image of a 400 nm-thick discontinuous Ti film deposited onto Si substrate. The patterned sample was placed against the LHS wall of the cuvette electrochemical cell with no electrode connection while both cathode and anode were Ti foils. Figure 7.4b and c show SEM images of two different patterns comprised of anodized TiO_2 nanotube arrays in which SEM insets represent higher magnification images of gap area,

confirming the magnetic field-assisted formation of TiO_2 nanotube arrays from discontinuous Ti films on arbitrary substrates. Lower SEM inset in Figure 7.4b show the nanotube arrays after top debris layer was etched away using SF_6 gas through reactive ion etching (RIE). Color images in the insets of Figure 7.4b and c are optical micrographs obtained after anodization in which the variation in the color due to optical interference is a distinctive indication of the presence of an anodized oxide film. Cross-sectional SEM image of the grown discontinuous TiO_2 nanotube arrays is depicted in Figure 7.4d.

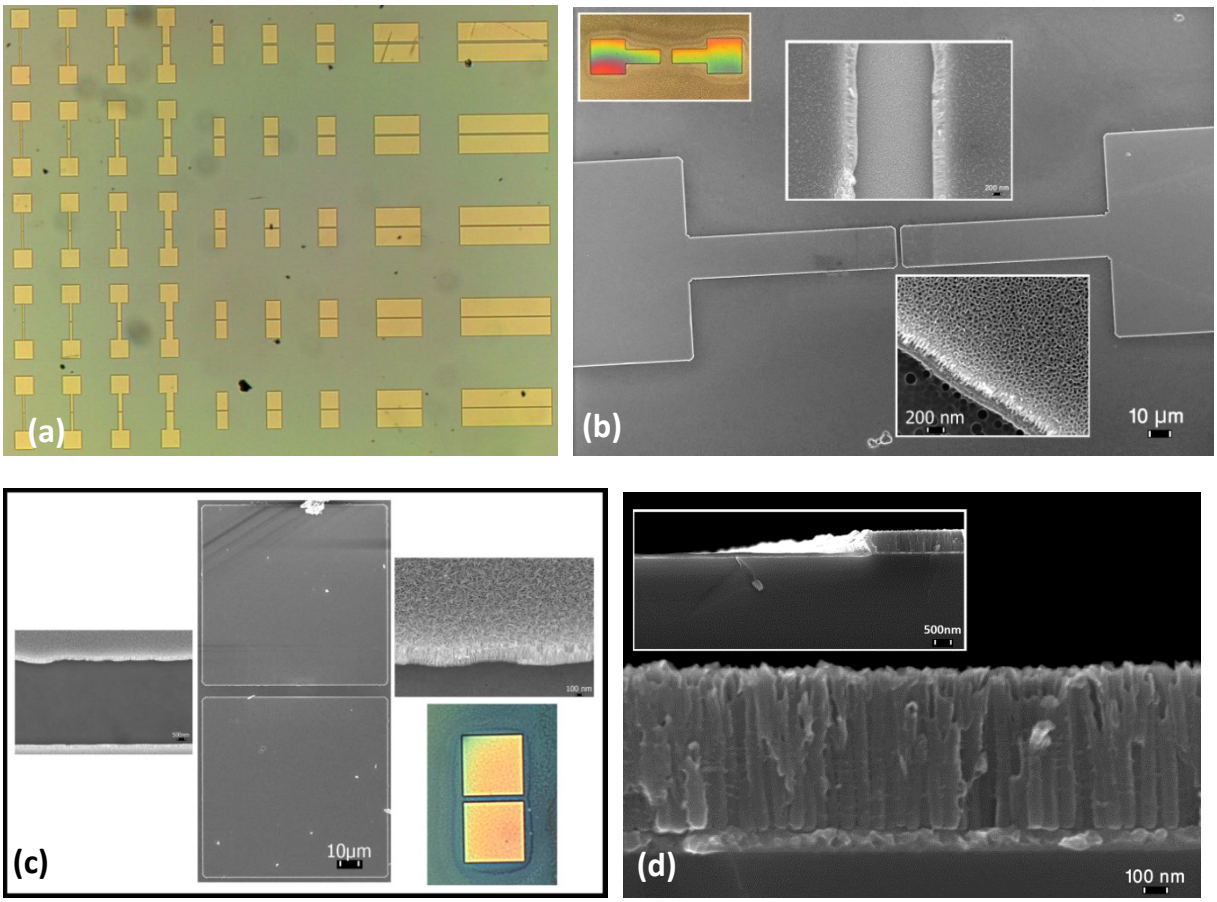

Figure 7.4 (a) Optical micrograph (10X magnification) of patterned Ti film onto Si wafer. (b) and (c) top view SEM and optical microscopy images and (d) cross-sectional SEM images of TiO2 nanotube arrays grown without any electrode connection to the sample.

Herein we also show that the applied magnetic field can be used to control the morphology of the TiO_2 nanotube arrays grown on the Ti sample connected to the anode and placed in front of the cathode electrode. The anodization rate (determinative of nanotube length) can be readily modulated by manipulating the magnetic field strength. Figure 7.5a shows the current density between the cathode and anode (both Ti foils) with, and without applied magnetic field, during anodization for anode surface areas of 0.77 and 1.16 cm^2 respectively. It may be observed that the applied magnetic field during anodization decreases the Faradaic efficiency of nanotube formation at the anode due to the Lorentz force-induced deflection of ions towards LHS and RHS, hence reducing the number of the ions reaching the anode. This manifests itself in the lower anodization current density (Figure 7.5a) during the pitting and nucleation stages of nanotube growth, and in the lower nanotube lengths achieved (Figure 7.5b and c) when a magnetic field is present. This points to the ability of the magnetic field to control the length of nanotubes grown on the front Ti foil (electrical anode) without changing any other anodization parameter.

The 1 cm inter-electrode distance resulted in high electric fields in the electrolyte, which promoted the full dissociation of the dissolved salt. Since a 1-cm cuvette was used as the electrochemical cell, a small amount of the electrolyte was present during anodization (only about 3.8 mL). Due to the above two factors, the electrolyte became fully ionized several minutes into the anodization process if the anode surface area was large enough (1.16 cm^2 in this case) and the electrolyte turned highly conductive. The resulting high currents raised the electrolyte temperature to a level where the cuvette melted and nanotube arrays onto front foil were damaged due to being harshly attacked by fluoride ions. For the utilized setup configuration and the applied voltage of 50 V we found the optimum anode surface area to be in the range of

0.8 to 1.1 cm^2 beyond which despite generating TiO_2 nanotube arrays on the LHS foil (in the presence of the magnetic field), nanotube arrays on the front Ti foil anode get damaged. If the anode surface area is smaller than 0.8 cm^2, the nanotube array onto LHS Ti sample is not generated because the current density is too small to be efficiently deflected towards the left sample by the Lorentz force ($\vec{F} = q\vec{v} \times \vec{B}$). For anode surface areas within the optimum range, TiO_2 nanotubes are grown onto both front foil (electrical anode) and Ti-coated LHS samples (no electrode connection) using magnetic-field-assisted anodization.

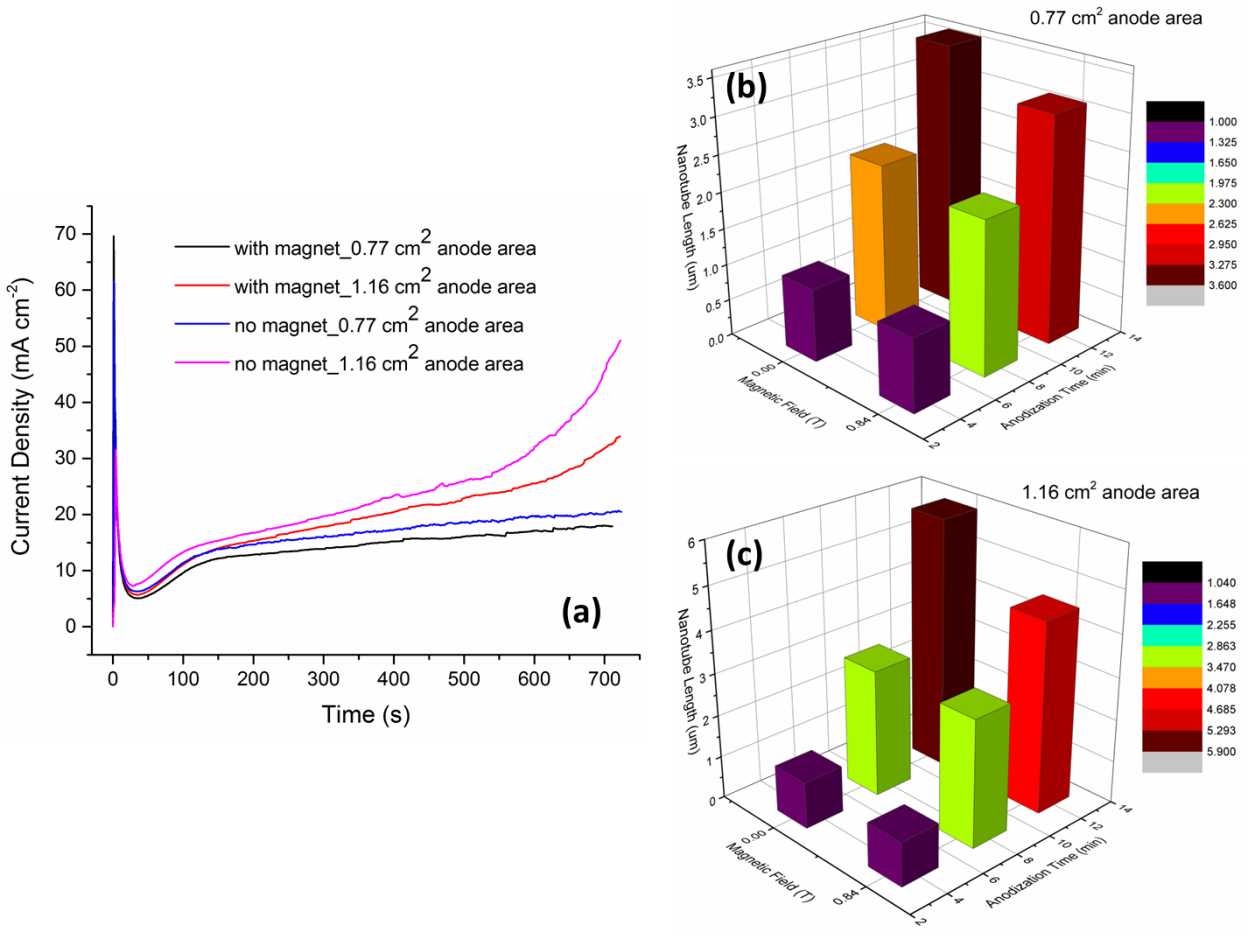

Figure 7.5 (a) Current density plots during anodization of titania nanotube arrays for 0.77 and 1.16 cm2 anode areas with/without applied magnetic field (b, c) Variation of nanotube length as a function of magnetic field strength and anodization duration for sample areas of 0.77 cm2 and 1.16 cm2 respectively.

7.4. Conclusions

We believe magnetic-field-assisted electrochemical anodization to be superior to the conventional anodization method since addresses many of its drawbacks. First of all, the sample (Ti foil or Ti coated substrate) is fully immersed into the electrolyte allowing utilization of its full area which is more cost effective. It also enables us to mount very small sized samples and grow titania nanotube arrays without any electrode connection on patterned substrates of any conductivity. Consequently, Ti film continuity is not needed during nanotube growth. This is of special importance for growing TiO_2 nanotubes onto small electronic chips or lab-on-a-chip devices. Traditionally, the Ti metal needed to be deposited everywhere on the substrate as a blanket film to provide the required conductivity for anodization process. Patterning the nanotubes after their growth, is a huge challenge when dealing with very small gaps and hitherto prevented the integration of TiO_2 nanotube arrays with MEMS devices, porous substrates and substrates containing nanostructures such as oriented nanotube/nanowire/nanopore arrays of metals, dielectrics and semiconductors. Therefore demonstrated magnetic field-assisted electroless anodization process greatly expands the type of substrates on which TiO_2 nanotube arrays may be formed. Since the sample is not partially out of the electrolyte, no precaution is required to tackle the faster anodization issue at electrolyte/air interface. This will open a window towards much easier incorporation of TiO_2 nanotube arrays onto MEMS devices, chip-sized supercapacitors, microelectrocatalysts, etc. and also enable improved interfacing of nanotubes with the macroscale.

The magnetic field is an anodization parameter which can be used for morphology control of the fabricated TiO_2 nanotube arrays, and may also be easily extended to the formation of other nanostructured valve metals such as Al_2O_3, HfO_2, ZrO_2, Ta_2O_5, etc. The Lorentz-force

driven electroless anodization demonstrated by us may also provide deep insights into the anodization process. For instance, field-assisted migration was found to be unimportant to the electroless anodization process.

Chapter 8

8. Conclusion and future research works

In this chapter a summary of this dissertation and its contribution is presented. A description of new problems for future research directions is also provided.

8.1. Conclusion and summary of the contributions

The main focus of this thesis was introducing novel nanostructures of TiO_2 to address the new requirements of variety of applications, studying their fundamental properties such as interaction with light and charge carrier transport, deterministic placement of chromophores onto the nanostructures, studying non-radiative resonant energy transfer under proposed method of chromophore placement and finally improving the method of anodic growth of TiO_2 nanotube arrays by introducing a magnetic field into the process of electrochemical anodization for the first time.

Very large diameter TiO_2 nanotube arrays were generated in which the inner diameter of the nanotubes were for the first time comparable with the wavelength of visible light. Their interaction with visible light was studied, similar nanotubes were simulated using FDTD method and showed that simulation results were in agreement with experimentally obtained data. Developing such a 3-D FDTD simulation model was performed for the first time and it is advantageous for the studies in this field. Introduced model enables the researchers to carry out the simulation of their desired TiO_2 nanostructures, test their properties and optimize it to fit well into a specific application and then start to practically fabricate it. This will save both time and money by reducing trial and error cycles.

Multipodal TiO_2 nanotubes were generated in which nanotubes possessed more than one leg. The process by which such complex nanostructures were generated was described by introducing a phenomenon named "nanotube combination". It was shown that nanotube combination starts with the formation of tapered nanotubes and a model for the process of formation of tapered nanotubes was presented. Nanotube combination was attributed to the capillary forces generated during the imbibition of electrolyte into and out of the intertubular spaces between adjacent tapered nanotubes which is strong enough to bend the TiO_2 nanotubes by tens of degrees. In terms of applications, multipodal TiO_2 nanotubes provide unique advantages such as the feasibility of distinct filling/functionalizing of individual legs which would be beneficial for multiplexed sensing as well as multiplexed drug delivery. Since nanotubes with more than one leg provide better attachment to the surface, multipodal nanotubes are ideal candidates for applications that involve bearing heavy loads.

Deterministic placement of distinct chromophores into two different sites in the structure of nanoporous AAO was successfully carried out which is important from the point of view of several different functions. As mentioned, deterministic placement is a key factor in functionalization of complex nanostructures including generated multipodal TiO_2 nanotubes and obtained experiences during this project would be helpful in achieving such a goal. Moreover an appropriate arrangement was presented for the placement of donor-acceptor dyes in which they were separately embedded into the wall cracks and coated onto the walls of porous AAO respectively and an efficient non-radiative exciton transfer (FRET) was shown to happen under such a configuration. Such a successfully employed chromophore placement geometry could be utilized int the nanostructures of other materials such as TiO_2. This will be discussed in more details in proposed future works section.

Time of flight measurement technique was used to perform for the first time a direct study on the charge carrier transport behavior of single crystal vertically oriented rutile TiO_2 nanowire arrays. When charge carrier mobility is indirectly inferred from techniques such as impedance/intensity-modulated spectroscopy in nanotube/nanowire arrays utilized in dye sensitized solar cell for example, it does not provide a picture of the real charge carrier mobility and traps in bare nanostructures since surface traps for instance are already passivated by sensitizers. Our direct measurement using TOF and SCLC methods revealed that mobility in bare TiO_2 rutile nanowire arrays was close to 1.95×10^{-5} $cm^2V^{-1}s^{-1}$ i.e. nearly five orders of magnitude lower than in bulk single crystal rutile. An equilibrium free electron concentration of $\sim 10^{14}$ cm^{-3} and a trap density of 3.5×10^{16} cm^{-3} in rutile nanowires were also calculated. Collected data points to a large number of surface-located deep electron traps, attributable to a moderate intrinsic electron concentration and a high surface-to-volume ratio of the nanowire arrays. It shows that the performance of the applications relying on charge transport of TiO_2 nanowires would dramatically improve if pre-reduction of traps was carried out.

A magnetic field was employed for the first time in the process of anodic growth of TiO_2 nanotube arrays. The significant advantage of magnetic-field-assisted anodization is that it enables growth of TiO_2 nanotube arrays by anodization of discontinuous or patterned Ti thin films. A patterned thin layer of Ti was generated using lift-off to produced separate metallic Ti structures with a vast range of dimensions and morphologies. Using magnetic field into the process of electrochemical anodization under optimized conditions we transformed the patterned Ti into TiO_2 nanotube arrays without even connecting any electrode to the sample. Now using present technique it is possible to selectively deposit Ti on pre-structured samples such as MEMS devices and turn them into TiO_2 nanotube arrays without the electrical continuity of the

Ti film being a concern. On the other hand, since the sample is completely immersed into the electrolyte during nanotube growth and there is no electrode connection, very small-size samples such as electronic chips can benefit from being incorporated with TiO_2 nanotube arrays using our newly developed technique.

8.2. Future work directions

Herein there is a definition of some research problems in order to extend the scope of our present research works.

8.2.1. Surface enhanced Raman scattering using large diameter TiO_2 nanotube arrays

Generated large diameter TiO_2 nanotube arrays with diameters comparable with the wavelength of the optical light can be coated with appropriate organic dyes and get filled with noble metals such as gold and silver. Such structure would be ideal for performing surface-enhanced Raman scattering (SERS). Such nanotube arrays work better for SERS compared to conventional titania nanotube arrays which possess diameters much smaller than the wavelength of the visible light since Raman modes need to be excited using visible and near-IR radiations and their diameter dimension is already in that range.

8.2.2. Multi-functionalization of multipodal TiO_2 nanotube arrays

As mentioned before, one of the superior advantages of generated multipodal TiO_2 nanotubes is the possibility of distinctive filling and functionalization of different legs. We propose on utilizing multipodal TiO_2 nanotubes in multi-sensing and also delivery of multiple drugs. Physical properties of liquids including viscosity can be used to control the penetration of desired

solutions into specific legs with determined pore diameter. Solution may contain drug or material is to be coated onto the inner wall or filled into different legs.

8.2.3. Applying crack-wall geometry of chromophore placement into TiO_2 nanotube arrays

In chapter 5 it was shown that efficient FRET occurred when chromophores placed distinctively into the wall cracks as well as on the wall surfaces of nanoporous AAO. We propose using the same geometry of chromophore placement for TiO_2 nanotube arrays in order to enhance red/near-IR absorption of sensitized nanotubes. We suggest two possible methods for embedding dye/quantum dots into the walls of TiO_2 nanotube arrays. Cracks similar to those present in porous AAO might be generated into the walls of TiO_2 nanotubes by introducing stress during electrochemical anodization which may happen by performing fast anodization. The other method includes coating the wall surfaces with chromophores and burying them under 1-2 nm of TiO_2 or Al_2O_3 layer using atomic layer deposition (ALD). In both cases it will be followed by coating walls with the second type of chromophore. Light absorption enhancement in red/near-IR region using FRET is expected to increase the performance of applications such as photovoltaics which require solar light harvesting.

8.2.4. Studying charge transport behavior of other semiconductor nanostructures using TOF measurement

Research results presented in chapter 6 showed that TOF method enables us to directly study charge transport properties of single crystal vertically oriented rutile TiO_2 nanowire arrays. TOF along with SCLC provided invaluable information on mobility, charge carrier concentration and trap density. We propose extending such measurements to other semiconductor nanostructures such as polycrystalline TiO_2 nanotubes and ZnO nanotube and nanowire arrays. Same

measurements also can be performed when nanostructures are filled/coated with materials such as dyes to study the changes in charge carrier transport. It provides information such as surface trap passivation for instance. We also propose aligning a single nanotube/nanowire between two closely separated metal pads, focusing laser beam onto one and applying potential difference between the pads to study charge carrier transport along a single nanotube/nanowire.

On the same TiO_2 samples we may also study current mechanisms other than SCLC. Poole-Frenkel is very likely to have contribution in our samples which requires more systematic temperature-dependent measurements.

8.2.5. TiO_2 nanotube growth on MEMS devices using magnetic-field-assisted anodization

Newly developed magnetic-field-assisted anodization of TiO_2 nanotube arrays presented in chapter 7 provides for the first time the possibility of titania nanotube growth by anodization of discontinuous Ti thin films. It facilitates the incorporation of TiO_2 nanotube arrays into a variety of microdevices. We propose utilizing this technique for the growth of nanotube arrays on MEMS devices. One possibility is fabrication of MEMS resonators, depositing a Ti thin film on distinct resonating pads by lift-off and transforming it into TiO_2 nanotube arrays by means of new technique. It is difficult to fulfill using conventional anodization method because Ti needs to be coated everywhere to preserve the continuity of the film. After anodization, TiO_2 nanotube arrays need to be patterned to be present onto the resonating pads only. Removing them from very narrow gaps is tough and any remaining Ti will result in device failure. Nanotube arrays grown onto the resonators using magnetic-field-assisted anodization could be functionalized to adsorb biomaterials. Adsorbed biomaterials will add mass thereby shifting the resonant frequency and the resulting structure will function as a highly sensitive biosensor.

Bibliography

1. Drexler, K. E. Nanotechnology: From Feynman to Funding. 2004.

2. Weiss, J.; Takhistov, P.; McClements, D. J., Functional materials in food nanotechnology. *Journal of Food Science* **2006,** *71* (9), R107-R116.

3. Sorrentino, A.; Gorrasi, G.; Vittoria, V., Potential perspectives of bio-nanocomposites for food packaging applications. *Trends in Food Science and Technology* **2007,** *18* (2), 84-95.

4. Li, Q.; Mahendra, S.; Lyon, D. Y.; Brunet, L.; Liga, M. V.; Li, D.; Alvarez, P. J. J., Antimicrobial nanomaterials for water disinfection and microbial control: Potential applications and implications. *Water Research* **2008,** *42* (18), 4591-4602.

5. Fei, J.; Cui, Y.; Yan, X.; Qi, W.; Yang, Y.; Wang, K.; He, Q.; Li, J., Controlled preparation of MnO2 hierarchical hollow nanostructures and their application in water treatment. *Advanced Materials* **2008,** *20* (3), 452-456.

6. Dong, Y.; Bai, Z.; Liu, R.; Zhu, T., Decomposition of indoor ammonia with TiO2-loaded cotton woven fabrics prepared by different textile finishing methods. *Atmospheric Environment* **2007,** *41* (15), 3182-3192.

7. Rengasamy, S.; Eimer, B.; Shaffer, R. E., Simple respiratory protection - Evaluation of the filtration performance of cloth masks and common fabric materials against 20-1000 nm size particles. *Annals of Occupational Hygiene* **2010,** *54* (7), 789-798.

8. Hochbaum, A. I.; Yang, P., Semiconductor nanowires for energy conversion. *Chemical Reviews* **2010,** *110* (1), 527-546.

9. Mor, G. K.; Shankar, K.; Paulose, M.; Varghese, O. K.; Grimes, C. A., Use of Highly-Ordered TiO2 Nanotube Arrays in Dye-Sensitized Solar Cells. *Nano Letters* **2006,** *6* (2), 215-218.

10. Li, H.; Xiao, H. G.; Yuan, J.; Ou, J., Microstructure of cement mortar with nano-particles. *Composites Part B: Engineering* **2004,** *35* (2), 185-189.

11. Qing, Y.; Zenan, Z.; Deyu, K.; Rongshen, C., Influence of nano-SiO2 addition on properties of hardened cement paste as compared with silica fume. *Construction and Building Materials* **2007,** *21* (3), 539-545.

12. Allen, C.; Maysinger, D.; Eisenberg, A., Nano-engineering block copolymer aggregates for drug delivery. *Colloids and Surfaces B: Biointerfaces* **1999,** *16* (1-4), 3-27.

13. OberdÃ¶rster, E., Manufactured nanomaterials (fullerenes, C60) induce oxidative stress in the brain of juvenile largemouth bass. *Environmental Health Perspectives* **2004,** *112* (10), 1058-1062.

14. Zhang, X.; Han, F.; Shi, B.; Farsinezhad, S.; Dechaine, G. P.; Shankar, K., Photocatalytic conversion of diluted CO2 into light hydrocarbons using periodically modulated multiwalled nanotube arrays. *Angewandte Chemie - International Edition* **2012,** *51* (51), 12732-12735.

15. Klaine, S. J.; Alvarez, P. J. J.; Batley, G. E.; Fernandes, T. F.; Handy, R. D.; Lyon, D. Y.; Mahendra, S.; McLaughlin, M. J.; Lead, J. R., Nanomaterials in the environment: Behavior, fate, bioavailability, and effects. *Environmental Toxicology and Chemistry* **2008,** *27* (9), 1825-1851.

16. Baughman, R. H.; Zakhidov, A. A.; De Heer, W. A., Carbon nanotubes - The route toward applications. *Science* **2002,** *297* (5582), 787-792.

17. Mor, G. K.; Varghese, O. K.; Paulose, M.; Shankar, K.; Grimes, C. A., A review on highly ordered, vertically oriented TiO 2 nanotube arrays: Fabrication, material properties, and solar energy applications. *Solar Energy Materials and Solar Cells* **2006,** *90* (14), 2011-2075.

18. Wu, H.; Chan, G.; Choi, J. W.; Ryu, I.; Yao, Y.; McDowell, M. T.; Lee, S. W.; Jackson, A.; Yang, Y.; Hu, L.; Cui, Y., Stable cycling of double-walled silicon nanotube battery anodes through solid-electrolyte interphase control. *Nature Nanotechnology* **2012,** *7* (5), 310-315.

19. Golberg, D.; Bando, Y.; Huang, Y.; Terao, T.; Mitome, M.; Tang, C.; Zhi, C., Boron nitride nanotubes and nanosheets. *ACS Nano* **2010,** *4* (6), 2979-2993.

20. Cui, Y.; Wei, Q.; Park, H.; Lieber, C. M., Nanowire nanosensors for highly sensitive and selective detection of biological and chemical species. *Science* **2001,** *293* (5533), 1289-1292.

21. Law, M.; Greene, L. E.; Johnson, J. C.; Saykally, R.; Yang, P., Nanowire dye-sensitized solar cells. *Nature Materials* **2005,** *4* (6), 455-459.

22. Cui, Y.; Lieber, C. M., Functional nanoscale electronic devices assembled using silicon nanowire building blocks. *Science* **2001,** *291* (5505), 851-853.

23. Huang, M. H.; Wu, Y.; Feick, H.; Tran, N.; Weber, E.; Yang, P., Catalytic growth of zinc oxide nanowires by vapor transport. *Advanced Materials* **2001,** *13* (2), 113-116.

24. Zhao, D.; Feng, J.; Huo, Q.; Melosh, N.; Fredrickson, G. H.; Chmelka, B. F.; Stucky, G. D., Triblock copolymer syntheses of mesoporous silica with periodic 50 to 300 angstrom pores. *Science* **1998,** *279* (5350), 548-552.

25. Tanev, P. T.; Pinnavaia, T. J., A neutral templating route to Mesoporous molecular sieves. *Science* **1995,** *267* (5199), 865-867.

26. Davydov, D. N.; Sattari, P. A.; AlMawlawi, D.; Osika, A.; Haslett, T. L.; Moskovits, M., Field emitters based on porous aluminum oxide templates. *Journal of Applied Physics* **1999,** *86* (7), 3983-3987.

27. Jackson, J. B.; Westcott, S. L.; Hirsch, L. R.; West, J. L.; Halas, N. J., Controlling the surface enhanced Raman effect via the nanoshell geometry. *Applied Physics Letters* **2003,** *82* (2), 257-259.

28. Wu, D.; Liu, X., Optimization of the bimetallic gold and silver alloy nanoshell for biomedical applications in vivo. *Applied Physics Letters* **2010,** *97* (6).

29. Halpern, A. R.; Corn, R. M., Lithographically patterned electrodeposition of gold, silver, and nickel nanoring arrays with widely tunable near-infrared plasmonic resonances. *ACS Nano* **2013,** *7* (2), 1755-1762.

30. Suarez, M. A.; Grosjean, T.; Charraut, D.; Courjon, D., Nanoring as a magnetic or electric field sensitive nano-antenna for near-field optics applications. *Optics Communications* **2007,** *270* (2), 447-454.

31. Huang, Z. M.; Zhang, Y. Z.; Kotaki, M.; Ramakrishna, S., A review on polymer nanofibers by electrospinning and their applications in nanocomposites. *Composites Science and Technology* **2003,** *63* (15), 2223-2253.

32. Deitzel, J. M.; Kleinmeyer, J.; Harris, D.; Beck Tan, N. C., The effect of processing variables on the morphology of electrospun nanofibers and textiles. *Polymer* **2001,** *42* (1), 261-272.

33. Chen, J.; Wang, D.; Xi, J.; Au, L.; Siekkinen, A.; Warsen, A.; Li, Z. Y.; Zhang, H.; Xia, Y.; Li, X., Immuno gold nanocages with tailored optical properties for targeted photothermal destruction of cancer cells. *Nano Letters* **2007,** *7* (5), 1318-1322.

34. Yavuz, M. S.; Cheng, Y.; Chen, J.; Cobley, C. M.; Zhang, Q.; Rycenga, M.; Xie, J.; Kim, C.; Song, K. H.; Schwartz, A. G.; Wang, L. V.; Xia, Y., Gold nanocages covered by smart polymers for controlled release with near-infrared light. *Nature Materials* **2009,** *8* (12), 935-939.

35. Nath, M.; Govindaraj, A.; Rao, C. N. R., Simple synthesis of MoS2 and WS2 nanotubes. *Advanced Materials* **2001,** *13* (4), 283-286.

36. Yella, A.; Mugnaioli, E.; PanthÃ¶fer, M.; Therese, H. A.; Kolb, U.; Tremel, W., Bismuth-catalyzed growth of SnS2 nanotubes and their stability. *Angewandte Chemie - International Edition* **2009,** *48* (35), 6426-6430.

37. Wang, G.; Wang, H.; Ling, Y.; Tang, Y.; Yang, X.; Fitzmorris, R. C.; Wang, C.; Zhang, J. Z.; Li, Y., Hydrogen-treated TiO2 nanowire arrays for photoelectrochemical water splitting. *Nano Letters* **2011,** *11* (7), 3026-3033.

38. Wang, J.; Gudiksen, M. S.; Duan, X.; Cui, Y.; Lieber, C. M., Highly polarized photoluminescence and photodetection from single indium phosphide nanowires. *Science* **2001,** *293* (5534), 1455-1457.

39. Huang, Y.; Duan, X.; Cui, Y.; Lieber, C. M., Gallium Nitride Nanowire Nanodevices. *Nano Letters* **2002,** *2* (2), 101-104.

40. Antonelli, D. M.; Ying, J. Y., Synthesis of hexagonally packed mesoporous TiO2 by a modified sol-gel method. *Angewandte Chemie (International Edition in English)* **1995,** *34* (18), 2014-2017.

41. Li, W. C.; Lu, A. H.; Weidenthaler, C.; SchÃ¼th, F., Hard-templating pathway to create mesoporous magnesium oxide. *Chemistry of Materials* **2004,** *16* (26), 5676-5681.

42. Michailowski, A.; AlMawlawi, D.; Cheng, G. S.; Moskovits, M., Highly regular anatase nanotubule arrays fabricated in porous anodic templates. *Chemical Physics Letters* **2001,** *349* (1-2), 1-5.

43. Qiu, J. J.; Yu, W. D.; Gao, X. D.; Li, X. M., Sol-gel assisted ZnO nanorod array template to synthesize TiO2 nanotube arrays. *Nanotechnology* **2006,** *17* (18), 4695-4698.

44. Tian, Z. R. R.; Voigt, J. A.; Liu, J.; McKenzie, B.; Xu, H. F., Large oriented arrays and continuous films of TiO2-based nanotubes. *Journal of the American Chemical Society* **2003,** *125* (41), 12384-12385.

45. Im, B.; Joshi, U. A.; Lee, K. H.; Lee, J. S., Growth of single crystalline barium titanate nanowires from TiO2 seeds deposited on conducting glass. *Nanotechnology* **2010,** *21* (42), 425601.

46. Liu, B.; Boercker, J. E.; Aydil, E. S., Oriented single crystalline titanium dioxide nanowires. *Nanotechnology* **2008,** *19* (50), 7.

47. Feng, X. J.; Shankar, K.; Varghese, O. K.; Paulose, M.; Latempa, T. J.; Grimes, C. A., Vertically Aligned Single Crystal TiO2 Nanowire Arrays Grown Directly on Transparent Conducting Oxide Coated Glass: Synthesis Details and Applications. *Nano Letters* **2008,** *8* (11), 3781-3786.

48. Kolen'ko, Y. V.; Kovnir, K. A.; Gavrilov, A. I.; Garshev, A. V.; Frantti, J.; Lebedev, O. I.; Churagulov, B. R.; Van Tendeloo, G.; Yoshimura, M., Hydrothermal synthesis and characterization of nanorods of various titanates and titanium dioxide. *Journal of Physical Chemistry B* **2006,** *110* (9), 4030-4038.

49. Gong, D.; Grimes, C. A.; Varghese, O. K.; Hu, W. C.; Singh, R. S.; Chen, Z.; Dickey, E. C., Titanium oxide nanotube arrays prepared by anodic oxidation. *J. Mater. Res.* **2001,** *16* (12), 3331-3334.

50. Mor, G. K.; Varghese, O. K.; Paulose, M.; Mukherjee, N.; Grimes, C. A., Fabrication of tapered, conical-shaped titania nanotubes. *J. Mater. Res.* **2003,** *18* (11), 2588-2593.

51. Mor, G. K.; Varghese, O. K.; Paulose, M.; Grimes, C. A., Transparent highly ordered TiO2 nanotube arrays via anodization of titanium thin films. *Advanced Functional Materials* **2005,** *15* (8), 1291-1296.

52. Grimes, C. A., Synthesis and application of highly ordered arrays of TiO2 nanotubes. *Journal of Materials Chemistry* **2007,** *17* (15), 1451-1457.

53. Carp, O.; Huisman, C. L.; Reller, A., Photoinduced reactivity of titanium dioxide. *Progress in Solid State Chemistry* **2004,** *32* (1-2), 33-177.

54. Asahi, R.; Morikawa, T.; Ohwaki, T.; Aoki, K.; Taga, Y., Visible-light photocatalysis in nitrogen-doped titanium oxides. *Science* **2001,** *293* (5528), 269-271.

55. Dambournet, D.; Belharouak, I.; Amine, K., Tailored Preparation Methods of TiO(2) Anatase, Rutile, Brookite: Mechanism of Formation and Electrochemical Properties. *Chemistry of Materials* **2010,** *22* (3), 1173-1179.

56. Li, J. G.; Tang, C. C.; Li, D.; Haneda, H.; Ishigaki, T., Monodispersed spherical particles of brookite-type TiO2: Synthesis, characterization, and photocatalytic property. *Journal of the American Ceramic Society* **2004,** *87* (7), 1358-1361.

57. Joyce, C. D.; McIntyre, T.; Simmons, S.; LaDuca, H.; Breitzer, J. G.; Lopez, C. M.; Jansen, A. N.; Vaughey, J. T., Synthesis and electrochemical evaluation of an amorphous titanium dioxide derived from a solid state precursor. *Journal of Power Sources* **2010,** *195* (7), 2064-2068.

58. Mahshid, S.; Askari, M.; Ghamsari, M. S., Effect of brookite presence on nanocrystalline anatase - rutile phase transformation. *International Journal of Nanotechnology* **2009,** *6* (10-11), 961-972.

59. Li, Y.; Ishigaki, T., Thermodynamic analysis of nucleation of anatase and rutile from TiO2 melt. *Journal of Crystal Growth* **2002,** *242* (3â€“4), 511-516.

60. Li, W.; Ni, C.; Lin, H.; Huang, C. P.; Shah, S. I., Size dependence of thermal stability of <equation>TiO₂</equation> nanoparticles. *Journal of Applied Physics* **2004,** *96* (11), 6663-6668.

61. Hanaor, D. H.; Sorrell, C., Review of the anatase to rutile phase transformation. *Journal of Materials Science* **2011,** *46* (4), 855-874.

62. Tang, H.; Berger, H.; Schmid, P. E.; LÃ©vy, F.; Burri, G., Photoluminescence in TiO2 anatase single crystals. *Solid State Communications* **1993,** *87* (9), 847-850.

63. Labat, F. d. r.; Baranek, P.; Domain, C.; Minot, C.; Adamo, C., Density functional theory analysis of the structural and electronic properties of TiO2 rutile and anatase polytypes: Performances of different exchange-correlation functionals. *The Journal of Chemical Physics* **2007,** *126* (15), -.

64. Scanlon, D. O.; Dunnill, C. W.; Buckeridge, J.; Shevlin, S. A.; Logsdail, A. J.; Woodley, S. M.; Catlow, C. R. A.; Powell, M. J.; Palgrave, R. G.; Parkin, I. P.; Watson, G. W.; Keal, T. W.;

Sherwood, P.; Walsh, A.; Sokol, A. A., Band alignment of rutile and anatase TiO2. *Nat Mater* **2013,** *12* (9), 798-801.

65. Mo, S.-D.; Ching, W. Y., Electronic and optical properties of three phases of titanium dioxide: Rutile, anatase, and brookite. *Physical Review B* **1995,** *51* (19), 13023-13032.

66. Takahashi, Y.; Matsuoka, Y., Dip-coating of TiO2 films using a sol derived from Ti(O-i-Pr)4-diethanolamine-H2O-i-PrOH system. *Journal of Materials Science* **1988,** *23* (6), 2259-2266.

67. Cetinorgu, E.; Geron, N.; Goldsmith, S.; Boxman, R. L., Phase determination of filtered vacuum arc deposited TiO(2) thin films by optical modeling. *Thin Solid Films* **2009,** *518* (4), 1060-1066.

68. Richter, C.; Schmuttenmaer, C. A., Exciton-like trap states limit electron mobility in TiO2 nanotubes. *Nat Nano* **2010,** *5* (11), 769-772.

69. Yang, Y.; Kim, D.; Yang, M.; Schmuki, P., Vertically aligned mixed V2O5-TiO2 nanotube arrays for supercapacitor applications. *Chemical Communications* **2011,** *47* (27), 7746-7748.

70. Bai, Y.; Park, I. S.; Park, H. H.; Lee, M. H.; Bae, T. S.; Duncan, W.; Swain, M., The effect of annealing temperatures on surface properties, hydroxyapatite growth and cell behaviors of TiO2 nanotubes. *Surface and Interface Analysis* **2010,** *43* (6), 998-1005.

71. Feng, X.; Shankar, K.; Varghese, O. K.; Paulose, M.; Latempa, T. J.; Grimes, C. A., Vertically Aligned Single Crystal TiO2 Nanowire Arrays Grown Directly on Transparent Conducting Oxide Coated Glass: Synthesis Details and Applications. *Nano Letters* **2008,** *8* (11), 3781-3786.

72. Paulose, M.; Shankar, K.; Varghese, O. K.; Mor, G. K.; Grimes, C. A., Application of highly-ordered TiO2 nanotube-arrays in heterojunction dye-sensitized solar cells. *Journal of Physics D-Applied Physics* **2006,** *39* (12), 2498-2503.

73. Kuang, D.; Brillet, J.; Chen, P.; Takata, M.; Uchida, S.; Miura, H.; Sumioka, K.; Zakeeruddin, S. M.; Gratzel, M., Application of highly ordered TiO2 nanotube arrays in flexible dye-sensitized solar cells. *Acs Nano* **2008,** *2* (6), 1113-1116.

74. Jennings, J. R.; Ghicov, A.; Peter, L. M.; Schmuki, P.; Walker, A. B., Dye-sensitized solar cells based on oriented TiO(2) nanotube arrays: Transport, trapping, and transfer of electrons. *Journal of the American Chemical Society* **2008,** *130* (40), 13364-13372.

75. Mor, G. K.; Varghese, O. K.; Paulose, M.; Shankar, K.; Grimes, C. A., A review on highly ordered, vertically oriented TiO2 nanotube arrays: Fabrication, material properties, and solar energy applications. *Solar Energy Materials and Solar Cells* **2006,** *90* (14), 2011-2075.

76. Shankar, K.; Basham, J. I.; Allam, N. K.; Varghese, O. K.; Mor, G. K.; Feng, X. J.; Paulose, M.; Seabold, J. A.; Choi, K. S.; Grimes, C. A., Recent Advances in the Use of TiO(2) Nanotube and Nanowire Arrays for Oxidative Photoelectrochemistry. *Journal of Physical Chemistry C* **2009,** *113* (16), 6327-6359.

77. Shankar, K.; Mor, G. K.; Prakasam, H. E.; Yoriya, S.; Paulose, M.; Varghese, O. K.; Grimes, C. A., Highly-ordered TiO2 nanotube arrays up to 220 mu m in length: use in water photoelectrolysis and dye-sensitized solar cells. *Nanotechnology* **2007,** *18* (6), 11.

78. Mor, G. K.; Carvalho, M. A.; Varghese, O. K.; Pishko, M. V.; Grimes, C. A., A room-temperature TiO2-nanotube hydrogen sensor able to self-clean photoactively from environmental contamination. *J. Mater. Res.* **2004,** *19* (2), 628-634.

79. Paulose, M.; Varghese, O. K.; Mor, G. K.; Grimes, C. A.; Ong, K. G., Unprecedented ultra-high hydrogen gas sensitivity in undoped titania nanotubes. *Nanotechnology* **2006,** *17* (2), 398-402.

80. Park, J.; Bauer, S.; Pittrof, A.; Killian, M. S.; Schmuki, P.; von der Mark, K., Synergistic Control of Mesenchymal Stem Cell Differentiation by Nanoscale Surface Geometry and Immobilized Growth Factors on TiO2 Nanotubes. *Small* **2012,** *8* (1), 98-107.

81. Park, J.; Bauer, S.; von der Mark, K.; Schmuki, P., Nanosize and vitality: TiO2 nanotube diameter directs cell fate. *Nano Lett.* **2007,** *7* (6), 1686-1691.

82. Bao, S. J.; Li, C. M.; Zang, J. F.; Cui, X. Q.; Qiao, Y.; Guo, J., New nanostructured TiO2 for direct electrochemistry and glucose sensor applications. *Advanced Functional Materials* **2008,** *18* (4), 591-599.

83. Wang, C. X.; Yin, L. W.; Zhang, L. Y.; Gao, R., Ti/TiO2 Nanotube Array/Ni Composite Electrodes for Nonenzymatic Amperometric Glucose Sensing. *J. Phys. Chem. C* **2010,** *114* (10), 4408-4413.

84. Kar, P.; Pandey, A.; Greer, J. J.; Shankar, K., Ultrahigh sensitivity assays for human cardiac troponin I using TiO(2) nanotube arrays. *Lab Chip* **2012,** *12* (4), 821-828.

85. Popat, K. C.; Leoni, L.; Grimes, C. A.; Desai, T. A., Influence of engineered titania nanotubular surfaces on bone cells. *Biomaterials* **2007,** *28* (21), 3188-3197.

86. Gulati, K.; Aw, M. S.; Losic, D., Drug-eluting Ti wires with titania nanotube arrays for bone fixation and reduced bone infection. *Nanoscale Res. Lett.* **2011,** *6*, 6.

87. Song, Y. Y.; Schmidt-Stein, F.; Bauer, S.; Schmuki, P., Amphiphilic TiO(2) Nanotube Arrays: An Actively Controllable Drug Delivery System. *Journal of the American Chemical Society* **2009,** *131* (12), 4230-+.

88. Liu, C. M.; Chen, C.; Cheng, H. E., Growth Mechanism of TiO2 Nanotube Arrays in Nanopores of Anodic Aluminum Oxide on Si Substrates by Atomic Layer Deposition. *Journal of the Electrochemical Society* **2011,** *158* (3), K58-K63.

89. Macak, J. M.; Tsuchiya, H.; Schmuki, P., High-aspect-ratio TiO2 nanotubes by anodization of titanium. *Angewandte Chemie-International Edition* **2005,** *44* (14), 2100-2102.

90. Albu, S. P.; Ghicov, A.; Aldabergenova, S.; Drechsel, P.; LeClere, D.; Thompson, G. E.; Macak, J. M.; Schmuki, P., Formation of Double-Walled TiO2 Nanotubes and Robust Anatase Membranes. *Advanced Materials* **2008,** *20* (21), 4135-+.

91. Kontos, A. I.; Likodimos, V.; Stergiopoulos, T.; Tsoukleris, D. S.; Falaras, P.; Rabias, I.; Papavassiliou, G.; Kim, D.; Kunze, J.; Schmuki, P., Self-Organized Anodic TiO2 Nanotube Arrays Functionalized by Iron Oxide Nanoparticles. *Chemistry of Materials* **2009,** *21* (4), 662-672.

92. Mohapatra, S. K.; Kondamudi, N.; Banerjee, S.; Misra, M., Functionalization of self-organized TiO2 nanotubes with Pd nanoparticles for photocatalytic decomposition of dyes under solar light illumination. *Langmuir* **2008,** *24* (19), 11276-11281.

93. Kang, S. H.; Kim, H. S.; Kim, J. Y.; Sung, Y. E., An investigation on electron behavior employing vertically-aligned TiO2 nanotube electrodes for dye-sensitized solar cells. *Nanotechnology* **2009,** *20* (35), 6.

94. Mohammadpour, A.; Farsinezhad, S.; Wiltshire, B. D.; Shankar, K., Majority carrier transport in single crystal rutile nanowire arrays. *physica status solidi (RRL) – Rapid Research Letters* **2014**, n/a-n/a.

95. Yoriya, S.; Grimes, C. A., Self-Assembled TiO2 Nanotube Arrays by Anodization of Titanium in Diethylene Glycol: Approach to Extended Pore Widening. *Langmuir* **2009,** *26* (1), 417-420.

96. Lee, J.; Jho, J. Y., Fabrication of highly ordered and vertically oriented TiO2 nanotube arrays for ordered heterojunction polymer/inorganic hybrid solar cell. *Solar Energy Materials and Solar Cells* **2011,** *95* (11), 3152-3156.

97. Shankar, K.; Mor, G. K.; Prakasam, H. E.; Yoriya, S.; Paulose, M.; Varghese, O. K.; Grimes, C. A., Highly-ordered TiO2 nanotube arrays up to 220 Î¼m in length: Use in water photoelectrolysis and dye-sensitized solar cells. *Nanotechnology* **2007,** *18* (6).

98. Wang, J.; Lin, Z., Freestanding TiO2 Nanotube Arrays with Ultrahigh Aspect Ratio via Electrochemical Anodization. *Chemistry of Materials* **2008,** *20* (4), 1257-1261.

99. Macák, J. M.; Tsuchiya, H.; Schmuki, P., High-Aspect-Ratio TiO2 Nanotubes by Anodization of Titanium. *Angewandte Chemie International Edition* **2005,** *44* (14), 2100-2102.

100. Prakasam, H. E.; Shankar, K.; Paulose, M.; Varghese, O. K.; Grimes, C. A., A New Benchmark for TiO2 Nanotube Array Growth by Anodization. *The Journal of Physical Chemistry C* **2007,** *111* (20), 7235-7241.

101. Yin, H.; Liu, H.; Shen, W. Z., The large diameter and fast growth of self-organized TiO2 nanotube arrays achieved via electrochemical anodization. *Nanotechnology* **2010,** *21* (3).

102. Paulose, M.; Prakasam, H. E.; Varghese, O. K.; Peng, L.; Popat, K. C.; Mor, G. K.; Desai, T. A.; Grimes, C. A., TiO2 Nanotube Arrays of 1000 Î¼m Length by Anodization of Titanium Foil:â€‰ Phenol Red Diffusion. *The Journal of Physical Chemistry C* **2007,** *111* (41), 14992-14997.

103. Ito, S.; Zakeeruddin, S. M.; Humphry-Baker, R.; Liska, P.; Charvet, R.; Comte, P.; Nazeeruddin, M. K.; PÃ©chy, P.; Takata, M.; Miura, H.; Uchida, S.; GrÃ¤tzel, M., High-efficiency organic-dye-sensitized solar cells controlled by nanocrystalline-TiO2 electrode thickness. *Advanced Materials* **2006,** *18* (9), 1202-1205.

104. Van Hal, P. A.; Wienk, M. M.; Kroon, J. M.; Verhees, W. J. H.; Slooff, L. H.; Van Gennip, W. J. H.; Jonkheijm, P.; Janssen, R. A. J., Photoinduced electron transfer and photovoltaic response of a MDMO-PPV:TiO2 bulk-heterojunction. *Advanced Materials* **2003,** *15* (2), 118-121.

105. Haque, S. A.; Koops, S.; Tokmoldin, N.; Durrant, J. R.; Huang, J.; Bradley, D. D. C.; Palomares, E., A multilayered polymer light-emitting diode using a nanocrystalline metal-oxide film as a charge-injection electrode. *Advanced Materials* **2007,** *19* (5), 683-687.

106. Nagaveni, K.; Hegde, M. S.; Ravishankar, N.; Subbanna, G. N.; Madras, G., Synthesis and structure of nanocrystalline TiO2 with lower band gap showing high photocatalytic activity. *Langmuir* **2004,** *20* (7), 2900-2907.

107. Yu, J. C.; Yu, J.; Ho, W.; Jiang, Z.; Zhang, L., Effects of F - doping on the photocatalytic activity and microstructures of nanocrystalline TiO 2 powders. *Chemistry of Materials* **2002,** *14* (9), 3808-3816.

108. Fabregat-Santiago, F.; Garcia-Belmonte, G.; Bisquert, J.; Zaban, A.; Salvador, P., Decoupling of transport, charge storage, and interfacial charge transfer in the nanocrystalline TiO2/electrolyte system by impedance methods. *Journal of Physical Chemistry B* **2002,** *106* (2), 334-339.

109. Nelson, J., Continuous-time random-walk model of electron transport in nanocrystalline TiO2 electrodes. *Physical Review B - Condensed Matter and Materials Physics* **1999,** *59* (23), 15374-15380.

110. Van de Lagemaat, J.; Frank, A. J., Nonthermalized electron transport in dye-sensitized nanocrystalline TiO2 films: Transient photocurrent and random-walk modeling studies. *Journal of Physical Chemistry B* **2001,** *105* (45), 11194-11205.

111. Barzykin, A. V.; Tachiya, M., Mechanism of charge recombination in dye-sensitized nanocrystalline semiconductors: Random flight model. *Journal of Physical Chemistry B* **2002,** *106* (17), 4356-4363.

112. Shankar, K.; Bandara, J.; Paulose, M.; Wietasch, H.; Varghese, O. K.; Mor, G. K.; LaTempa, T. J.; Thelakkat, M.; Grimes, C. A., Highly Efficient Solar Cells using TiO2 Nanotube Arrays Sensitized with a Donor-Antenna Dye. *Nano Letters* **2008,** *8* (6), 1654-1659.

113. Zhu, K.; Neale, N. R.; Miedaner, A.; Frank, A. J., Enhanced Charge-Collection Efficiencies and Light Scattering in Dye-Sensitized Solar Cells Using Oriented TiO2 Nanotubes Arrays. *Nano Letters* **2006,** *7* (1), 69-74.

114. Shankar, K.; Mor, G. K.; Paulose, M.; Varghese, O. K.; Grimes, C. A., Effect of device geometry on the performance of TiO2 nanotube array-organic semiconductor double heterojunction solar cells. *Journal of Non-Crystalline Solids* **2008,** *354* (19-25), 2767-2771.

115. Varghese, O. K.; Paulose, M.; Grimes, C. A., Long vertically aligned titania nanotubes on transparent conducting oxide for highly efficient solar cells. *Nature nanotechnology* **2009,** *4* (9), 592-597.

116. Richter, C.; Schmuttenmaer, C. A., Exciton-like trap states limit electron mobility in TiO2 nanotubes. *Nature Nanotechnology* **2010,** *5* (11), 769-772.

117. Feng, X.; Shankar, K.; Paulose, M.; Grimes, C. A., Tantalum-Doped Titanium Dioxide Nanowire Arrays for Dye-Sensitized Solar Cells with High Open-Circuit Voltage. *Angewandte Chemie* **2009,** *121* (43), 8239-8242.

118. Kuo, C. Y.; Tang, W. C.; Gau, C.; Guo, T. F.; Jeng, D. Z., Ordered bulk heterojunction solar cells with vertically aligned Ti O2 nanorods embedded in a conjugated polymer. *Applied Physics Letters* **2008,** *93* (3).

119. Kim, H. S.; Lee, J. W.; Yantara, N.; Boix, P. P.; Kulkarni, S. A.; Mhaisalkar, S.; GrÃ¤tzel, M.; Park, N. G., High efficiency solid-state sensitized solar cell-based on submicrometer rutile TiO2 nanorod and CH3NH3PbI3 perovskite sensitizer. *Nano Letters* **2013,** *13* (6), 2412-2417.

120. Kumar, A.; Madaria, A. R.; Zhou, C., Growth of aligned single-crystalline rutile TiO2 nanowires on arbitrary substrates and their application in dye-sensitized solar cells. *Journal of Physical Chemistry C* **2010,** *114* (17), 7787-7792.

121. Mor, G. K.; Shankar, K.; Paulose, M.; Varghese, O. K.; Grimes, C. A., Use of Highly-Ordered TiO2 Nanotube Arrays in Dye-Sensitized Solar Cells. *Nano Letters* **2005,** *6* (2), 215-218.

122. Mor, G. K.; Shankar, K.; Paulose, M.; Varghese, O. K.; Grimes, C. A., Enhanced photocleavage of water using titania nanotube arrays. *Nano Letters* **2005,** *5* (1), 191-195.

123. Dong, S.; Wang, H.; Gu, L.; Zhou, X.; Liu, Z.; Han, P.; Wang, Y.; Chen, X.; Cui, G.; Chen, L., Rutile TiO2 nanorod arrays directly grown on Ti foil substrates towards lithium-ion micro-batteries. *Thin Solid Films* **2011,** *519* (18), 5978-5982.

124. Wu, J. M.; Shih, H. C.; Wu, W. T., Electron field emission from single crystalline TiO2 nanowires prepared by thermal evaporation. *Chemical Physics Letters* **2005,** *413* (4-6), 490-494.

125. Yu, Y.; Xu, D., Single-crystalline TiO2 nanorods: Highly active and easily recycled photocatalysts. *Applied Catalysis B: Environmental* **2007,** *73* (1-2), 166-171.

126. Jennings, J. R.; Ghicov, A.; Peter, L. M.; Schmuki, P.; Walker, A. B., Dye-Sensitized Solar Cells Based on Oriented TiO2 Nanotube Arrays: Transport, Trapping, and Transfer of Electrons. *Journal of the American Chemical Society* **2008,** *130* (40), 13364-13372.

127. Chen, Q.; Xu, D., Large-Scale, Noncurling, and Free-Standing Crystallized TiO2 Nanotube Arrays for Dye-Sensitized Solar Cells. *The Journal of Physical Chemistry C* **2009,** *113* (15), 6310-6314.

128. Richter, C.; Schmuttenmaer, C. A. In *Photoconductivity in TiO2 nanotubes measured by time resolved terahertz spectroscopy*, Optics InfoBase Conference Papers, 2010.

129. Wehrenfennig, C.; Palumbiny, C. M.; Schmidt-Mende, L.; Johnston, M. B.; Snaith, H. J.; Herz, L. M. In *Fast electron trapping in anodized TiO2 nanotubes*, International Conference on Infrared, Millimeter, and Terahertz Waves, IRMMW-THz, 2013.

130. Carlson, H. J.; Campbell, R. E., Genetically encoded FRET-based biosensors for multiparameter fluorescence imaging. *Curr. Opin. Biotechnol.* **2009,** *20* (1), 19-27.

131. Hovan, S. C.; Howell, S.; Park, P. S. H., Forster resonance energy transfer as a tool to study photoreceptor biology. *J. Biomed. Opt.* **2010,** *15* (6), 9.

132. Laptenok, S. P.; Borst, J. W.; Mullen, K. M.; van Stokkum, I. H. M.; Visser, A.; van Amerongen, H., Global analysis of Forster resonance energy transfer in live cells measured by fluorescence lifetime imaging microscopy exploiting the rise time of acceptor fluorescence. *Physical Chemistry Chemical Physics* **2010,** *12* (27), 7593-7602.

133. Sidebert, S.; Kalinin, S.; Hien, N.; Kienzler, A.; Clima, L.; Bannwarth, W.; Appel, B.; Muller, S.; Seidel, C. A. M., Accurate Distance Determination of Nucleic Acids via Forster Resonance Energy Transfer: Implications of Dye Linker Length and Rigidity. *Journal of the American Chemical Society* **2011,** *133* (8), 2463-2480.

134. Mor, G. K.; Basham, J.; Paulose, M.; Kim, S.; Varghese, O. K.; Vaish, A.; Yoriya, S.; Grimes, C. A., High-Efficiency Forster Resonance Energy Transfer in Solid-State Dye Sensitized Solar Cells. *Nano Letters* **2010,** *10* (7), 2387-2394.

135. Basham, J. I.; Mor, G. K.; Grimes, C. A., Forster Resonance Energy Transfer in Dye-Sensitized Solar Cells. *ACS Nano* **2010,** *4* (3), 1253-1258.

136. Frigoli, M.; Ouadahi, K.; Larpent, C., A Cascade FRET-Mediated Ratiometric Sensor for Cu(2+)Ions Based on Dual Fluorescent Ligand-Coated Polymer Nanoparticles. *Chem.-Eur. J.* **2009,** *15* (33), 8319-8330.

137. Zhou, Z. G.; Yu, M. X.; Yang, H.; Huang, K. W.; Li, F. Y.; Yi, T.; Huang, C. H., FRET-based sensor for imaging chromium(III) in living cells. *Chem. Commun.* **2008,** (29), 3387-3389.

138. Yin, J.; Lin, A. J.; Buckett, P. D.; Wessling-Resnick, M.; Golan, D. E.; Walsh, C. T., Single-cell FRET imaging of transferrin receptor trafficking dynamics by Sfp-catalyzed, site-specific protein labeling. *Chem. Biol.* **2005,** *12* (9), 999-1006.

139. Ratner, V.; Kahana, E.; Eichler, M.; Haas, E., A general strategy for site-specific double labeling of globular proteins for kinetic FRET studies. *Bioconjugate Chem.* **2002,** *13* (5), 1163-1170.

140. Beljonne, D.; Curutchet, C.; Scholes, G. D.; Silbey, R. J., Beyond Forster Resonance Energy Transfer in Biological and Nanoscale Systems. *Journal of Physical Chemistry B* **2009,** *113* (19), 6583-6599.

141. Clapp, A. R.; Medintz, I. L.; Mauro, J. M.; Fisher, B. R.; Bawendi, M. G.; Mattoussi, H., Fluorescence Resonance Energy Transfer Between Quantum Dot Donors and Dye-Labeled Protein Acceptors. *Journal of the American Chemical Society* **2003,** *126* (1), 301-310.

142. Boker, A.; Lin, Y.; Chiapperini, K.; Horowitz, R.; Thompson, M.; Carreon, V.; Xu, T.; Abetz, C.; Skaff, H.; Dinsmore, A. D.; Emrick, T.; Russell, T. P., Hierarchical nanoparticle assemblies formed by decorating breath figures. *Nat. Mater.* **2004,** *3* (5), 302-306.

143. Fan, W.; Snyder, M. A.; Kumar, S.; Lee, P. S.; Yoo, W. C.; McCormick, A. V.; Penn, R. L.; Stein, A.; Tsapatsis, M., Hierarchical nanofabrication of microporous crystals with ordered mesoporosity. *Nat. Mater.* **2008,** *7* (12), 984-991.

144. Na, K.; Jo, C.; Kim, J.; Cho, K.; Jung, J.; Seo, Y.; Messinger, R. J.; Chmelka, B. F.; Ryoo, R., Directing Zeolite Structures into Hierarchically Nanoporous Architectures. *Science* **2011,** *333* (6040), 328-332.

145. Bein, T., Zeolitic host-guest interactions and building blocks for the self-assembly of complex materials. *MRS Bull.* **2005,** *30* (10), 713-720.

146. Devaux, A.; Lutkouskaya, K.; Calzaferri, G.; Dieu, L. Q.; Bruhwiler, D.; De Cola, L.; Torres, T., Nanochannels for supramolecular organisation of dyes. *Chimia* **2007,** *61* (10), 626-630.

147. Shankar, K.; Feng, X.; Grimes, C. A., Enhanced harvesting of red photons in nanowire solar cells: Evidence of resonance energy transfer. *ACS Nano* **2009,** *3* (4), 788-794.

148. Zhang, G. Q.; Finefrock, S.; Liang, D. X.; Yadav, G. G.; Yang, H. R.; Fang, H. Y.; Wu, Y., Semiconductor nanostructure-based photovoltaic solar cells. *Nanoscale* **2011,** *3* (6), 2430-2443.

149. El-Kouedi, M.; Foss, C. A., Optical properties of gold-silver iodide nanoparticle pair structures. *J. Phys. Chem. B* **2000,** *104* (17), 4031-4037.

150. Chung, A. J.; Huh, Y. S.; Erickson, D., Large area flexible SERS active substrates using engineered nanostructures. *Nanoscale* **2011,** *3* (7), 2903-2908.

151. Miura, I.; Okada, Y.; Kudoh, S.; Nakata, M., Organic electroluminescence in porous alumina. *Jpn. J. Appl. Phys. Part 1 - Regul. Pap. Short Notes Rev. Pap.* **2004,** *43* (11A), 7552-7553.

152. Yagi, K.; Shibata, S.; Yano, T.; Yasumori, A.; Yamane, M.; Dunn, B., Photostability of the laser dye DCM in various inorganic-organic host matrices. *Journal of Sol-Gel Science and Technology* **1995,** *4* (1), 67-73.

153. Blum, C.; Vos, W. L.; Subramaniam, V., Tuning Spontaneous Emission versus Forster Energy Transfer in Biological Systems by Manipulating the Density of Photonic States. *arXiv:0704.3560v2 [physics.chem-ph]* **2007**.

154. Mor, G. K.; Kim, S.; Paulose, M.; Varghese, O. K.; Shankar, K.; Basham, J.; Grimes, C. A., Visible to near-infrared light harvesting in TiO2 nanotube array-P3HT based heterojunction solar cells. *Nano Letters* **2009,** *9* (12), 4250-4257.

155. Buhbut, S.; Itzhakov, S.; Tauber, E.; Shalom, M.; Hod, I.; Geiger, T.; Garini, Y.; Oron, D.; Zaban, A., Built-in Quantum Dot Antennas in Dye-Sensitized Solar Cells. *ACS Nano* **2010,** *4* (3), 1293-1298.

156. Buhbut, S.; Itzhakov, S.; Oron, D.; Zaban, A., Quantum Dot Antennas for Photoelectrochemical Solar Cells. *The Journal of Physical Chemistry Letters* **2011,** *2* (15), 1917-1924.

157. Wallrabe, H.; Periasamy, A., Imaging protein molecules using FRET and FLIM microscopy. *Current Opinion in Biotechnology* **2005,** *16* (1), 19-27.

158. Majoul, I.; Straub, M.; Duden, R.; Hell, S. W.; SÃ¶ling, H.-D., Fluorescence resonance energy transfer analysis of proteinâ€“protein interactions in single living cells by multifocal multiphoton microscopy. *Reviews in Molecular Biotechnology* **2002,** *82* (3), 267-277.

159. LleÃ³, A.; Berezovska, O.; Herl, L.; Raju, S.; Deng, A.; Bacskai, B. J.; Frosch, M. P.; Irizarry, M.; Hyman, B. T., Nonsteroidal anti-inflammatory drugs lower AÎ²42 and change presenilin 1 conformation. *Nature Medicine* **2004,** *10* (10), 1065-1066.

160. Huang, G. S.; Wu, X. L.; Xie, Y.; Kong, F.; Zhang, Z. Y.; Siu, G. G.; Chu, P. K., Photoluminescence from 8-hydroxy quinoline aluminum embedded in porous anodic alumina membrane. *Applied Physics Letters* **2005,** *87* (15).

161. Berger, S.; Kunze, J.; Schmuki, P.; Valota, A. T.; Leclere, D. J.; Skeldon, P.; Thompson, G. E., Influence of water content on the growth of anodic TiO2 nanotubes in fluoride-containing ethylene glycol electrolytes. *Journal of the Electrochemical Society* **2010,** *157* (1), C18-C23.

162. Roy, P.; Berger, S.; Schmuki, P., TiO2 nanotubes: Synthesis and applications. *Angewandte Chemie - International Edition* **2011,** *50* (13), 2904-2939.

163. Shankar, K.; Basham, J. I.; Allam, N. K.; Varghese, O. K.; Mor, G. K.; Feng, X.; Paulose, M.; Seabold, J. A.; Choi, K.-S.; Grimes, C. A., Recent Advances in the Use of TiO2 Nanotube and Nanowire Arrays for Oxidative Photoelectrochemistry. *The Journal of Physical Chemistry C* **2009,** *113* (16), 6327-6359.

164. Lei, B.-X.; Liao, J.-Y.; Zhang, R.; Wang, J.; Su, C.-Y.; Kuang, D.-B., Ordered Crystalline TiO2 Nanotube Arrays on Transparent FTO Glass for Efficient Dye-Sensitized Solar Cells. *The Journal of Physical Chemistry C* **2010,** *114* (35), 15228-15233.

165. Chen, C.-C.; Chung, H.-W.; Chen, C.-H.; Lu, H.-P.; Lan, C.-M.; Chen, S.-F.; Luo, L.; Hung, C.-S.; Diau, E. W.-G., Fabrication and Characterization of Anodic Titanium Oxide Nanotube Arrays of Controlled Length for Highly Efficient Dye-Sensitized Solar Cells. *The Journal of Physical Chemistry C* **2008,** *112* (48), 19151-19157.

166. Wu, D.; Liu, J.; Zhao, X.; Li, A.; Chen, Y.; Ming, N., Sequence of Events for the Formation of Titanate Nanotubes, Nanofibers, Nanowires, and Nanobelts. *Chemistry of Materials* **2005,** *18* (2), 547-553.

167. Lei, Y.; Zhang, L. D., Fabrication, characterization, and photoluminescence properties of highly ordered TiO2 nanowire arrays. *Journal of Materials Research* **2001,** *16* (04), 1138-1144.

168. Kumar, A.; Madaria, A. R.; Zhou, C., Growth of Aligned Single-Crystalline Rutile TiO2 Nanowires on Arbitrary Substrates and Their Application in Dye-Sensitized Solar Cells. *The Journal of Physical Chemistry C* **2010,** *114* (17), 7787-7792.

169. Shin, Y.; Lee, S., Self-Organized Regular Arrays of Anodic TiO2 Nanotubes. *Nano Letters* **2008,** *8* (10), 3171-3173.

170. Liu, B.; Boercker, J. E.; Aydil, E. S., Oriented single crystalline titanium dioxide nanowires. *Nanotechnology* **2008,** *19* (50), 505604.

171. Demazeau, G., Solvothermal and hydrothermal processes: the main physico-chemical factors involved and new trends. *Research on Chemical Intermediates* **2011,** *37* (2-5), 107-123.

172. Demazeau, G., Solvothermal reactions: an original route for the synthesis of novel materials. *J. Mater. Sci.* **2008,** *43* (7), 2104-2114.

173. Demazeau, G., Impact of High Pressures in Solvothermal Processes. In *International Conference on High Pressure Science and Technology, Joint Airapt-22 and Hpcj-50*, Takemura, K., Ed. Iop Publishing Ltd: Bristol, 2010; Vol. 215.

174. Li, S.; Zhang, G.; Guo, D.; Yu, L.; Zhang, W., Anodization Fabrication of Highly Ordered TiO2 Nanotubes. *The Journal of Physical Chemistry C* **2009,** *113* (29), 12759-12765.

175. Zamuner, M.; Talaga, D.; Deiss, F.; Guieu, V.; Kuhn, A.; Ugo, P.; Sojic, N., Fabrication of a Macroporous Microwell Array for Surface-Enhanced Raman Scattering. *Advanced Functional Materials* **2009,** *19* (19), 3129-3135.

176. Semouchkina, E. A.; Semouchkin, G. B.; Lanagan, M.; Randall, C. A., FDTD study of resonance Processes in metamaterials. *Microwave Theory and Techniques, IEEE Transactions on* **2005,** *53* (4), 1477-1487.

177. Sergentu, V. V.; Tiginyanu, I. M.; Ursaki, V. V.; Enachi, M.; Albu, S. P.; Schmuki, P., Prediction of negative index material lenses based on metallo-dielectric nanotubes. *physica status solidi (RRL) – Rapid Research Letters* **2008,** *2* (5), 242-244.

178. Macak, J. M.; Hildebrand, H.; Marten-Jahns, U.; Schmuki, P., Mechanistic aspects and growth of large diameter self-organized TiO2 nanotubes. *Journal of Electroanalytical Chemistry* **2008,** *621* (2), 254-266.

179. Shankar, K.; Mor, G. K.; Fitzgerald, A.; Grimes, C. A., Cation Effect on the Electrochemical Formation of Very High Aspect Ratio TiO2 Nanotube Arrays in Formamideâˆ'Water Mixtures. *The Journal of Physical Chemistry C* **2006,** *111* (1), 21-26.

180. Shankar, K. Effect of Architecture and Doping on the Photoelectrochemical Properties of Titania Nanotubes. The Pennsylvania State University University Park, 2007.

181. Ue, M.; Mizutani, F.; Takaha, H.; Takeuchi, S.; Sugiyama, K.; Nishiwaki, T.; Sato, N., Anodization of Alâ€"Nd alloy films in nonaqueous electrolyte solutions for TFT-LCD application. *Electrochimica Acta* **2001,** *47* (1â€"2), 217-223.

182. Kane, Y., Numerical solution of initial boundary value problems involving maxwell's equations in isotropic media. *Antennas and Propagation, IEEE Transactions on* **1966,** *14* (3), 302-307.

183. Ong, K. G.; Varghese, O. K.; Mor, G. K.; Grimes, C. A., Numerical Simulation of Light Propagation Through Highly-Ordered Titania Nanotube Arrays: Dimension Optimization for Improved Photoabsorption. *Journal of Nanoscience and Nanotechnology* **2005,** *5* (11), 1801-1808.

184. Ong, K. G.; Varghese, O. K.; Mor, G. K.; Shankar, K.; Grimes, C. A., Application of finite-difference time domain to dye-sensitized solar cells: The effect of nanotube-array negative electrode dimensions on light absorption. *Solar Energy Materials and Solar Cells* **2007,** *91* (4), 250-257.

185. Fischer, L.; Zvyagin, A.; Plakhotnik, T.; Vorobyev, M., Numerical modeling of light propagation in a hexagonal array of dielectric cylinders. *Journal of the Optical Society of America A: Optics and Image Science, and Vision* **2010,** *27* (4), 865-872.

186. Song, Y.-Y.; Schmidt-Stein, F.; Bauer, S.; Schmuki, P., Amphiphilic TiO2 Nanotube Arrays: An Actively Controllable Drug Delivery System. *Journal of the American Chemical Society* **2009,** *131* (12), 4230-4232.

187. Mohapatra, S. K.; Banerjee, S.; Misra, M., Synthesis of Fe2O3/TiO2 nanorod-nanotube arrays by filling TiO2 nanotubes with Fe. *Nanotechnology* **2008,** *19* (31).

188. Meng, G.; Jung, Y. J.; Cao, A.; Vajtai, R.; Ajayan, P. M., Controlled fabrication of hierarchically branched nanopores, nanotubes, and nanowires. *Proceedings of the National Academy of Sciences of the United States of America* **2005,** *102* (20), 7074-7078.

189. Zhang, Q.; Fan, W.; Gao, L., Anatase TiO2 nanoparticles immobilized on ZnO tetrapods as a highly efficient and easily recyclable photocatalyst. *Applied Catalysis B: Environmental* **2007,** *76* (1-2), 168-173.

190. Hsu, Y. F.; Yip, C. T.; DjuriÅ¡iÄ‡, A. B.; Chan, W. K. In *Efficiency enhancement for ZnO tetrapod dye-sensitized solar cells by TiO2 coating and ammonium treatment*, 2008 2nd IEEE International Nanoelectronics Conference, INEC 2008, 2008; pp 358-361.

191. Waghmare, P. R.; Mitra, S. K., Contact angle hysteresis of microbead suspensions. *Langmuir* **2010,** *26* (22), 17082-17089.

192. Mohammadpour, A.; Shankar, K., Anodic TiO2 nanotube arrays with optical wavelength-sized apertures. *Journal of Materials Chemistry* **2010,** *20* (39), 8474-8477.

193. Yoriya, S.; Mor, G. K.; Sharma, S.; Grimes, C. A., Synthesis of ordered arrays of discrete, partially crystalline titania nanotubes by Ti anodization using diethylene glycol electrolytes. *Journal of Materials Chemistry* **2008,** *18* (28), 3332-3336.

194. Yasuda, K.; MacAk, J. M.; Berger, S.; Ghicov, A.; Schmuki, P., Mechanistic aspects of the self-organization process for oxide nanotube formation on valve metals. *Journal of the Electrochemical Society* **2007,** *154* (9), C472-C478.

195. Sivaprasad, P.; Kalidas, C., Conductance behaviour of HCl in water-ethylene glycol, water-diethylene glycol and ethylene glycol-diethylene glycol mixtures. *Proceedings of the Indian Academy of Sciences - Chemical Sciences* **1983,** *92* (3), 203-209.

196. Izutsu, K., *Electrochemistry in Nonaqueous Solutions*. 2003.

197. Macak, J. M.; Schmuki, P., Anodic growth of self-organized anodic TiO2 nanotubes in viscous electrolytes. *Electrochimica Acta* **2006,** *52* (3), 1258-1264.

198. Sun, L.; Zhang, S.; Sun, X. W.; He, X., Effect of electric field strength on the length of anodized titania nanotube arrays. *Journal of Electroanalytical Chemistry* **2009,** *637* (1-2), 6-12.

199. Sreekantan, S.; Saharudin, K. A.; Lockman, Z.; Tzu, T. W., Fast-rate formation of TiO2 nanotube arrays in an organic bath and their applications in photocatalysis. *Nanotechnology* **2010,** *21* (36).

200. Prakasam, H. E.; Shankar, K.; Paulose, M.; Varghese, O. K.; Grimes, C. A., A new benchmark for TiO 2 nanotube array growth by anodization. *Journal of Physical Chemistry C* **2007,** *111* (20), 7235-7241.

201. Rao, S. V.; Kalidas, C., Effect of water on the conductance of hydrogen halides in diethylene glycol. *Bull. Chem. Soc. Jpn.* **1976,** *49*, 203-2-5.

202. Zhu, K.; Vinzant, T. B.; Neale, N. R.; Frank, A. J., Removing structural disorder from oriented TiO2 nanotube arrays: Reducing the dimensionality of transport and recombination in dye-sensitized solar cells. *Nano Letters* **2007,** *7* (12), 3739-3746.

203. Roy, P.; Dey, T.; Schmuki, P., Scanning electron microscopy observation of nanoscopic wetting of TiO 2 nanotubes and ODS modified nanotubes using ionic liquids. *Electrochemical and Solid-State Letters* **2010,** *13* (7), E11-E13.

204. Hoang, V. V., The glass transition and thermodynamics of liquid and amorphous TiO 2 nanoparticles. *Nanotechnology* **2008,** *19* (10).

205. Stukan, M. R.; Ligneul, P.; Crawshaw, J. P.; Boek, E. S., Spontaneous imbibition in nanopores of different roughness and wettability. *Langmuir* **2010,** *26* (16), 13342-13352.

206. Pinzari, F.; Ascarelli, P.; Cappelli, E.; Mattei, G.; Giorgi, R., Wettability of HF-CVD diamond films. *Diamond and Related Materials* **2001,** *10* (3-7), 781-785.

207. Kim, D.; Macak, J. M.; Schimidt-Stein, F.; Schmuki, P., Capillary effects, wetting behavior and photo-induced tube filling of TiO2 nanotube layers. *Nanotechnology* **2008,** *19* (30).

208. Li, J.; Papadopoulos, C.; Xu, J., Growing Y-junction carbon nanotubes. *Nature* **1999,** *402* (6759), 253-254.

209. Mohapatra, S. K.; Misra, M.; Mahajan, V. K.; Raja, K. S., Synthesis of Y-branched TiO2 nanotubes. *Materials Letters* **2008,** *62* (12-13), 1772-1774.

210. Xu, C. X.; Xue, Q. H.; Zhong, Y.; Cui, Y. P.; Ba, L.; Zhao, B.; Gu, N., Photoluminescent blue-shift of organic molecules in nanometre pores. *Nanotechnology* **2002,** *13* (1), 47-50.

211. Das, L.; Mateo, J.; Bandyopadhyay, S.; Edwards, J. D.; Anderson, J., Motional modes in bulk powder and few-molecule clusters of tris(8-hydroxyquinoline aluminum) and their relation to spin dephasing. *Applied Physics Letters* **2011,** *98* (6).

212. Kanchibotla, B.; Pramanik, S.; Bandyopadhyay, S.; Cahay, M., Transverse spin relaxation time in organic molecules. *Physical Review B* **2008,** *78* (19).

213. Blum, C.; Vos, W. L.; Vinod Subramaniam, V., Tuning Spontaneous Emission versus Forster Energy Transfer in Biological Systems by Manipulating the Density of Photonic States. *arXiv:0704.3560 [physics.chem-ph]* **2007**.

214. Davis, S. A.; Burkett, S. L.; Mendelson, N. H.; Mann, S., Bacterial templating of ordered macrostructures in silica and silica- surfactant mesophases. *Nature* **1997,** *385* (6615), 420-423.

215. Forster, T., 10th Spiers Memorial Lecture - Transfer Mechanisms of Electronic Excitation. *Discussions of the Faraday Society* **1959,** (27), 7-17.

216. Meng, G.; Cao, A.; Cheng, J.-Y.; Vijayaraghavan, A.; Jung, Y. J.; Shima, M.; Ajayan, P. M., Ordered Ni nanowire tip arrays sticking out of the anodic aluminum oxide template. *Journal of Applied Physics* **2005,** *97* (6), -.

217. Li, Y.; Meng, G. W.; Zhang, L. D.; Phillipp, F., Ordered semiconductor ZnO nanowire arrays and their photoluminescence properties. *Applied Physics Letters* **2000,** *76* (15), 2011-2013.

218. Routkevitch, D.; Bigioni, T.; Moskovits, M.; Xu, J. M., Electrochemical Fabrication of CdS Nanowire Arrays in Porous Anodic Aluminum Oxide Templates. *The Journal of Physical Chemistry* **1996,** *100* (33), 14037-14047.

219. Xu, D.; Shi, X.; Guo, G.; Gui, L.; Tang, Y., Electrochemical Preparation of CdSe Nanowire Arrays. *The Journal of Physical Chemistry B* **2000,** *104* (21), 5061-5063.

220. Peng, Y.; Zhang, H.-L.; Pan, S.-L.; Li, H.-L., Magnetic properties and magnetization reversal of Î±-Fe nanowires deposited in alumina film. *Journal of Applied Physics* **2000,** *87* (10), 7405-7408.

221. Zeng, H.; Zheng, M.; Skomski, R.; Sellmyer, D. J.; Liu, Y.; Menon, L.; Bandyopadhyay, S., Magnetic properties of self-assembled Co nanowires of varying length and diameter. *Journal of Applied Physics* **2000,** *87* (9), 4718-4720.

222. Choi, J.; Sauer, G.; Nielsch, K.; Wehrspohn, R. B.; GÃ¶sele, U., Hexagonally Arranged Monodisperse Silver Nanowires with Adjustable Diameter and High Aspect Ratio. *Chemistry of Materials* **2003,** *15* (3), 776-779.

223. Sander, M. S.; Gronsky, R.; Sands, T.; Stacy, A. M., Structure of Bismuth Telluride Nanowire Arrays Fabricated by Electrodeposition into Porous Anodic Alumina Templates. *Chemistry of Materials* **2002,** *15* (1), 335-339.

224. Yin, A. J.; Li, J.; Jian, W.; Bennett, A. J.; Xu, J. M., Fabrication of highly ordered metallic nanowire arrays by electrodeposition. *Applied Physics Letters* **2001,** *79* (7), 1039-1041.

225. Evans, P. R.; Yi, G.; Schwarzacher, W., Current perpendicular to plane giant magnetoresistance of multilayered nanowires electrodeposited in anodic aluminum oxide membranes. *Applied Physics Letters* **2000,** *76* (4), 481-483.

226. Hu, W.; Gong, D.; Chen, Z.; Yuan, L.; Saito, K.; Grimes, C. A.; Kichambare, P., Growth of well-aligned carbon nanotube arrays on silicon substrates using porous alumina film as a nanotemplate. *Applied Physics Letters* **2001,** *79* (19), 3083-3085.

227. Guo, Y. G.; Hu, J. S.; Liang, H. P.; Wan, L. J.; Bai, C. L., TiO2-Based Composite Nanotube Arrays Prepared via Layer-by-Layer Assembly. *Advanced Functional Materials* **2005,** *15* (2), 196-202.

228. Wang, W.; Li, N.; Li, X.; Geng, W.; Qiu, S., Synthesis of metallic nanotube arrays in porous anodic aluminum oxide template through electroless deposition. *Materials Research Bulletin* **2006,** *41* (8), 1417-1423.

229. Hassanzadeh, N.; Omidvar, H.; Poorbafrani, M.; Tabaian, S., Influence of Anodizing Parameters on Pore Diameter of Anodic Aluminium Oxide (AAO) Films Using Taguchi Design. *Arabian Journal for Science and Engineering* **2013,** *38* (6), 1305-1312.

230. Tian, M.; Xu, S.; Wang, J.; Kumar, N.; Wertz, E.; Li, Q.; Campbell, P. M.; Chan, M. H. W.; Mallouk, T. E., Penetrating the Oxide Barrier in Situ and Separating Freestanding Porous Anodic Alumina Films in One Step. *Nano Letters* **2005,** *5* (4), 697-703.

231. Shimizu, T.; Xie, T.; Nishikawa, J.; Shingubara, S.; Senz, S.; Gösele, U., Synthesis of Vertical High-Density Epitaxial Si(100) Nanowire Arrays on a Si(100) Substrate Using an Anodic Aluminum Oxide Template. *Advanced Materials* **2007,** *19* (7), 917-920.

232. Liu, S.; Xiong, Z.; Zhu, C.; Li, M.; Zheng, M.; Shen, W., Fast anodization fabrication of AAO and barrier perforation process on ITO glass. *Nanoscale Research Letters C7 - 159* **2014,** *9* (1), 1-8.

233. Han, C. Y.; Willing, G. A.; Xiao, Z.; Wang, H. H., Control of the Anodic Aluminum Oxide Barrier Layer Opening Process by Wet Chemical Etching. *Langmuir* **2006,** *23* (3), 1564-1568.

234. Le Coz, F.; Arurault, L.; Fontorbes, S.; Vilar, V.; Datas, L.; Winterton, P., Chemical composition and structural changes of porous templates obtained by anodising aluminium in phosphoric acid electrolyte. *Surface and Interface Analysis* **2010,** *42* (4), 227-233.

235. Lee, W.; Nielsch, K.; GÃ¶sele, U., Self-ordering behavior of nanoporous anodic aluminum oxide (AAO) in malonic acid anodization. *Nanotechnology* **2007,** *18* (47), 475713.

236. Wang, J.; Wang, C.-W.; Li, S.-Y.; Zhou, F., The effect of oxalic and sulfuric ions on the photoluminescence ofÂ anodic aluminum oxide formed in a mixture of sulfuric andÂ oxalic acid. *Applied Physics A* **2009,** *94* (4), 939-942.

237. Oh, J.; Thompson, C. V., The role of electric field in pore formation during aluminum anodization. *Electrochimica Acta* **2011,** *56* (11), 4044-4051.

238. Lee, K. H.; Wong, C. C., Decoupling two-step anodization in anodic aluminum oxide. *Journal of Applied Physics* **2009,** *106* (10), -.

239. Alam, K. M.; Singh, A. P.; Bodepudi, S. C.; Pramanik, S., Fabrication of hexagonally ordered nanopores in anodic alumina: An alternative pretreatment. *Surf. Sci.* **2011,** *605* (3-4), 441-449.

240. Ono, S.; Saito, M.; Ishiguro, M.; Asoh, H., Controlling factor of self-ordering of anodic porous alumina. *Journal of the Electrochemical Society* **2004,** *151* (8), B473-B478.

241. Ishiji, T.; Kaneko, M., Photoluminescence of pyrenebutyric acid incorporated into silicone film as a technique in luminescent oxygen sensing. *Analyst* **1995,** *120* (6), 1633-1638.

242. Baldacchini, G.; Chiacchiaretta, P.; Reisfeld, R.; Zigansky, E., The origin of luminescence blueshifts in Alq(3) composites. *J. Lumines.* **2009,** *129* (12), 1849-1852.

243. Levichkova, M. M.; Assa, J. J.; Frob, H.; Leo, K., Blue luminescent isolated Alq(3) molecules in a solid-state matrix. *Applied Physics Letters* **2006,** *88* (20).

244. Muccini, M.; Loi, M. A.; Kenevey, K.; Zamboni, R.; Masciocchi, N.; Sironi, A., Blue Luminescence of Facial Tris(quinolin-8-olato)aluminum(III) in Solution, Crystals, and Thin Films. *Advanced Materials* **2004,** *16* (11), 861-864.

245. Hennecke, M.; Wadle, A., A photoselection study on the fluorescence of pyrenebutyric acid in solution. *The Journal of Chemical Physics* **1992,** *97* (2), 871-874.

246. Flink, S.; van Veggel, F.; Reinhoudt, D. N., Functionalization of self-assembled monolayers on glass and oxidized silicon wafers by surface reactions. *J. Phys. Org. Chem.* **2001,** *14* (7), 407-415.

247. Sluch, M. I.; Vitukhnovsky, A. G.; Petty, M. C., Pyrene excimer formation in Langmuir-Blodgett films. *Thin Solid Films* **1996,** *284-285* (0), 622-626.

248. Bauer, R. K.; De Mayo, P.; Ware, W. R.; Wu, K. C., Surface photochemistry. The photophysics of pyrene adsorbed on silica gel, alumina, and calcium fluoride. *The Journal of Physical Chemistry* **1982,** *86* (19), 3781-3789.

249. Thangaraju, K.; Kumar, J.; Amaladass, P.; Mohanakrishnan, A. K.; Narayanan, V., Study on photoluminescence from tris-(8-hydroxyquinoline)aluminum thin films and influence of light. *Applied Physics Letters* **2006,** *89* (8), 082106-3.

250. Shankar, K.; Mor, G. K.; Prakasam, H. E.; Varghese, O. K.; Grimes, C. A., Self-Assembled Hybrid Polymerâˆ’TiO2 Nanotube Array Heterojunction Solar Cells. *Langmuir* **2007,** *23* (24), 12445-12449.

251. Yang, P.; Zhou, X.; Cao, G.; Luscombe, C. K., P3HT:PCBM polymer solar cells with TiO2 nanotube aggregates in the active layer. *Journal of Materials Chemistry* **2010,** *20* (13), 2612-2616.

252. Mor, G. K.; Kim, S.; Paulose, M.; Varghese, O. K.; Shankar, K.; Basham, J.; Grimes, C. A., Visible to Near-Infrared Light Harvesting in TiO2 Nanotube Arrayâˆ’P3HT Based Heterojunction Solar Cells. *Nano Letters* **2009,** *9* (12), 4250-4257.

253. KuÅ¾elovÃ¡, K.; GrebeÅˆovÃ¡, D.; Hrkal, Z., Labeling of apoptotic JURL-MK1 cells by fluorescent caspase-3 inhibitor FAM-DEVD-fmk occurs mainly at site(s) different from caspase-3 active site. *Cytometry Part A* **2007,** *71* (8), 605-611.

254. Saberi Moghaddam, R.; Huettner, S.; Vaynzof, Y.; Ducati, C.; Divitini, G.; Lohwasser, R. H.; Musselman, K. P.; Sepe, A.; Scherer, M. R. J.; Thelakkat, M.; Steiner, U.; Friend, R. H., Polymer crystallization as a tool to pattern hybrid nanostructures: Growth of 12 nm ZnO arrays in poly(3-hexylthiophene). *Nano Letters* **2013,** *13* (9), 4499-4504.

255. Motaung, D. E.; Malgas, G. F.; Arendse, C. J.; Mavundla, S. E., Determination of the structure, morphology and complex refractive index in ZnO-nanopencils/P3HT hybrid structures. *Materials Chemistry and Physics* **2012,** *135* (2-3), 401-410.

256. Bidmanova, S.; Hlavacek, A.; Damborsky, J.; Prokop, Z., Conjugation of 5(6)-carboxyfluorescein and 5(6)-carboxynaphthofluorescein with bovine serum albumin and their immobilization for optical pH sensing. *Sensors and Actuators, B: Chemical* **2012,** *161* (1), 93-99.

257. Cook, S.; Furube, A.; Katoh, R., Analysis of the excited states of regioregular polythiophene P3HT. *Energy and Environmental Science* **2008,** *1* (2), 294-299.

258. Kvach, M. V.; Tsybulsky, D. A.; Ustinov, A. V.; Stepanova, I. A.; Bondarev, S. L.; Gontarev, S. V.; Korshun, V. A.; Shmanai, V. V., 5(6)-Carboxyfluorescein revisited: New protecting group, separation of isomers, and their spectral properties on oligonucleotides. *Bioconjugate Chemistry* **2007,** *18* (5), 1691-1696.

259. Xu, C.; Shin, P. H.; Cao, L.; Wu, J.; Gao, D., Ordered TiO2 nanotube arrays on transparent conductive oxide for dye-sensitized solar cells. *Chemistry of Materials* **2010,** *22* (1), 143-148.

260. Zhu, K.; Neale, N. R.; Miedaner, A.; Frank, A. J., Enhanced charge-collection efficiencies and light scattering in dye-sensitized solar cells using oriented TiO2 nanotubes arrays. *Nano Letters* **2007,** *7* (1), 69-74.

261. Albu, S. P.; Ghicov, A.; Macak, J. M.; Hahn, R.; Schmuki, P., Self-organized, free-standing TiO2 nanotube membrane for flow-through photocatalytic applications. *Nano Letters* **2007,** *7* (5), 1286-1289.

262. Wu, Z.; Dong, F.; Zhao, W.; Wang, H.; Liu, Y.; Guan, B., The fabrication and characterization of novel carbon doped TiO2 nanotubes, nanowires and nanorods with high visible light photocatalytic activity. *Nanotechnology* **2009,** *20* (23).

263. Liu, G.; Li, F.; Wang, D. W.; Tang, D. M.; Liu, C.; Ma, X.; Lu, G. Q.; Cheng, H. M., Electron field emission of a nitrogen-doped TiO2 nanotube array. *Nanotechnology* **2008,** *19* (2).

264. Xiang, B.; Zhang, Y.; Wang, Z.; Luo, X. H.; Zhu, Y. W.; Zhang, H. Z.; Yu, D. P., Field-emission properties of TiO2 nanowire arrays. *Journal of Physics D: Applied Physics* **2005,** *38* (8), 1152-1155.

265. Xu, J.; Jia, C.; Cao, B.; Zhang, W. F., Electrochemical properties of anatase TiO2 nanotubes as an anode material for lithium-ion batteries. *Electrochimica Acta* **2007,** *52* (28), 8044-8047.

266. Armstrong, G.; Armstrong, A. R.; Bruce, P. G.; Reale, P.; Scrosati, B., TiO2(B) nanowires as an improved anode material for lithium-ion batteries containing LiFePO4 or LiNi0.5Mn 1.5O4 cathodes and a polymer electrolyte. *Advanced Materials* **2006,** *18* (19), 2597-2600.

267. Many, A.; Rakavy, G., Theory of Transient Space-Charge-Limited Currents in Solids in the Presence of Trapping. *Physical Review* **1962,** *126* (6), 1980-1988.

268. Parker, R. A., Static Dielectric Constant of Rutile (TiO2), 1.6-1060°K. *Physical Review* **1961,** *124* (6), 1719-1722.

269. Dou, M.; Persson, C., Comparative study of rutile and anatase SnO2 and TiO 2: Band-edge structures, dielectric functions, and polaron effects. *Journal of Applied Physics* **2013,** *113* (8).

270. Katayama, M.; Ikesaka, S.; Kuwano, J.; Yamamoto, Y.; Koinuma, H.; Matsumoto, Y., Field-effect transistor based on atomically flat rutile TiO2. *Applied Physics Letters* **2006,** *89* (24).

271. Hendry, E.; Koeberg, M.; Pijpers, J.; Bonn, M., Reduction of carrier mobility in semiconductors caused by charge-charge interactions. *Physical Review B* **2007,** *75* (23), 233202.

272. Seitz, M. A.; Wmtmore, D. H., Electronic drift mobilities and space-charge-limited currents in lithium-doped zinc oxide. *Journal of Physics and Chemistry of Solids* **1968,** *29* (6), 1033-1049.

273. Breckenridge, R. G.; Hosler, W. R., Electrical Properties of Titanium Dioxide Semiconductors. *Physical Review* **1953,** *91* (4), 793-802.

274. Feng, X.; Zhu, K.; Frank, A. J.; Grimes, C. A.; Mallouk, T. E., Rapid Charge Transport in Dye-Sensitized Solar Cells Made from Vertically Aligned Single-Crystal Rutile TiO2 Nanowires. *Angewandte Chemie* **2012,** *124* (11), 2781-2784.

275. Enache-Pommer, E.; Liu, B.; Aydil, E. S., Electron transport and recombination in dye-sensitized solar cells made from single-crystal rutile TiO2 nanowires. *Physical Chemistry Chemical Physics* **2009,** *11* (42), 9648-9652.

276. Turner, G. M.; Beard, M. C.; Schmuttenmaer, C. A., Carrier Localization and Cooling in Dye-Sensitized Nanocrystalline Titanium Dioxide. *The Journal of Physical Chemistry B* **2002,** *106* (45), 11716-11719.

277. Yoriya, S.; Grimes, C. A., Self-Assembled TiO2 Nanotube Arrays by Anodization of Titanium in Diethylene Glycol: Approach to Extended Pore Widening. *Langmuir* **2010,** *26* (1), 417-420.

278. Albu, S. P.; Schmuki, P., TiO2 nanotubes grown in different organic electrolytes: Two-size self-organization, single vs. double-walled tubes, and giant diameters. *Phys. Status Solidi-Rapid Res. Lett.* **2010,** *4* (8-9), 215-217.

279. Mohammadpour, A.; Waghmare, P. R.; Mitra, S. K.; Shankar, K., Anodic Growth of Large-Diameter Multipodal TiO(2) Nanotubes. *Acs Nano* **2010,** *4* (12), 7421-7430.

280. Chen, B.; Lu, K., Hierarchically Branched Titania Nanotubes with Tailored Diameters and Branch Numbers. *Langmuir* **2012,** *28* (5), 2937-2943.

281. Zhang, X. J.; Han, F.; Shi, B.; Farsinezhad, S.; Dechaine, G. P.; Shankar, K., Photocatalytic Conversion of Diluted CO2 into Light Hydrocarbons Using Periodically Modulated Multiwalled Nanotube Arrays. *Angewandte Chemie-International Edition* **2012,** *51* (51), 12732-12735.

282. Yip, C. T.; Huang, H. T.; Zhou, L. M.; Xie, K. Y.; Wang, Y.; Feng, T. H.; Li, J. S.; Tam, W. Y., Direct and Seamless Coupling of TiO2 Nanotube Photonic Crystal to Dye-Sensitized Solar Cell: A Single-Step Approach. *Advanced Materials* **2011,** *23* (47), 5624-+.

283. Lin, J.; Liu, K.; Chen, X. F., Synthesis of Periodically Structured Titania Nanotube Films and Their Potential for Photonic Applications. *Small* **2011,** *7* (13), 1784-1789.

284. Stergiopoulos, T.; Ghicov, A.; Likodimos, V.; Tsoukleris, D. S.; Kunze, J.; Schmuki, P.; Falaras, P., Dye-sensitized solar cells based on thick highly ordered TiO(2) nanotubes produced by controlled anodic oxidation in non-aqueous electrolytic media. *Nanotechnology* **2008,** *19* (23), 7.

285. Vomiero, A.; Galstyan, V.; Braga, A.; Concina, I.; Brisotto, M.; Bontempi, E.; Sberveglieri, G., Flexible dye sensitized solar cells using TiO2 nanotubes. *Energy & Environmental Science* **2011,** *4* (9), 3408-3413.

286. Chen, B.; Hou, J. B.; Lu, K., Formation Mechanism of TiO2 Nanotubes and Their Applications in Photoelectrochemical Water Splitting and Supercapacitors. *Langmuir* **2013,** *29* (19), 5911-5919.

287. Lu, X. H.; Wang, G. M.; Zhai, T.; Yu, M. H.; Gan, J. Y.; Tong, Y. X.; Li, Y., Hydrogenated TiO2 Nanotube Arrays for Supercapacitors. *Nano Lett.* **2012,** *12* (3), 1690-1696.

288. Wu, H.; Li, D. D.; Zhu, X. F.; Yang, C. Y.; Liu, D. F.; Chen, X. Y.; Song, Y.; Lu, L. F., High-performance and renewable supercapacitors based on TiO2 nanotube array electrodes treated by an electrochemical doping approach. *Electrochim. Acta* **2014,** *116*, 129-136.

289. Zhou, H.; Zhang, Y. R., Electrochemically Self-Doped TiO2 Nanotube Arrays for Supercapacitors. *J. Phys. Chem. C* **2014,** *118* (11), 5626-5636.

290. Rao, B. M.; Roy, S. C., Solvothermal Processing of Amorphous TiO2 Nanotube Arrays: Achieving Crystallinity at a Lower Thermal Budget. *The Journal of Physical Chemistry C* **2013,** *118* (2), 1198-1205.

291. Oh, S.; Brammer, K. S.; Li, Y. S. J.; Teng, D.; Engler, A. J.; Chien, S.; Jin, S., Stem cell fate dictated solely by altered nanotube dimension. *Proceedings of the National Academy of Sciences* **2009,** *106* (7), 2130-2135.

292. Mun, K.-S.; Alvarez, S. D.; Choi, W.-Y.; Sailor, M. J., A Stable, Label-free Optical Interferometric Biosensor Based on TiO2 Nanotube Arrays. *ACS Nano* **2010,** *4* (4), 2070-2076.

293. Popat, K. C.; Eltgroth, M.; LaTempa, T. J.; Grimes, C. A.; Desai, T. A., Titania Nanotubes: A Novel Platform for Drug-Eluting Coatings for Medical Implants? *Small* **2007,** *3* (11), 1878-1881.

294. Granitzer, P.; Rumpf, K.; Ohta, T.; Koshida, N.; Poelt, P.; Reissner, M., Porous silicon/Ni composites of high coercivity due to magnetic field-assisted etching. *Nanoscale Research Letters* **2012,** *7*, 4.

295. Nakagawa, T.; Koyama, H.; Koshida, N., Control of structure and optical anisotropy in porous Si by magnetic-field assisted anodization. *Applied Physics Letters* **1996,** *69* (21), 3206-3208.

296. Gelloz, B.; Masunaga, M.; Shirasawa, T.; Mentek, R.; Ohta, T.; Koshida, N., Enhanced Controllability of Periodic Silicon Nanostructures by Magnetic Field Anodization. *ECS Transactions* **2008,** *16* (3), 195-200.

297. Morishita, Y.; Kawai, S.; Sunagawa, J.; Suzuki, T., Magnetic-field-assisted anodization of GaAs substrates. *Electrochemical and Solid State Letters* **2001,** *4* (1), G4-G6.

298. Mark, P.; Helfrich, W., Space-Charge-Limited Currents in Organic Crystals. *Journal of Applied Physics* **1962,** *33* (1), 205-215.

299. Chu, T.-Y.; Song, O.-K., Hole mobility of N,N'-bis(naphthalen-1-yl)-N,N'-bis(phenyl) benzidine investigated by using space-charge-limited currents. *Applied Physics Letters* **2007,** *90* (20), -.

300. Takeshi, Y.; Yoshihisa, Y.; De-Chun, Z.; Tetsuo, T., Carrier Mobilities in Organic Electron Transport Materials Determined from Space Charge Limited Current. *Japanese Journal of Applied Physics* **2002,** *41* (9R), 5626.

301. Murgatroyd, P. N., Theory of space-charge-limited current enhanced by Frenkel effect. *Journal of Physics D: Applied Physics* **1970,** *3* (2), 151.

302. Rose, A., Space-Charge-Limited Currents in Solids. *Physical Review* **1955,** *97* (6), 1538-1544.

303. Nespurek, S.; Sworakowski, J., Use of spaceâ€chargeâ€limited current measurements to determine the properties of energetic distributions of bulk traps. *Journal of Applied Physics* **1980,** *51* (4), 2098-2102.

304. Lampert, M. A., Simplified Theory of Space-Charge-Limited Currents in an Insulator with Traps. *Physical Review* **1956,** *103* (6), 1648-1656.

305. Simmons, J. G., Poole-Frenkel Effect and Schottky Effect in Metal-Insulator-Metal Systems. *Physical Review* **1967,** *155* (3), 657-660.

306. Koszewski, A.; Souchon, F.; Ch, D.; Bloch, D.; Ouisse, T., Physical model of dielectric charging in MEMS. *Journal of Micromechanics and Microengineering* **2013,** *23* (4), 045019.

307. Aleskandrova, P. V.; Gueorguiev, V. K.; Ivanov, T. E.; Koprinarova, J. B., Poole-Frenkel conduction in Al/ZrO2 /SiO 2 /Si structures. *European Physical Journal B* **2006,** *52* (4), 453-457.

308. Hill, R. M., Poole-Frenkel conduction in amorphous solids. *Philosophical Magazine* **1971,** *23* (181), 59-86.

309. Victor, P.; Nagaraju, J.; Krupanidhi, S. B., Growth and electrical characterization of laser ablated highly oriented zirconium titanate thin films in a metalâ€“oxide semiconductor configuration. *Semiconductor Science and Technology* **2003,** *18* (2), 183.

310. Trippe, S. C.; Madaleno, J. C.; Pereira, L., Electrical Properties of Fluorine Doped Diamond Like Carbon. *Materials Science Forum* **2006,** *514-516*, 53-57.

311. Arghya Narayan, B.; Sang Woo, J., Poole-Frenkel effect in sputter-deposited CuAlO2+ x nanocrystals. *Nanotechnology* **2013,** *24* (16), 165705.

312. Takeshita, S. Modeling of Space-Charge-Limited Current Injection Incorporating and Advanced Model of the Poole-Frenkel Effect. All Thesis, Paper 473, Clemson, 2008.

313. Jonscher, A. K., Free-carrier Poole-Frenkel effect in crystalline solids. *Journal of Physics C: Solid State Physics* **1970,** *3* (8), L159.

314. Jonscher, A. K., Electronic properties of amorphous dielectric films. *Thin Solid Films* **1967,** *1* (3), 213-234.

315. Antony, R. P.; Mathews, T.; Panda, K.; Sundaravel, B.; Dash, S.; Tyagi, A. K., Enhanced Field Emission Properties of Electrochemically Synthesized Self-Aligned Nitrogen-Doped TiO2 Nanotube Array Thin Films. *The Journal of Physical Chemistry C* **2012,** *116* (31), 16740-16746.

316. Miyauchi, M.; Tokudome, H.; Toda, Y.; Kamiya, T.; Hosono, H., Electron field emission from <equation>TiO₂</equation> nanotube arrays synthesized by hydrothermal reaction. *Applied Physics Letters* **2006,** *89* (4), 043114-043114-3.

317. Alivov, Y.; Molloi, S., Calculation of field emission enhancement for TiO2 nanotube arrays. *Journal of Applied Physics* **2010,** *108* (2), -.

318. Alivov, Y.; Klopfer, M.; Molloi, S., Enhanced field emission from clustered TiO<inf>2</inf> nanotube arrays. *Applied Physics Letters* **2011,** *99* (6), 063104-063104-3.

319. Chen, J.-B.; Wang, C.-W.; Ma, B.-H.; Li, Y.; Wang, J.; Guo, R.-S.; Liu, W.-M., Field emission from the structure of well-aligned TiO2/Ti nanotube arrays. *Thin Solid Films* **2009,** *517* (15), 4390-4393.

320. Xiang, B.; Zhang, Y.; Wang, Z.; Luo, X. H.; Zhu, Y. W.; Zhang, H. Z.; Yu, D. P., Field-emission properties of TiO 2 nanowire arrays. *Journal of Physics D: Applied Physics* **2005,** *38* (8), 1152.

321. Forbes, R. G., Refining the application of Fowlerâ€“Nordheim theory. *Ultramicroscopy* **1999,** *79* (1â€“4), 11-23.

322. Wenli, Y.; Joseph, M.; Alexander, M.; Colin, A. W., An investigation of annealing on the dielectric performance of TiO 2 thin films. *Semiconductor Science and Technology* **2006,** *21* (12), 1573.

323. Xu, X.; Tang, C.; Zeng, H.; Zhai, T.; Zhang, S.; Zhao, H.; Bando, Y.; Golberg, D., Structural Transformation, Photocatalytic, and Field-Emission Properties of Ridged TiO2 Nanotubes. *ACS Applied Materials & Interfaces* **2011,** *3* (4), 1352-1358.

324. Li, Y.; Fang, X.; Koshizaki, N.; Sasaki, T.; Li, L.; Gao, S.; Shimizu, Y.; Bando, Y.; Golberg, D., Periodic TiO2 Nanorod Arrays with Hexagonal Nonclose-Packed Arrangements: Excellent Field Emitters by Parameter Optimization. *Advanced Functional Materials* **2009,** *19* (15), 2467-2473.

325. Yahya, A.; Michael, K.; Sabee, M., Effect of TiO 2 nanotube parameters on field emission properties. *Nanotechnology* **2010,** *21* (50), 505706.

326. Lengyel, G., Schottky Emission and Conduction in Some Organic Insulating Materials. *Journal of Applied Physics* **1966,** *37* (2), 807-810.

Appendix

In this section a brief description of different current mechanisms is presented followed by preliminary temperature dependent I-V measurements. The obtained current-voltage data fitted to different transport models are performed as an initial study on the contribution of different mechanisms accompanying the dominant SCLC in our single crystal rutile TiO_2 nanowire samples.

When applying an electric field, charge carriers may get injected through an ohmic contact into a material. If the density of injected charge carriers exceeds that of charge carriers present in the material at thermal equilibrium, current flow gets limited by the space charge[298]. SCLC occurs under conditions of high level injection of charge carriers. The unipolar space charge limited current can be expressed as

$$J = \frac{9}{8}\varepsilon\varepsilon_0\mu\frac{E^2}{L} \qquad \text{(A.1)}$$

where J is the current density, ε and ε_0 are the relative dielectric constant and the permittivity of the free space respectively, L is the film thickness, E is the field and μ is the mobility[299, 300]. In the equation above it is assumed that the current consists of the drift of only one type of charge carriers and mobility is considered to be field independent[301]. In order to measure a significant SCLC signal, at least one of the electrodes needs to make an ohmic contact to the material. Equation (A.1) shows that current density in SCLC is proportional to the square of the applied voltage whereas there is a linear relation when the current is ohmic. The critical voltage at which transition from ohmic to SCLC occurs is related to the density of free charge carriers in the material. As soon as the density of injected carriers exceeds the density of free carriers (already

present in the material), SCLC becomes dominant. The excess carriers initially fill traps in materials with a large defect density, and theretfore the critical voltage at which the density of the excess free carriers exceeds that the equilibrium free carriers concnetration is higher than in a defect-free form of the same material [302]. Since SCLC is affected by traps, it has been extensively used for studying the energetic and spatial profiles of the traps in insulators and semiconductors[303]. The SCLC contribution in insulators is stronger than that in semiconductors because the density of free carriers is relatively lower in insulators and the injection of charge carriers from the contact(s) by the application of electrical fields more easily bring about the space charge limited current regime[304]. SCLC was clearly shown for our single crystal TiO_2 nanowire samples in chapter 6 (Figure 6.4). As discussed, in a log-log I-V plot, region with slope 2 represents the SCLC. As discussed in chapter 6, the sudden rise in the current is due to the fact that quasi-fermi level passes the trap level at higher than a certain voltage, all traps get filled and current shoots up because of the trap-free condition governing the material, resulting in a near-vertical rise in the I-V characteristic in the neighbourhood of the trap-free limit. Such a sudden rise in the current at higher voltages is seen in the same plot (Figure 6.4) is a signature of the SCLC. We replaced the Al top contact with 250 nm of Ti metal and performed the same TOF measurements. As can be seen in Figure A.1a, SCLC was again present since in the log-log I-V plot there is a region with the slope of 2 followed by a sudden increase in the current at slightly higher voltages, which is also characteristic of the presence of deep trapping states.

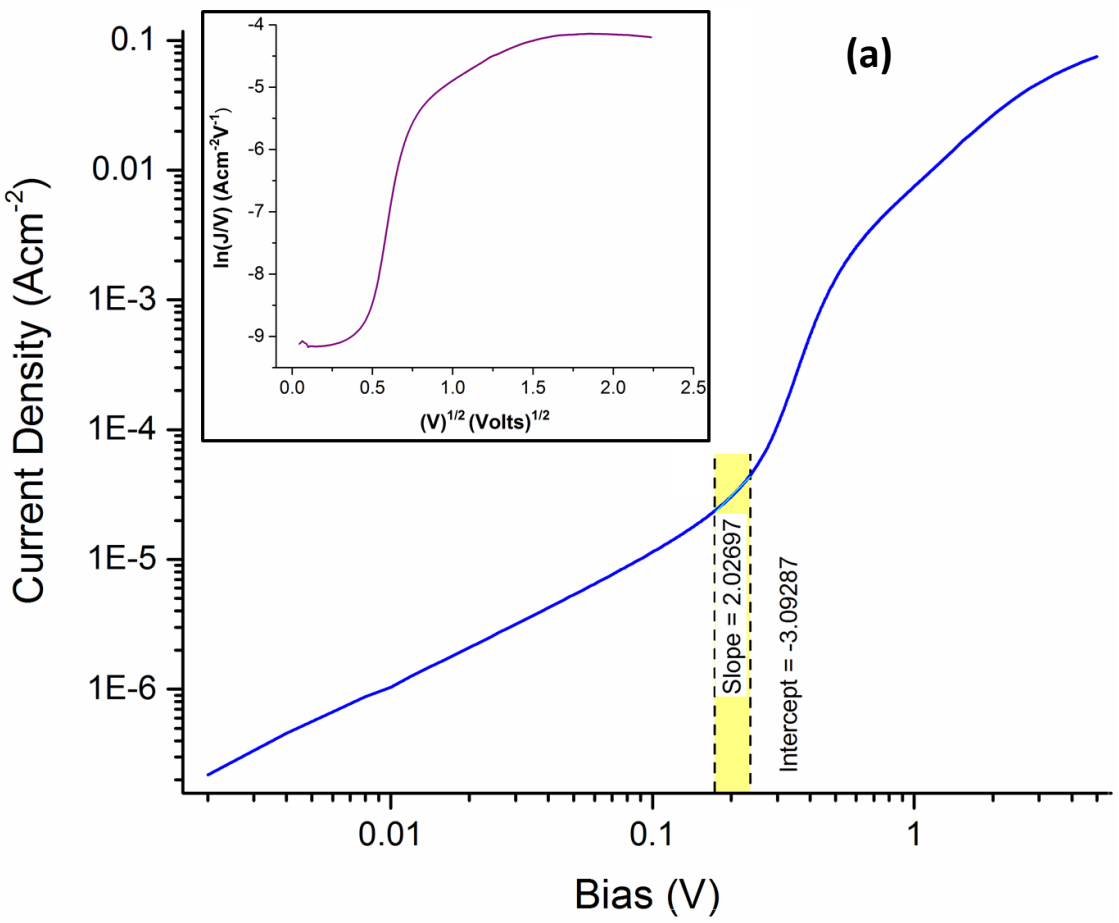

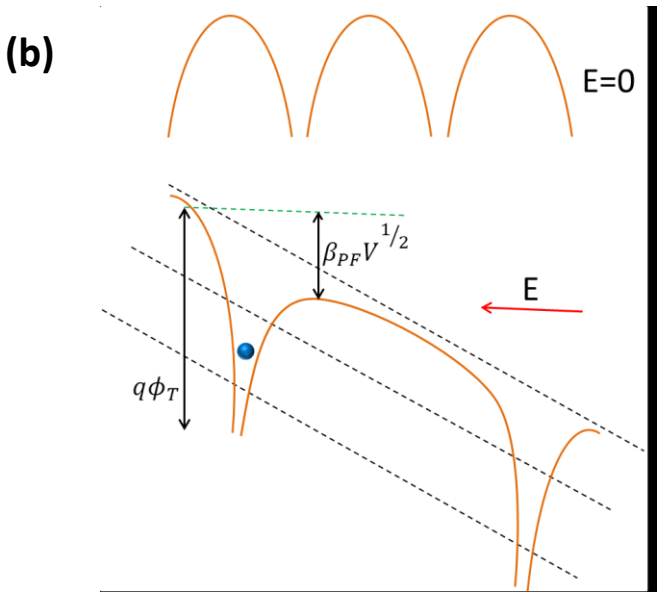

Figure A.1 (a) log-log plot of the steady state current–voltage characteristics and (b) Schematic image showing the Poole-Frenkel conduction mechanism of the rutile nanowire array sample with 250 nm thick Ti top contact. Inset of the (a) shows PF plot of the same sample.

Poole-Frenkel (also known as field-assisted thermal ionization and abbreviated here as PF) is another current mechanism whose presence needed to be investigated in the TiO_2 nanowire samples. As can be seen schematically in Figure A.1b, PF is in fact the reduction in the Coulombic potential barrier of trapping states through interaction with an electric field. At the presence of a strong electric field, the effective depth of a trap is decreased and the proportion of the free charge carriers increases[301, 305]. It can be seen that the PF mechanism involves electron emission from trapping centers into the conduction band of the semiconductor[306]. Because PF-type transport involves both thermal and electric field-activated transport, it sometimes referred to as internal Schottky emission. The PF requirement is that the trap needs to be positively charged when empty and be neutral when filled. A Coulombic barrier is generated when electron interacts with the positively charged trap. The trap which is uncharged when empty, does not contribute in PF emission[305].

The PF equation for charge transport can be written as

$$J = \left(\frac{CV}{L}\right) exp\left(\beta_{PF} V^{1/2}\right) exp\left(-\frac{q\phi_T}{k_B T}\right) \qquad (A.2)$$

where J is the current density, V is the applied voltage, ϕ_T is the ionization energy of the trap levels, k_B is the Boltzman constant, T is the temperature, C is a constant related to the density of ionized traps and carrier mobility and β_{PF} is the barrier lowering coefficient for the PF emission[307]. It has been schematically shown in Figure A.1b that under the applied field, barrier height decreases by $\beta_{PF} V^{1/2}$ denoted in equation (A.2). To be able to get characteristic $\beta_{PF} V^{1/2}$, it is required that the density of the ionizable sites to be in a range that the Coulombic fields of the two adjacent sites do not overlap[308]. According to equation (A.2) one may plot $\ln(J/V)$ vs

$V^{1/2}$ and find the linear regions in order to explore the PF model. In another way one may investigate proportionality of the both ln(J) and ln(J/V) with $1/k_BT$. The latter one requires temperature dependent current-voltage measurements. Inset of the Figure A.1a depicts $\ln(J/V)$ vs $V^{1/2}$ plot known as the PF plot which is however not at all linear at higher voltages (when PF conduction overwhelms ohmic conduction). Unlike SCLC which has been shown to have a decisive role in charge carrier conduction of our sample, the presented PF plot does not seem to provide sufficient basis to consider a PF mechanism contribution. Obtaining a proof for presence of PF requires more systematic temperature-dependent measurements[309-311] which might be the subject of the further study in the future. PF is particularly significant for disordered, amorphous materials. We expect that even if PF has a contribution, it would co-exist along with SCLC and the latter one still would be the dominant mechanism[312]. We think such a space charge limited current regime incorporating Poole-Frenkel emission is more likely than PF alone when dealing with monocrystalline TiO_2 nanowire arrays since it is well known that charge transport purely due to Poole-Frenkel mechanism is rare in highly crystalline materials[313, 314].

Fowler–Nordheim (FN) model as one of the current mechanisms has been investigated for TiO_2 nanostructure-based field-emitters[315-320]. But it is to be noted that FN conduction in TiO_2 nanostructures occurs outside the body of the nanostructure between the tip and the counter-electrode. FN describes tunneling through a triangular potential barrier and is known to take place at high fields. One characteristic fact that makes FN distinguishable from other mechanisms such as PF and Schottky emission (will be discussed later) is that it is not a function of dielectric constant and a relatively extremely weak function of temperature[321, 322]. Our examination of FN emission in TiO_2 nanowire arrays is motivated by the fact that in a material such as TiO_2 nanowire arrays that is expected to contain a high density of deep traps (due to the

large number of surface states), FN conduction can be significant at high electric fields when trapped electrons tunnel through a triangular barrier to either adjacent empty trapping sites or to the conduction band.

The general FN equation can be written as

$$J = \left(\frac{A\beta^2 E^2}{\phi}\right) exp\left(-\frac{B\phi^{3/2}}{\beta E}\right) \quad (A.3)$$

or

$$ln\left(\frac{J}{E^2}\right) = ln\left(\frac{A\beta^2}{\phi}\right) - \frac{B\phi^{3/2}}{\beta E} \quad (A.4)$$

where two constants A and B have the values of $1.54 \times 10^{-6}\ AeVV^{-2}$ and $6.83 \times 10^{3}\ V\mu m^{-1}eV^{-3/2}$ respectively, J is the current density, β is so called the field enhancement factor, E is the applied field and Φ is the work function[323]. The presence of linearity in the so-called Fowler-Nordheim plot ($ln(J/E^2)$ vs 1/E) is an indication of field emission[323]. FN theory in the forms presented in equations (A.3) and (A.4) is always valid for metals however, for wide band gap n-type semiconductors such as TiO_2 it has been suggested to be presented as

$$J = \left(\frac{A\beta^2 E^2}{\phi}\right) exp\left(-\frac{B\phi^{3/2}}{\beta E}\right) exp\left(\frac{-\Delta W^S - \Delta W^p}{2kT}\right) \quad (A.5)$$

In which ΔW^s is the increase of surface barrier potential of nanostructured semiconductor because of the surface states and ΔW^p is the surface barrier layer decrement due to field penetration[315]. Figure A.2 shows the FN plot of the TiO_2 nanowire arrays which shows non-

linearity at small values of 1/V (high voltages) and linearity at higher values of 1/V (low voltages). This behavior is opposite to that of a typical FN plot which exhibits linearity with steep downslope at small reciprocal voltages, followed by a minimum and then gently upsloping non-linear behavior at higher values of 1/V. Therefore, our results indicate that field emission does not exist in the rutile nanowire arrays in the range of applied voltages. To the best of our knowledge, field emission of TiO_2 nanostructures has been demonstrated typically at electric fields higher than about $5\ V/\mu m$ [315, 316, 318-320, 323]. Our SCLC study has been limited to the electric field range of about 0 to 4.5 $V/\mu m$ (Figure 6.4) and the FN plot (Figure A.2) does not show field emission. It has been also reported that field enhancement factor (β) is proportional to the spacing between the 1-D TiO_2 nanostructures[317-319, 323, 324] and spacing between anode and cathode[323, 325]. FN mechanism did not show noticeable contribution at present work since utilized TiO_2 nanowire arrays were highly close-packed and had the effective charge transport length of about 1.2 μm. Also at high dopant densities (> 10^{19} cm^{-3}), it might be possible that the barrier (with for instance a contact electrode) becomes narrow enough to allow the charge carriers to tunnel through it. But neither the ohmic nor the space-charge limited transport regimes in Figure 6.4 in Chapter 6 show any indication of a high carrier density. A high carrier density would render a low dielectric relaxation time and would also preclude the observation of a clear maximum in the photoconductivity transient (Figure 6.3) in the time scale indicated.

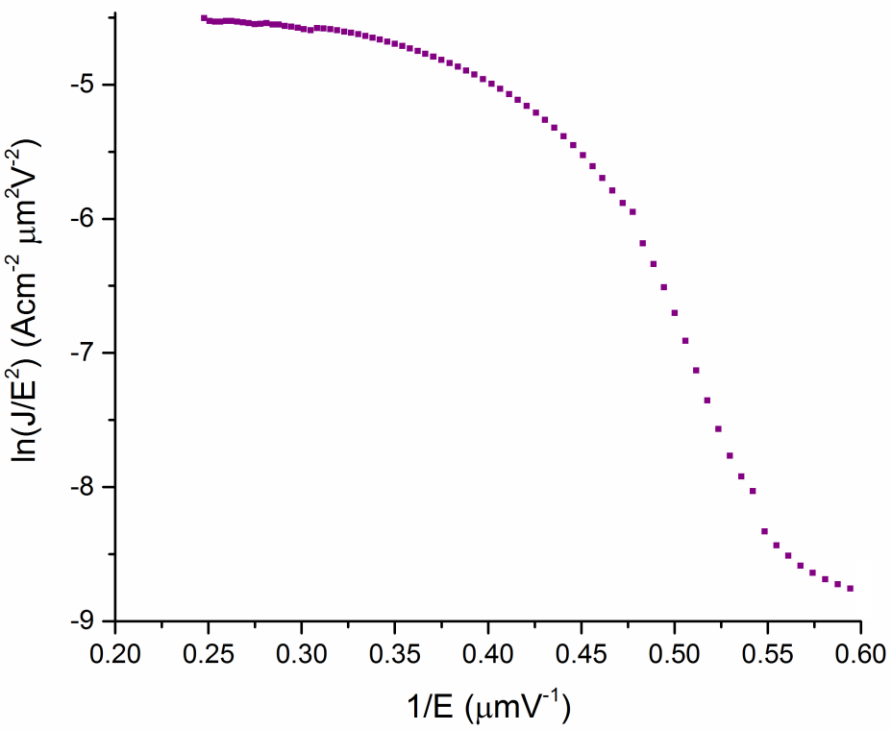

Figure A.2 Fowler-Nordheim plot of the monocrystalline rutile TiO_2 nanowire arrays.

Schottky emission is the last mechanism whose contribution in the conductivity of the TiO_2 nanowire samples with Ti top contact needs to be investigated. It is referred to as thermionic emission and considers the influence of heat and electric field in enabling charge carriers to surmount a potential barrier, typically with a metallic contact electrode. The difference in the work functions of the charge transport material and the metal contact controls the emission current[326]. It looks like the previously explained PF mechanism but with the difference that PF conductivity is observed only in bulk-limited conduction processes whereas Schottky emission is basically an electrode-limited process[305].

The Schottky equation can be written as

$$J = A^{*}T^{2} exp\left(\beta_{Sc} V^{1/2}\right) exp\left(-\frac{q\phi_B}{k_B T}\right) \quad \text{(A.6)}$$

where J is the current density, V is the applied voltage, A^* is the effective Richardson constant, ϕ_B is the Schottky barrier height, β_{Sc} is the barrier lowering coefficients for the Schottky emission, k_B is the Boltzman constant and T is the temperature[307]. Figure A.3a shows current density versus voltage plot of the same TiO_2 nanowire array sample with Ti top contact. The current density has been plotted in log scale in order to make a clearer comparison between the current density values at positive and negative applied voltages. It shows that for voltage between 0.5 V to 2 V and -2 V to -0.5 V there is more than 10 times difference between the current density values at the symmetric positive and negative voltages. In other plot regions, ohmic behavior is seen.

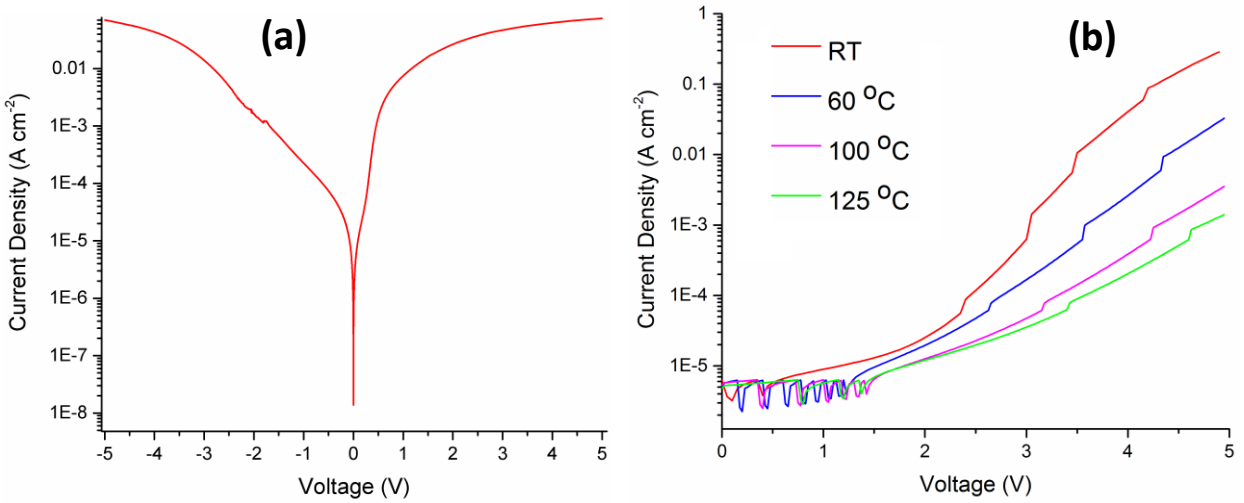

Figure A.3 Current density (log scale) versus voltage plot of the TiO_2 nanowire array sample (a) with Ti top contact and (b) at different temperatures with Al top contact.

In order to shed further light on the transport mechanisms, preliminary temperature dependent-studies were initiated. For the TiO_2 nanowire samples with Al top contact, current

density versus voltage measurements were performed at 125 ^{o}C, 100 ^{o}C, 60 ^{o}C and room temperature. In this sample 300 nm Al was deposited onto the photolithografically created features in HPR 504 photoresist by electron beam evaporation followed by removing the unwanted Al by lift-off. As can be seen in Figure A.3b, current density decreases by increasing the temperature. It may indicate that thermally activated charge transport processes such as thermionic emission and Poole-Frenkel emission do not contribute to current conduction in our samples. FN is a very weakly temperature-dependent mechanism and the observed temperature dependency shown above may eliminate its presence as well. However, to constitute a more thorough study, further temperature-dependent studies using different contact electrodes and nanowire lengths and particularly using cryogenic temperatures are necessary.